CHARLES UNIVERSITY
Faculty of Science

Study programme: Physical chemistry
Branch of study: Physical chemistry

Bc. Klára Veselá

Zeolite-amine complex catalysis of Meerwein-Ponndorf-Verley type hydrogen transfer reactions

Master thesis

Supervisor: Ing. Jan Přech, Ph.D.

Consultant: doc. Mariya Shamzhy, Ph.D.

Prague, 2025

UNIVERZITA KARLOVA
Přírodovědecká fakulta

Studijní program: Fyzikální chemie
Studijní obor: Fyzikální chemie

Bc. Klára Veselá

Katalýza reakcí přenosu vodíku typu Meerwein-Ponndorf-Verley pomocí zeolit-aminových komplexů

Diplomová práce

Školitel: Ing. Jan Přech, Ph.D.

Konzultant: doc. Mariya Shamzhy, Ph.D.

Praha, 2025

Prohlášení

Prohlašuji, že jsem tuto závěrečnou práci zpracovala samostatně a že jsem uvedla všechny použité informační zdroje a literaturu. Tato práce ani její podstatná část nebyla předložena k získání jiného nebo stejného akademického titulu.

Jsem si vědoma toho, že případné využití výsledků, získaných v této práci, mimo Univerzitu Karlovu je možné pouze po písemném souhlasu této univerzity.

V Praze dne, 16.5.2025 Klára Veselá

Acknowledgement

I would like to sincerely thank my supervisor, Ing. Jan Přech, Ph.D., for his help, patience, and continuous support throughout both my bachelor's and master's studies. I am also grateful to my consultant, doc. Mariya Shamzhy, Ph.D., for her valuable advice and insightful guidance. My sincere thanks extend to Prof. Jiří Čejka and his research group (Heterogeneous Catalysis and Advanced Materials) for their support and for creating such an inspiring research environment. I am also thankful to MSc. Yuqi Zhang for her kind help with the FTIR measurements, and MSc. Jun Xie for her assistance with the catalytic experiments carried out without the addition of base. I would also like to acknowledge Mgr. Jiří Dědeček, CSc., DSc., and Ing. Galina Sádovská, Ph.D., for their assistance with the interpretation of UV-Vis spectra. Finally, I am immensely thankful to my family, my partner, and my friends for their unwavering support and understanding throughout my studies.

Abstract

Meerwein-Ponndorf-Verley (MPV) reduction is a selective hydrogen transfer reaction that converts carbonyl compounds to the corresponding alcohols under mild conditions, offering a safer alternative to conventional hydrogenation by avoiding the use of molecular hydrogen. Recently, Lewis acid zeolites, particularly Zr- and Sn-substituted beta zeolites, have been identified as effective catalysts. Although MPV reduction is typically highly selective, its selectivity can decrease when the substrate structure allows competing Lewis catalysed reactions. In such cases, the addition of organic bases can increase selectivity by forming zeolite-amine complexes, although the mechanism as well as the base structure-activity correlations are unknown.

This study focuses on the MPV reduction of citronellal, a bio-derived aldehyde, in the presence of Zr- and Sn-beta catalysts, which suffers from side reactions like carbonyl-ene cyclization and acetalization. Small nitrogen-containing organic bases such as pyridine and N-methylpiperidine were used to increase the citronellol selectivity and to disclose the structure-activity correlations between the base and the selectivity improvement. A series of pyridine-derived bases shifted selectivity in favour of citronellol except 2,6-ditert-butylpyridine, which is unable to coordinate. Regarding overall conversion, pyridine and 2,5-lutidine caused only a slight decrease (83% conversion after 6 hours) compared to the base-free system (97 %). In contrast, bulkier 2,4,6-collidine resulted in significantly lower conversion (48 %), likely due to restricting diffusion and limiting access to the active sites. This highlights that coordination to the Lewis sites is essential, as only bases that can coordinate, form the zeolite-amine complexes and modulate the reaction selectivity. Notably, the presence of the base accelerated citronellol formation, suggesting that the zeolite-amine complex modifies the active sites rather than poisons them, as is often observed with aluminosilicate zeolites.

Building on these observations, apparent activation energies of individual reaction pathways were determined with added bases. Kinetic studies, performed between 40 and 80 °C using N-methylpiperidine and pyridine over Zr- and Sn-beta zeolites, showed that the pyridine addition decreased the apparent activation energy for citronellol formation from 56 $kJ \cdot mol^{-1}$ (base-free system) to 44 $kJ \cdot mol^{-1}$, while that for isopulegol remained unchanged (26 $kJ \cdot mol^{-1}$). The reaction with N-methylpiperidine was diffusion-limited, as formation of both products exhibited values below 30 $kJ \cdot mol^{-1}$. These findings highlight that the zeolite-amine complex influences intrinsic reaction mechanism, likely through active site modification and change in internal diffusion.

Key words: catalysis, Lewis acid, zeolite, amine, Meerwein-Ponndorf-Verley reduction, hydrogen transfer, stereoselectivity

Abstrakt

Meerwein-Ponndorf-Verleyho (MPV) redukce je selektivní reakce přenosu vodíku, která transformuje za mírných podmínek karbonylové sloučeniny na odpovídající alkoholy a nabízí tak bezpečnější alternativu ke klasické hydrogenaci, neboť se vyhýbá použití molekulárního vodíku. Účinnými katalyzátory této reakce jsou zeolity s Lewisovými kyselými centry, zejména Zr- a Sn-silikátové beta zeolity. Ačkoliv je MPV redukce obecně vysoce selektivní, její selektivita může poklesnout, pokud struktura substrátu umožňuje konkurenční Lewisovsky katalyzované reakční cesty. V takových případech lze zvýšit selektivitu přídavkem organických bází - aminů, které vytvářejí zeolit-aminové komplexy, nicméně, mechanismus tohoto jevu ani korelace mezi strukturou báze a její aktivitou při zvýšení selektivity nejsou známy.

Tato práce se zaměřuje na MPV redukci citronellalu, aldehydu přírodního původu, v přítomnosti Zr- a Sn-beta katalyzátorů. Této reakci konkurují karbonyl-en cyklizace a acetalizace. Malé dusíkaté organické báze (pyridin a N-methylpiperidin) byly použity ke zvýšení selektivity tvorby citronellolu a ke zkoumání korelace mezi jejich strukturou a aktivitou. Řada bází odvozených od pyridinu posunula selektivitu ve prospěch citronellolu s výjimkou 2,6-ditert-butylpyridinu, který není schopen koordinace na Lewisovská centra. Z hlediska konverze citronellalu, pyridin a 2,5-lutidin způsobily pouze mírný pokles (83% konverze po 6 hodinách) ve srovnání se systémem bez báze (97 %). Naopak objemnější 2,4,6-kolidin vedl k výrazně nižší konverzi (48 %), pravděpodobně v důsledku zpomalování difúze a přístupu k aktivním centrům. Tyto výsledky ukazují, že schopnost báze koordinovat se na Lewisovská centra je klíčová. Pouze báze, které se mohou koordinovat, vytvářejí zeolit-aminové komplexy a modulují selektivitu reakce. Pozoruhodné je, že přítomnost báze zároveň urychlila tvorbu citronellolu, což naznačuje, že zeolit-aminový komplex je vlastně modifikace aktivního centra, přičemž nedochází k prosté deaktivaci katalyzátoru (běžné u aluminosilikátových zeolitů).

Na základě těchto pozorování byly stanoveny zdánlivé aktivační energie jednotlivých reakčních cest za přítomnosti bází a bez nich. Kinetická studie provedená při 40-80 °C s použitím N-methylpiperidinu a pyridinu na Zr- a Sn-beta zeolitech ukázala, že přídavek pyridinu snížil zdánlivou aktivační energie tvorby citronellolu z 56 (reakce bez báze) na 44 $\mathrm{kJ \cdot mol^{-1}}$, zatímco hodnota pro tvorbu isopulegolu zůstala nezměněna (26 $\mathrm{kJ \cdot mol^{-1}}$). Reakce s N-methylpiperidinem byla difúzně řízená, neboť tvorba obou produktů vykazovala hodnoty pod 30 $\mathrm{kJ \cdot mol^{-1}}$. Tato zjištění naznačují, že zeolit-aminové komplexy ovlivňují vlastní reakční mechanismus, pravděpodobně prostřednictvím modifikace aktivních center a zpomalení vnitřní difúze.

Klíčová slova: katalýza, Lewisova kyselina, zeolit, amin, Meerwein-Ponndorf-Verleyho redukce, přenos vodíku, stereoselektivita

Table of contents

List of abbreviations

2,6-DTBP	2,6-ditert-butylpyridine
BAS	Brønsted Acid Site
BET	Brunauer-Emmett-Teller
EDX	Energy-Dispersive X-ray Spectrscopy
FID	Flame Ionization Detector
FTIR	Fourier-Transform Infrared Spectroscopy
GC	Gas Chromatography
ICP-MS	Inductively Coupled Plasma – Mass Spectrometry
IUPAC	International Union of Pure and Applied Chemistry
IZA	International Zeolite Association
LAS	Lewis Acid Sites
MPV	Meerwein-Ponndorf-Verley
NMR	Nuclear Magnetic Resonance Spectroscopy
ppm	Parts per million
PXRD	Powder X-ray Diffraction
rpm	Rotations per minute
SEM	Scanning Electron Microscopy
TEAOH	Tetraethylammonium hydroxide
TEM	Transmission Electron Microscopy
TEOS	Tetraethyl orthosilicate
UV-Vis	Ultraviolet-Visible
XRD	X-ray Diffraction

1 Introduction

Zeolites are crystalline microporous metallosilicate materials with frameworks composed of tetrahedrally coordinated silicon or metal atoms connected by oxygen bridges. This unique structure provides high thermal stability, a large surface area, molecular sieving properties, and the presence of acid sites, making zeolites highly effective as heterogeneous catalysts (besides other applications such as adsorption and ion-exchange). One of the most important features of zeolites is their acidity, which is induced by the incorporation of metal atoms (heteroatoms) in the zeolite framework. The type and concentration of these heteroatoms determine the acidity and thus define catalytic properties. In aluminosilicate zeolites, the trivalent aluminium generates Brønsted acid sites, which are effective for proton-mediated reactions (such as isomerisation of alkenes or cracking)[1]. In contrast, zeolites containing tetravalent heteroatoms, such as zirconosilicates, feature Lewis acid sites, where vacant d-orbitals of zirconium enable electron pair acceptance, contributing to their catalytic activity. These Lewis acid zeolites (e.g., Ti, Sn, Zr silicates) catalyse diverse chemical transformations, including hydrogen transfer reactions, epoxidation, dehydration, and others.[2] The studied Meerwein-Ponndorf-Verley (MPV) reduction converts aldehydes and ketones to their corresponding alcohols using other secondary alcohols as reducing agents under mild conditions.

In my bachelor's thesis[3], I investigated the effect of nitrogen organic bases (e.g., pyridine, N-methylpiperidine) on MPV reduction of prochiral ketones with 2-propanol over Zr-beta and Sn-beta Lewis acid zeolite catalysts. Additionally, I studied how bases influence MPV reduction of citronellal with 2-propanol, where the addition of the base increases the MPV reaction selectivity. In this reaction, isopulegol (product of the competing carbonyl-ene intramolecular reaction) was the main product in the base-free conditions, while citronellol became dominant with the addition of the base. Although bases generally decreased the reaction rate, it still proceeded. Base titration experiments showed that one molar equivalent of base per active site was sufficient to induce this selectivity switch, regardless of the base's pKa, indicating that basicity on its own does not define the extent of the selectivity switch. This means the base somehow directly influences function of the zeolite Lewis sites. Overall, these findings highlight the potential of base-modified Lewis acid zeolites for selective transformations and, possibly, chiral induction in MPV reductions.

Building on these insights, the present thesis delves into the mechanism of the base-mediated MPV reduction, focusing on how the organic bases (pyridine, substituted pyridines and N-methylpiperidine) influence the reaction mechanism of citronellal with 2-propanol over the Lewis acid zeolites model reaction. The primary objectives were to determine whether the base must be directly coordinated to the Lewis acid site to switch the selectivity of the reaction. Additionally, the study aimed to explain how the size and steric hindrance of the nitrogen atom in the base's structure affect the reaction. This was followed by a kinetic study aiming at the determination of the apparent activation energies for pathways leading to individual products to prove if the intrinsic mechanism of the studied reaction is changed upon introduction of the base.

Overall, the goals of my master's thesis are to provide a more detailed understanding of how organic bases influence hydrogen transfer reactions catalysed by Lewis acid zeolites. This involves addressing four key questions:

1) Does the base need to be coordinated to the active sites?
2) How do the size and steric hindrance of the base affect reaction outcomes?
3) Does the introduction of the base change the intrinsic reaction mechanism?
4) Is it possible to induce stereoselective course of the MPV reduction using chiral base-modified Lewis acid zeolites?

2 Theoretical part

Catalysis is an important fundamental phenomenon, playing a role in approximately 90% of chemical processes in modern chemistry. By definition, a catalyst is a substance that increases the rate of a chemical reaction by providing an alternative reaction pathway with lower activation energy of the rate determining step, thus enabling the reaction to proceed more selectively and/or under milder conditions. A catalyst is not consumed in the reaction and can be used repeatedly. However, its activity may decrease after a certain number of reaction turnovers for various reasons (so-called catalyst deactivation).[4,5] Catalysis can be classified into three groups: heterogeneous, homogeneous, and enzymatic catalysis. In heterogeneous catalysis, the catalyst is present in a different phase than the reactants (usually solid) and the reactions occur in the interphase. This provides, i.a., an advantage of easy catalyst separation from the reaction mixture allowing use in continuous flow systems. Zeolites are one of the most important classes of heterogeneous catalysts, finding applications in a variety of reactions, including catalytic cracking[6], isomerisation, alkylation, and other processes.[7] In this work we used zeolites for catalysing studied hydrogen transfer reactions. In contrast, a homogeneous catalyst is present in the same phase as the reactants (typically liquid phase). For example, Diels-Alder reactions, or acid or base catalysed ester hydrolysis/transesterification are homogeneously catalysed.[8] The third group, enzymes, are highly selective biological catalysts (biocatalysts), which catalyse biochemical reactions in cells. They are mostly proteins, work under mild conditions and are known for their specificity for their substrates. Enzymes play a crucial role in metabolic pathways and many industrial applications, such as in biosensors and the food industry (e.g., acid proteases in cheese manufacture or glucose isomerase for sweeteners).[9]

2.1 Zeolites

Zeolites are crystalline microporous[(1)] silicate materials[10], which are primarily found in nature and are of volcanic and hydrothermal origin. The natural zeolites found applications in environmental protection and agriculture (e.g. treatment of soil or ponds); however, their industrial use is limited because the zeolite properties strongly depend, i.a., on their crystal structure (the natural zeolites are mostly small-pore zeolites; see below), crystal size, and particularly their variable chemical composition, consisting of a mixture of

[(1)] pores with diameter smaller than 2 nm according to IUPAC

various elements. The naturally occurring zeolites with practical significance include mordenite or chabazite. For industrial catalytic applications, zeolites are typically synthetic and their synthesis is tuned to achieve specific morphology and tailored chemical composition, enabling, e.g., the adsorption of large molecules (such as branched hydrocarbons or xylene isomers)[11] and providing specific strength of acid sites.[12] The zeolites exhibit unique properties, including a high surface area and adsorption capacity, thermal and chemical stability, strong and tuneable acidity and molecular sieving properties.[13] Additionally, zeolites are also used as ion-exchangers for water purification, adsorbents in separation and purification processes,[14,15] and upgrading or purification of natural gas[16]. Nowadays, there have been synthesised more than 250 zeolite topologies recognised by the International Zeolite Association (IZA)[17], designated by three-letter structure codes (e.g., MFI, FAU, UTL).

The structure of zeolites is highly ordered and well-defined, consisting of a framework built from tetrahedral TO_4 units, where T represents a tetrahedrally coordinated atom (trivalent (+3) or tetravalent (+4) cation), such as Al^{3+}, Si^{4+}, Zr^{4+}, Sn^{4+}, Ti^{4+}, and others. T-atoms are located at the centre of the TO_4 units and are connected through the shared oxygen atoms in their corners forming higher building units such as rings, prisms or small cages. These structural variations forming the framework of zeolites result in diversity in pore sizes, pore connectivity and cavity sizes, each with a unique geometric structure and chemical composition.[18,19]

Zeolites can be classified according to various aspects. One of them is based on the number of tetrahedral atoms (T-atoms) at the pore openings defining the size of molecules that can penetrate. Small-pore zeolites have 8 T-atoms in the channel size defining ring, medium-pore zeolites have 10, and large-pore zeolites contain 12 T-atoms. Extra-large-pore zeolites, with more than 12 T-atoms, are relatively rare, but offer exceptional potential, particularly as catalysts, as they allow even sterically demanding molecules to reach active sites located in their pores.[20–22]

The catalytic properties of zeolites are closely linked to their acid sites, which are formed through the substitution of silicon for aluminium, which is the typical T-atom, but also other trivalent cations such as B^{3+}, Fe^{3+}, or Ga^{3+}, as well as tetravalent cations like Ti^{4+}, Sn^{4+}, Zr^{4+}, Hf^{4+} can be incorporated. Trivalent cations introduce negatively charged sites in the framework, which are compensated by extra-framework cations, such as protons or other

cations.[23] Therefore, incorporation of these trivalent heteroatoms into a zeolite framework generates Brønsted acid sites. On the other hand, tetravalent cations like Sn^{4+} or Zr^{4+} do not disrupt the framework charge but act as Lewis acid sites due to their empty d-orbitals.[18] The strength of the acid sites is defined by the nature of the incorporated heteroatom and the local framework environment, including bond length, angles and framework disruptions.[19] The Si/*M* molar ratio is used to describe the chemical composition of zeolites, indicating the silicon-to-metal ratio within the zeolite structure. This ratio also influences properties like acidity strength, thermal stability, and hydrophobicity, which are important for the selection of zeolites for specific applications.

Last but not least, zeolites are environmentally friendly materials that work as efficient and easily separable heterogeneous catalysts, replacing harmful chemicals in many processes. Thanks to their unique structure, they save energy and make production cleaner and more sustainable. They are also great for protecting the environment by helping clean air, water and soil from pollutants.[24]

2.1.1 Lewis acid zeolites (structure and properties)

Lewis acid zeolites are zeolites containing tetravalent metal atoms (e.g., Sn^{4+}, Zr^{4+} or Ti^{4+}) incorporated into the zeolite framework. These heteroatoms generate Lewis acid sites that act as electron pair acceptors as they have vacant d-orbitals.[19] Such materials catalyse a wide range of reactions, for example, hydrogen transfer reactions (MPV reduction and sugar isomerisation[25]), Baeyer-Villiger oxidation[26], epoxidation with peroxides[27], and various dehydration reactions[28].

Among Lewis acid zeolites, titanium silicate-1 (TS-1, MFI structure), is the only one used in industrial processes. Its catalytic activity stems from titanium active sites within the silicate framework, which are able to form peroxo-species thereby activating peroxides.[19] Thus, it can be used in selective oxidation reactions, including the epoxidation of alkenes, hydroxylation of aromatics, and ammoxidation of cyclohexanone.[29]

Lewis acid zeolites can be prepared through two main strategies: direct synthesis and post-synthesis modification. In the direct synthesis, heteroatoms generating the Lewis acid sites are introduced into the synthesis mixture. This can be achieved through hydrothermal synthesis, where a silicon source (e.g., fumed silica or tetraethyl orthosilicate) is mixed with a corresponding metal source (e.g., tin or zirconium chloride or alkoxide used in our case)

in the presence of mineralizers (hydroxide or fluoride ions), structure directing agents and water.[30] The second approach is based on modification of already existing zeolites to introduce the Lewis acid sites. For instance, an original aluminosilicate zeolite is first dealuminated using acid treatment to remove aluminium atoms from the framework. The resulting defects are then filled by incorporating the tetravalent metal ions, creating the Lewis acid sites.[31]

Zeolite beta, one of the most studied structures in the area of Lewis acid zeolites, has three-dimensional pore system with large pore openings (12-ring channels) and pore diameter of around 6.7 Å. Beta zeolite has complex structure, which includes different polymorphs designated as beta-A, beta-B, beta-CH and polymorph beta-C.[32] These polymorphs differ in the arrangement of beta layers within their crystal lattice, specifically in the connectivity of the beta layer (Figure 1; defined by the IZA[32] as so-called Periodic Building Units).[33,34]

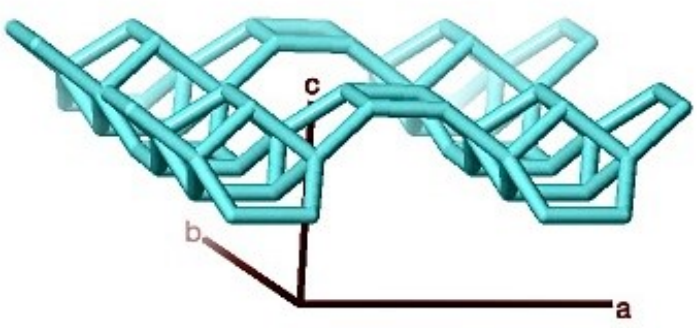

Figure 1: Structure of beta layer[32]

Polymorph beta-A is characterised by tetragonal symmetry, while beta-B and beta-CH exhibit monoclinic symmetry. Pure forms of polymorphs beta-A, -B, and -CH have not yet been prepared; these structures predominantly occur as intergrowths of each other within individual crystals of beta zeolite.[33,34] In this study, hydrothermally prepared Zr-beta and Sn-beta zeolites without aluminium content are used, which are a mixture of polymorphs A and B.

2.1.2 Active sites in Zr- and Sn-zeolites

In the zeolite framework, substituted tetravalent atoms can principally exist in three types of sites: "closed" $M(OSi)_4$, "open" $M(OSi)_3OH$, and "double-defective" $M(OSi)_2(OH)_2$ (see in Figure 2). Additionally, there are "oxidic" species *M*-O-*M*, which are not part of the framework and are considered as extra-framework species. In this context, *M* stands for substituting atoms such as Sn or Zr.[19,35] "Closed" sites are characterised by the metal ion

fully bonded to 4 neighbouring SiO_4, while "open" sites have only 3 oxygen bridges with 1 hydroxyl group completing the coordination. "Double-defective" sites are linked through 2 SiO_4 bridges and 2 hydroxyl groups. "Oxidic" species are structures containing metal-oxygen-metal linkages, at least one per unit, that exist outside the primary zeolite framework.[36] Acid site strength follows a general trend: "open" > "closed" > "double-defective" > silanol. It is also important to mention that the properties of sites may vary depending on the crystallographic position.[36] Initially, it was believed that "closed" and "open" sites transformed into one another upon hydration or dehydration. However, recent studies[37,38] have demonstrated that while such transformations occur, both types of sites coordinate water under hydrated conditions, increasing their coordination number to five or six.[19] The type of acid sites in zeolites can be distinguished by various spectroscopic techniques, such as Fourier-transform infrared spectroscopy (FTIR), solid-state nuclear magnetic resonance spectroscopy (NMR), or UV-Vis spectroscopy, depending on the heteroatom in the zeolite structure. For our synthesised zirconosilicate materials, we primarily used FTIR analysis of adsorbed probe molecules. FTIR spectroscopy identifies vibrational modes of probe molecules, such as C≡N stretching vibration in d_3-acetonitrile. When these molecules interact with synthesised material, shifts in electron density alter bond strengths, leading to characteristic changes in vibrational frequencies.[39] For Sn-zeolites, deuterated acetonitrile (d_3-acetonitrile)[40] is commonly used, while for Zr-zeolites, carbon monoxide[41] is preferred because d_3-acetonitrile does not interact with "closed" Zr sites.

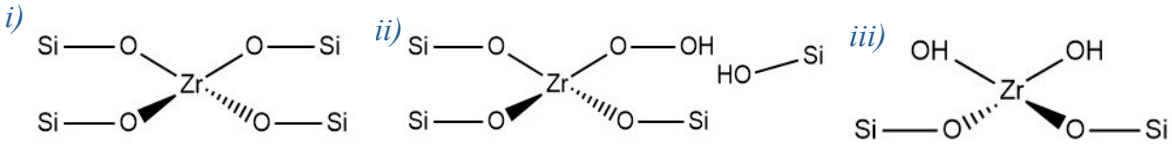

Figure 2: i) "closed", ii) "open", iii) "double-defective" Zr Lewis acid sites

2.1.3 Interaction of amines with Lewis centres

Lewis acids are defined as species capable of accepting an electron pair, while amines act as Lewis bases, due to the presence of nitrogen atoms with a lone pair of electrons. The interaction between Lewis acid and Lewis base leads to the formation of a Lewis adduct. The strength and stability of this interaction depend on multiple factors, including the electronic and structural characteristics of the Lewis acid, the electron-donating ability and the basicity of the amine, and the surrounding medium.[42] Pyridine and alkyl-pyridines are often used as probe molecules among Lewis bases to study the acidity of solid materials like

aluminosilicates using FTIR spectroscopy.[43–45] An example of this technique is a selective poisoning approach using pyridine to determine number and strength of active protonic acid sites on zeolites (e.g., Y and ZSM-5) by blocking stronger acid sites through irreversible sorption at elevated temperatures (e.g., 300 °C). The number of blocked acid sites was quantified via gas chromatography stepwise thermal desorption to determine irreversible sorption of pyridine[46]. Beyond characterization, amines can be used to influence/modify the catalytic behaviour of Lewis acid sites during the reaction. In zeolite-catalysed reactions, amines interact with the acid sites within the zeolite framework, which can alter reaction pathways and affect product selectivity by either promoting or suppressing specific transformations.[47]

2.2 Hydrogen transfer reactions catalysed by zeolites

2.2.1 Meerwein-Ponndorf-Verley reduction

Meerwein-Ponndorf-Verley (MPV) reduction is a hydrogen transfer reaction, which has already been known for one hundred years. In 1925, Meerwein and Schmidt,[48] along with Verley[30] discovered that aluminium ethoxide, the original catalyst for this reaction, reduces aldehydes in the presence of ethanol.[47] A year later, Ponndorf[49] explained the mechanism showing that ketones could also be reduced with aluminium alkoxides.

The reaction has been extensively studied since the mid-90s due to its wide-ranging applications in organic synthesis, pharmaceuticals and fine chemical areas. During this period, the MPV mechanism was well described by H. van Bekkum.[45] The original homogenous catalysis has evolved into nowadays heterogeneous catalysis, with catalysts like Lewis acid zeolites and metal-organic-frameworks now playing a key role.[50] The reaction mechanism (Figure 3) involves formation of a six-membered cyclic transition state, where a hydride transfer occurs from the alcohol to the carbonyl carbon of the substrate. In the case of citronellal MPV reduction, 2-propanol first adsorbs onto the Lewis acid site in the zeolite and undergoes deprotonation (*1*). Then citronellal interacts with the same catalytic centre (*2*), enabling the hydride transfer within the cyclic transition state, converting citronellal to citronellol (*3*). The catalyst plays a crucial role, coordinating through oxygen atoms and stabilizing the intermediate, which is essential for the transfer of hydrogen. Acetone then desorbs from the catalytic site (*4*), followed by the desorption of citronellol (*5*), regenerating the active site and allowing the catalytic cycle to repeat. One of the main

advantages of this reaction is that it does not require the use of molecular hydrogen. In addition, it proceeds under mild conditions, which means temperatures below 100 °C and atmospheric pressure.[51,52]

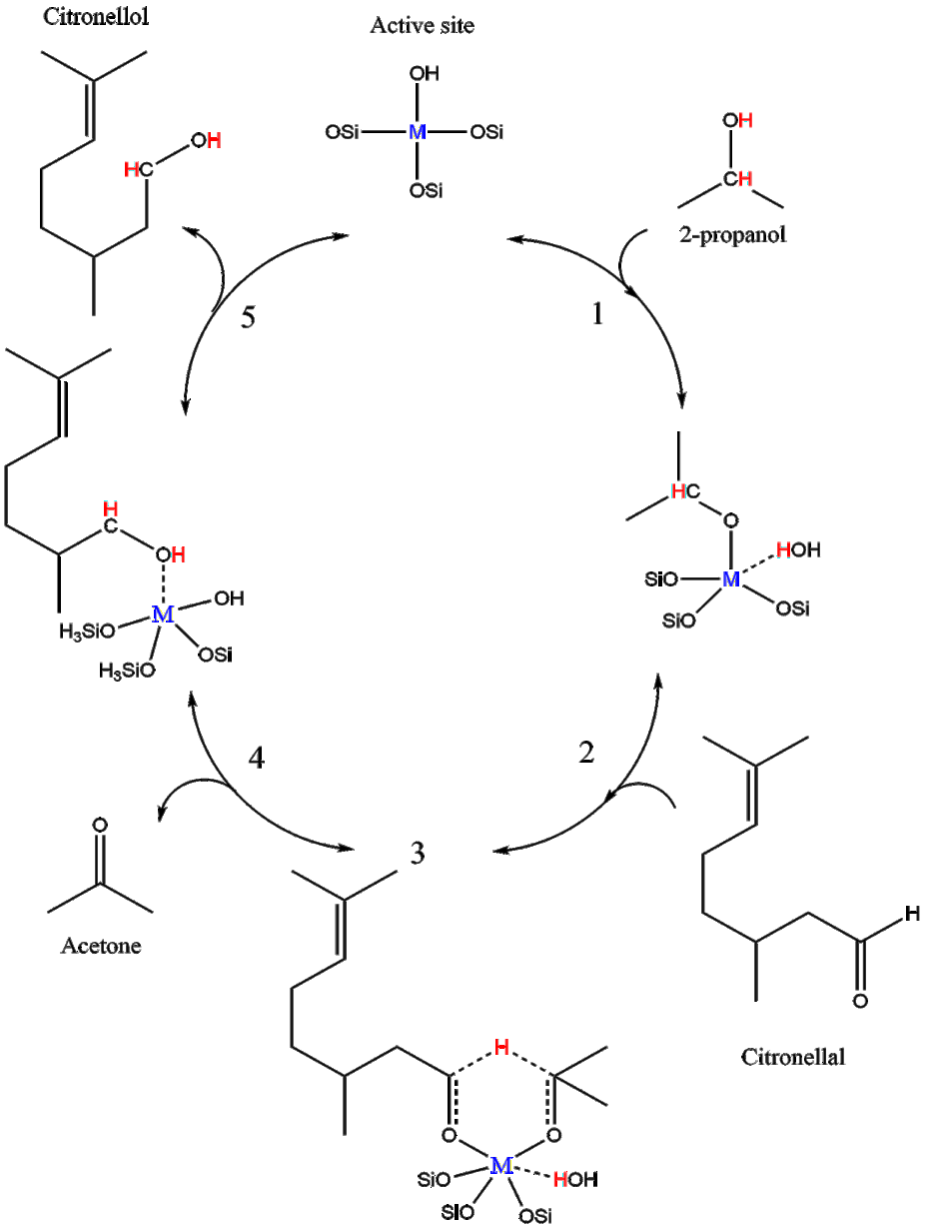

Figure 3: Proposed catalytic cycle for MPV reduction of citronellal to citronellol with 2-propanol over 1 active site in zeolite framework[51]

2.3 Characterization techniques used

Solid materials cannot be fully characterised by a single experimental technique, unlike small organic compounds. To get a full analysis of their structure, a combination of different techniques is necessary. For example, to determine the crystalline structure, X-ray powder diffraction (PXRD), transmission electron microscopy (TEM) and electron

diffraction are used, while textural properties such as surface area, total pore and micropore volume are evaluated using sorption. Additionally, the chemical composition of synthesised material is analysed by ICP-MS, while UV-Vis spectroscopy is employed to identify metal sites and their coordination environment. FTIR spectroscopy provides information on functional groups and bonding environments within the materials.

2.3.1 X-ray powder diffraction

X-ray powder diffraction (PXRD) is used to determine the crystalline structure of materials. It utilizes X-rays, which have a short wavelength and high energy. Originally, X-rays found applications in three areas: radiography for imaging dense materials; crystallography for studying crystalline structures and fluorescence spectrometry for elemental analysis.[53] This non-destructive method operates on the principle of constructive interference of monochromatic X-rays scattered on a crystalline sample. X-rays are generated in a cathode ray tube (e.g., Cu Kα on a Cu cathode), where a heated filament emits electrons that are accelerated toward a target material. Copper X-ray tubes are most commonly used for the diffraction of inorganic materials, with a wavelength of 1.54 Å.[53] In fact, the sample lattice behaves like a diffraction grating for the X-rays. The diffracted X-rays, obeying Bragg's law, are detected. The Bragg's law establishes a relationship between the wavelength of the electromagnetic radiation, the lattice spacing, and the diffraction angle:

$$n\lambda = 2d\sin\theta, \qquad (1)$$

where n is the order of reflection, λ X-ray wavelength, d spacing distance and θ is the angle of diffraction beam.[53]

The sample is scanned through a range of 2θ angles, allowing all possible diffraction directions to be captured due to the random orientation of crystals in powdered materials. This produces characteristic X-ray spectra due to the interaction of electrons with the material. The resulting diffraction pattern comprises peaks that are unique to each crystalline substance enabling identification by comparison with standard reference patterns.[54] In contrast to single-crystal XRD, which provides detailed atomic structure from a single, well-ordered crystal, powder XRD gives an averaged diffraction pattern from many randomly oriented crystallites, making it ideal for phase identification and crystallinity assessment.

2.3.2 Physisorption analysis of textural properties

Textural properties, such as specific surface area, pore size distribution, and pore volume are important characteristics of porous materials. One of the most widely used techniques for determining the textural properties of zeolites is the physisorption analysis of gas molecules at their boiling point. Physisorption (physical adsorption) involves weak Van der Waals interactions between gas molecules (adsorbate) and the surface of a solid material (adsorbent). It is described by adsorption isotherms, which show how much gas is adsorbed at given (relative) pressure at constant temperature.[55] N_2 and Ar are commonly used for standard textural property measurements. Nitrogen is preferred due to its availability and cost, while argon (being a sphere) provides more accurate data for characterising microporous materials like zeolites. However, it is unsuitable for zeolites with narrow 8-membered ring channels due to diffusion limitations.[56–58]

Physisorption analysis typically involves the following steps: degassing, where the sample is treated under vacuum or inert gas flow at elevated temperatures to remove adsorbed contaminants such as water; adsorption measurement, where the sample is exposed to an increasing amount of adsorbate gas at a constant temperature, and the amount adsorbed is recorded; desorption isotherm measurement, where the pressure is gradually decreased, and the amount of desorbed gas is measured to determine pore size distribution and hysteresis behavior.[58]

Based on Langmuir's adsorption theory, which assumes monolayer coverage, the Brunauer-Emmett-Teller (BET) model extends this theory by accounting for multilayer adsorption and is widely used for evaluating the specific surface area of solid materials through gas physisorption.[59] The t-plot method is used to determine the volume of micropores and external surface area by comparing the obtained adsorption isotherm with a standard isotherm of a nonporous solid material that has similar surface chemistry. This method provides a correlation between the statistical film thickness (t) and the relative pressure.[60]

2.3.3 Ultraviolet-visible reflectance spectroscopy

Ultraviolet-visible (UV-Vis) diffuse reflectance spectroscopy is a non-destructive tool for confirming the incorporation of heteroatoms (i.e., Zr, Sn) into the zeolite framework. Unlike traditional transmission UV-Vis spectroscopy that follows the Lambert-Beer law,

this technique uses the Kubelka-Munk function to account for light scattering on opaque material. Spectra are obtained by evaluating the Kubelka-Munk function at specific wavelengths and showing absorption peaks, which are characteristic of the incorporated elements and their bonding environment in the zeolite framework.[61,62] Tetrahedrally coordinated Sn^{4+} in zeolite framework has a peak centred around 220 nm, while extra-framework species (SnO_2) absorb in the range from 260 to 280 nm.[63] Similarly, the Zr atom within the framework exhibits absorption between 205-215 nm, whereas ZrO_2 has a peak at 240 nm.[64] However, this method provides qualitative data, since spectral intensity is influenced by poorly defined factors like crystal size and sample packing density.[19]

2.3.4 Elemental composition analysis by inductively coupled plasma-mass spectroscopy

Analysing the elemental composition of materials is important for understanding the behaviour of our heterogeneous catalysts. In this study, inductively coupled plasma-mass spectrometry (ICP-MS) was utilized to determine the Si/*M* ratio, where *M* signifies the heteroatom incorporated during synthesis. The principle of this method stands on the ionizing of the sample in an argon plasma, followed by mass spectrometric analysis to quantify the ions based on their mass-to-charge ratio. ICP-MS is highly sensitive, capable of detecting elements at concentrations up to 100s or even 1000s of parts-per-million (ppm), making it ideal for biological and material science applications.[65]

2.3.5 Scanning electron microscopy

Scanning electron microscopy (SEM) is a type of electron microscopy for the characterization of solid materials, providing detailed information about surface morphology, and crystal aggregate size. However, since SEM has limited resolution, it cannot provide direct insight into the internal structure of zeolites. The working principle of SEM is based on the interaction of a focused electron beam with the sample.[66] Electrons are generated by an electron gun and then accelerated by a positive electric potential, while electromagnetic lenses shape and focus the electron beam. When the incident electron beam interacts with the sample, several types of electrons are generated, including secondary electrons and backscattered electrons. The intensity and angle of emitted electrons are detected and processed to construct a detailed image of the sample.[66,67] The resolution

achievable under these conditions is on the order of a few nanometres, allowing for high-resolution imaging of the zeolite surface.

2.3.6 Quantification of acid sites in zeolites

The quantification of acid sites in zeolites is crucial for understanding their catalytic properties and predicting their performance in different reactions. The acid sites in zeolites are generally classified as Brønsted and Lewis acid sites, each contributing differently to catalytic activity. Therefore, various techniques have been developed to determine their concentration, strength, and distribution.[39] The most commonly used approach is FTIR spectroscopy of probe molecules (acetone or d_3-acetonitrile)[40], which are used to identify and (semi)quantify Lewis acid sites in our catalysts. The adsorption of d_3-acetonitrile produces spectra with characteristic vibrational bands that distinguish different types of Lewis acid sites: the ν(C≡N) band at 2306 cm^{-1} corresponds to interactions with "open" Zr sites.[41] In addition, according to reference[36], a weak band at 2295 cm^{-1} was attributed to d_3-acetonitrile hydrogen-bonded to Zr-OH groups of Zr "open" sites. However, d_3-acetonitrile does not interact with "closed" sites (the reason is unknown), so a different probe molecule is needed for their identification. In Sn-beta, both characteristic bands are detected, at 2316 cm^{-1} for "open" sites and 2304 cm^{-1} for "closed" sites.[68] For reference, the ν(C≡N) stretching vibration of pure liquid acetonitrile appears at 2253 cm^{-1}, but in d_3-acetonitrile is single clear C≡N band at 2262 cm^{-1}, which makes it more suitable for IR spectroscopic studies of adsorption on zeolites.[69] Recently, our group started using acetone to probe Zr Lewis acid sites. The acetone adsorption spectra show ν(C=O) bands shifting to lower wavenumbers due to interactions with Lewis acid sites. The stronger Zr "open" sites have a band at 1698 cm^{-1}[70], while a second band at 1709-1712 cm^{-1} corresponds to weaker Zr "closed" sites[71]. The Sn "open" sites exhibited a band at 1688 cm^{-1}, while the "closed" Sn sites were identified by the band at 1695 cm^{-1}.[36,68] Beyond FTIR analysis, NMR is particularly useful for characterising Lewis acid sites.[72] UV-Vis spectroscopy provides further qualitative insight into the coordination environment of metal species in the zeolite framework and their concentration.[63]

3 Working hypothesis

We hypothesise that nitrogen-containing bases, particularly amines, coordinate to the Lewis acid sites of Zr-containing beta zeolites and selectively modify their catalytic properties rather than deactivating them. We propose that this modification, through the formation of zeolite–amine complexes, influences the reaction mechanism of Lewis acid-catalysed processes occurring over Zr-based zeolites.

This study focuses on the MPV reduction of citronellal with 2-propanol over Zr-beta zeolites in the presence of pyridine-derived bases and N-methylpiperidine. The aim is to understand how these bases affect both catalyst activity and product selectivity. We propose that the coordination of the base to the Zr active sites is essential and causes a change in the intrinsic reaction mechanism. Accordingly, we expect two key parameters: the molecular size of the base and the steric accessibility of its nitrogen atom to control the effect. pKa was excluded before as a driving parameter. Smaller bases diffuse more easily into the zeolite pores and are more likely to form internal active Zr sites-amine complex, enhancing their ability to influence the catalytic behaviour. Finally, we propose that chiral amine–zeolite complexes may induce stereoselectivity in the MPV reduction of prochiral ketones.

4 Experimental part

4.1 List of used chemicals

The chemicals used for the synthesis of zeolites and catalytic testing are listed in Table 1.

Table 1: List of chemicals used for synthesis of zeolites and catalytic experiments

Name	Purity	Manufacturer
2-propanol	≥98%	VWR Chemicals
2,4,6-collidine	99%	Thermo Scientific
2,5-lutidine	95%	Sigma Aldrich
2,6-ditert-butylpyridine	97%	Sigma Aldrich
3-methylcyclohexanol	98%	Sigma Aldrich
3-methylcyclohexanone	97%	Sigma Aldrich
3,5-lutidine	99%	Thermo Scientific
Al-beta (CP811E; Si/Al = 68)		Zeolyst Int.
Citronellal	96%	Alfa Aesar
Citronellol	92%	TCI
Hydrofluoric acid	40%	VWR Chemicals
Isopulegol	97%	Alfa Aesar
Mesitylene	98%	Sigma Aldrich
N-methylpiperidine	99%	Acros Organic
Nitric acid	65%	Lach-ner
Pyridine	99.8%	Sigma Aldrich
(R)-1-methyl-2-pyrrolidinemethanol	97%	Sigma Aldrich
(S)-(-)-1-methyl-2-pyrrolidinemethanol	96%	Sigma Aldrich
Tetraethylammonium hydroxide	35%	Thermo Scientific
Tetraethyl orthosilicate	100%	VWR Chemicals
Tin(IV) chloride	98%	Sigma Aldrich
Zirconium(IV) chloride	99.9%	Sigma Aldrich
Zirconium(IV) isopropoxide	99.9%	Sigma Aldrich

4.2 Synthesis of the catalysts

4.2.1 Preparation of beta seeds

The first step of all synthesis was dealumination of beta seeds, which are precursor crystals. We used dealuminated commercial Al-beta zeolite as seeds. The Al-beta dealumination was performed as follows: 1 g of Al-beta (CP811E; Si/Al = 68, Zeolyst Int.) was mixed with 20 ml of 65% aqueous solution of nitric acid and stirred in a 50 ml flask while heating (100 °C) for 18 hours. After this period, the mixture was diluted with at least 100 ml of distilled water, then filtered, washed with 200 ml of water, and dried at 60 °C. The dried powder sample was used in the next step of synthesis.

4.2.2 Synthesis of Zr-beta-A, Zr-beta-B and Zr-beta-C

In this work, 3 batches of Zr-beta (labelled as Zr-beta-A, Zr-beta-B, and Zr-beta-C) were used and synthesised using a similar synthetic procedure, with the composition of the synthesis mixture listed in Table 2. In the case of Zr-beta-A, 35.17 g of tetraethyl orthosilicate (TEOS) was mixed with 35.45 g of 35 wt.% tetraethylammonium hydroxide (TEAOH). The mixture was stirred for 2 hours. Meanwhile, 0.181 g of anhydrous zirconium(IV) chloride was weighed out as the zirconium source, dissolved in 1.50 ml of distilled water and then added dropwise to the TEOS-TEAOH mixture. After this, 1.000 g of beta seeds (dealuminated zeolite beta CP811E) was added to promote crystal growth, followed by the addition of 3.52 g 48 wt.% hydrofluoric acid. The thick gel was homogenised with a spatula and then transferred to Teflon-lined autoclave. The 90ml autoclave was put into an oven pre-heated to 140 °C to crystallise, which lasted for 11 days. Afterward, the solid product was recovered through centrifugation, washed with distilled water, and dried. For synthesis of Zr-beta-B, the procedure was the same as for Zr-beta-A except the amount of zirconium source was increased to 0.729 g of the anhydrous zirconium(IV) chloride. Specifically, the composition of the synthesis mixture was 35.17 g of TEOS, 35.46 g TEAOH, and 0.729 g of zirconium(IV) chloride and the hydrothermal synthesis occurred for 17 days. After the given time, the sample was cooled down to room temperature, centrifuged, and dried at 60 °C. Finally, the samples were calcined in air at 550 °C for 6 hours with a heating rate of 2 °C/min.

Zr-beta-C was prepared using a slightly different approach. First, 28.16 g of TEOS and 31.79 g of TEAOH were mixed for 15 minutes to homogenise the mixture. Then, 0.295

g of zirconium(IV) isopropoxide as zirconium source was added directly to the mixture and stirred overnight. In the next step, 3.02 g 50 wt.% HF and 0.281 g of dealuminated beta seeds, which were prepared in the first step and dispersed in the 2.7 g of distilled water, were added to the synthesis mixture. The resulting gel was transferred to a Teflon-lined autoclave and heated at 140°C under static conditions for 20 days. After crystallisation, the product was filtered, washed with 500 ml of distilled water and dried at 60 °C overnight. The calcination process was the same as above.

4.2.3 Synthesis of Sn-beta

The synthesis of Sn-beta followed the procedure for Zr-beta-A. 35.17 g of TEOS was mixed with 37.59 g TEAOH. Separately, 0.290 g of anhydrous tin(IV) chloride was dissolved in 1.50 ml of distilled water and then added to the synthesis mixture. The resulting mixture was stirred at 100 °C until all ethanol, generated during hydrolysis of TEOS, had evaporated completely. Afterward, 1.002 g of the zeolite dealuminated beta seeds prepared in the first step were added to the mixture, followed by 3.72 g of HF. The mixture was then transferred to a steel autoclave with a Teflon liner, which was sealed and placed in the oven at 140 °C for 11 days. After the given time, the autoclave was removed from the oven, cooled down and the solid product was separated by centrifugation. The crude product was washed with deionized water and left to dry at 60 °C. The same calcination conditions mentioned earlier were applied to Sn-beta.

Table 2: Composition of synthesis mixtures for each prepared material

[g]	Zr-beta-A	Zr-beta-B	Zr-beta-C	Sn-beta
TEOS	35.17	35.17	28.16	35.17
TEAOH	35.45	35.46	31.79	37.59
H_2O	1.50	1.50	2.70	1.50
$ZrCl_4$	0.181	0.729	-	-
$Zr(OCH(CH_3)_2)_4$	-	-	0.295	-
$SnCl_4$	-	-	-	0.290
Beta seeds	1.000	1.000	0.281	1.002
HF	3.52	3.52	3.02	3.72

4.3 Zeolite sample characterization

The structure of the prepared zeolites was analysed using powder X-ray diffraction (PXRD). Measurements were carried out on a Bruker D8 Advance diffractometer equipped with LYNXEYE XE-T detector, utilizing Cu Kα radiation (λ = 0.15406 nm). The powdered zeolite samples were ground, pressed onto a plastic holder and aligned using a glass for a smooth surface. All the samples were measured in the 5-40 °C 2θ range in 2000 steps with 0.8 s time per step. The diffraction patterns that we obtained were compared with the literature.[17]

Textural properties of the zeolites were evaluated using nitrogen sorption isotherms measured at -196 °C with Micrometrics 3Flex volumetric surface area analyser. Before analysis, the samples were degassed using a Micromeritics Smart Vac Prep instrument equipped with a turbomolecular pump vacuum. The process involved heating the catalyst to 110 °C (heating rate 1 °C/min), until a residual pressure of 13.3 Pa was achieved, followed by maintaining this temperature for 1 hour. Subsequently, the temperature was increased to 250 °C using the same rate and held for 8 hours. The BET surface area (S_{BET}) was calculated from the adsorption data within the relative pressure range of p/p^0 = 0.05-0.20, while the external surface area (S_{ext}) and micropore volume (V_{micro}) were determined using the t-plot method. The total pore volume (V_{tot}) was derived from the adsorbed amount of nitrogen at p/p^0 = 0.95, representing the total adsorption capacity. These measurements provided comprehensive insight into the textual characteristics of the prepared zeolites. Measurement was done with the help of Ing. Martin Kubů, Ph.D.

UV-Vis spectra were obtained using an Agilent Cary 4000 UV-Vis spectrometer equipped with a $BaSO_4$ integration sphere against $BaSO_4$ 100% reflectance standard, covering a wavelength range of 190-600 nm. The measurements were carried out with the assistance of Ing. Jan Přech, Ph.D., and the recorded spectra were transformed into absorption spectra using the Kubelka-Munk function.

The elemental content of the catalyst (Si, Zr and Sn) was quantified using Agilent 7900 ICP-MS instrument. For the measurement, 50 mg of the catalyst was mixed with 1.8 ml of 67-69% HNO_3, 5.4 ml of 34-37% HCl and 1.8 ml of 47-51% HF. The resulting solution was then transferred into a sealed Teflon vessel and heated in a microwave oven (Speedwave® XPERT, Berghof) at 210 °C with a temperature ramp of 5 °C per minute for 25 minutes.

After a certain time, the mixture was allowed to cool down and the excess of HF was complexed by adding 16 ml of boric acid, followed by further microwave treatment at 190 °C (5 °C/min) for 10 minutes. Finally, the cooled solution was diluted with deionized water before analysis. These measurements were performed by Ing. Martin Kubů, Ph.D.

SEM images were obtained using a Thermo Fisher Scientific Scios 2 DualBeam SEM microscope, which is equipped with a Schottky field emission gun. The sample morphology was examined using the in-lens Trinity Detector T2 for secondary electron imaging with the T1 detector. An infrared CCD camera was used for image acquisition. The imaging conditions for both T1 and T2 detectors were set at an accelerating voltage of 2 kV, a beam current of 13 pA, and a working distance of 4 mm. Elemental composition analysis was performed using energy-dispersive X-ray spectroscopy (EDX) with the UltraDry X-ray detector integrated into the SEM apparatus. The analysis covered the entire image area, employing an accelerating voltage of 10 kV, a beam current of 1.6 nA, and a working distance of 7 mm. All samples were mounted on conductive carbon tape affixed to the SEM holder.

Semiquantitative FTIR adsorption analysis was carried out using acetone as a probe molecule. The spectra were recorded using a Nicolet iS50 spectrometer with a transmission MTC/B detector with a resolution of 4 cm^{-1}. The zeolite samples were pressed into self-supporting wafers and then saturated with an excess of the probe molecule at room temperature under a pressure of 732 Pa. To remove excess physisorbed molecules, the cell was outgassed for 20 minutes at 50 °C for acetone. All spectra were normalised to the same sample density, specifically ($10\ mg \cdot cm^{-2}$).

4.4 Catalytic reactions

4.4.1 Activation of the catalysts

All catalysts were activated in a ceramic plate before every catalytic experiment. Initially, 200, 100 or 20 mg of each catalyst was weighed and heated in a laboratory furnace at 450 °C for 6 hours, with a heating rate of 2 °C per minute. Afterward, the catalyst was carefully transferred to a desiccator (at a temperature of approx. 150 °C) to cool down.

4.4.2 Description of basic experiment (citronellal with 2-propanol)

This section describes the parameters of the typical reference experiment, performed in this thesis. In each subsequent section, only specific reaction conditions and the

composition of the mixture will be modified while maintaining this procedure. The compositions and ratios of the reaction mixture used in each experiment are listed in Table 3.

The citronellal reaction with 2-propanol took place in a 25ml round-bottom flask with two necks, equipped with a magnetic stir bar. Each flask, functioning as a reactor, was sealed with a septum on one side and connected to a Dimroth condenser on the other. This setup prevented the loss of volatile components by condensing vapours back into the reaction mixture. Before starting the reaction, the catalyst was activated (see Section 4.4.1 Activation of the catalysts) and its exact mass was carefully weighed after removal from the furnace. Amounts of the other reagents were adjusted according to this measured value to keep constant compound ratios in all experiments. The catalyst (the standard amount is 100 mg) was then added to the flask along with 78.5 mmol of 2-propanol (6 ml). The flask was heated to the desired temperature (70 °C) using a hot plate magnetic stirrer, StarFish^{TM} apparatus. To ensure consistent heating and minimize heat loss, the flask was insulated with cotton wool and wrapped in aluminium foil. Once the target temperature was reached, the reaction was initiated by adding prepared mixture of 180 µl of mesitylene (used as an internal standard) and 2.2 mmol of the substrate (0.4 ml of citronellal). Immediately after the substrate addition, approximately 250 µl of the mixture was withdrawn using a syringe to serve as the "zero" sample. This sample was centrifuged at 5000 rpm for 5 minutes to separate the liquid phase from the catalyst. The separated liquid phase was then transferred to a new vial for analysis. Samples were collected at defined time intervals throughout the reaction, as specified for each experiment below. The samples were then analysed using a gas chromatograph (GC) Agilent 7890B, equipped with an autosampler, a flame ionisation detector (FID) and VF-WAXms column (30m x 250 µm x 1 µm). Nitrogen was used as the carrier gas at a flow rate of 0.7 ml·min^{-1}. The detector and inlet temperatures were set to 250 °C and the column operated isothermally at 165 °C. Each sample analysis took 18 minutes to measure.

4.4.3 Study of citronellal reaction and the influence of pyridine-derived bases

For the citronellal reaction without a base, the reaction mixture contained 20 mg of the catalyst (used in a reduced amount from standard 100 mg to slow down the reaction for effective sampling), 78.5 mmol of 2-propanol, 180 µl of mesitylene and 2.2 mmol of citronellal. The reaction was conducted at 70 °C and samples were collected at intervals throughout the reaction: 0, 0.5, 1, 3, 5 and 6 hours.

The citronellal reaction was then studied with pyridine and various substituted pyridines: 2,5-lutidine, 3,5-lutidine, 2,4,6-collidine and 2,6-ditert-butylpyridine. Once the mixture of 2-propanol with 20 mg of catalyst in the flask reached the desired temperature (70 °C), the base was added to the reaction mixture. The amount of base was calculated to be a 1:1 molar ratio between the base concentration and concentration of heteroatom in the used catalyst, which was determined by ICP-MS analysis. 15 minutes after the addition of the base, the reaction was initiated by the introduction of a prepared mixture of citronellal with mesitylene. Sampling and analysis were the same as for the reaction without the presence of the base.

4.4.4 Kinetic study of MPV reduction

For the kinetic study, the experimental setup followed the procedure described in Section 4.4.2 , with three key modifications: the reaction mixture volume was doubled, the amount of catalyst (Zr-beta-A or Sn-beta) was 40 mg for base-free reaction (to slow down the reaction for efficient sampling) and increased to 200 mg for reactions with bases, where a higher catalyst loading was needed due to slower reaction rates. The experiments were conducted over a temperature range of 40-80 °C for Zr-beta-A and 50-80 °C for Sn-beta. Specifically, the reaction mixture consisted of 40 or 200 mg of the catalyst, 12 ml of solvent (157 mmol), 360 µl of mesitylene and 4.4 mmol of substrate (800 µl citronellal). The study was performed at temperature intervals of 10 °C, specifically at 40, 50, 60, 70 and 80 °C. To ensure more accurate kinetic results, sampling was performed at shorter intervals: 0, 0.5, 1, 1.5, 2, 2.5, 3, 4, 5 and 6 hours.

For the reactions involving bases (pyridine and N-methylpiperidine), the experimental procedure remained the same as for the base-free reactions except for the addition of the base. The base-to-substrate molar ratio was 1:10, specifically 0.44 mmol of base for 4.4 mmol of substrate. Once the flask containing 2-propanol and catalyst reached the reaction temperature (40-80 °C), 0.44 mmol of the base (35.4 µl of pyridine or 43.5 µl N-methylpiperidine) was added. The mixture was then allowed to react with the base for 15 minutes. After that, the reaction was initiated by the addition of mesitylene-substrate mixture. Sampling and analysing were conducted in the same manner as above.

4.4.5 Influence of chiral base on the MPV reduction of prochiral ketones

To investigate the potential for chiral induction in the MPV reduction of prochiral ketones such as 3-methylcyclohexanone, chiral bases ((R)-1-methyl-2-pyrrolidinemethanol, and (S)-(-)-1-methyl-2-pyrrolidinemethanol) were tested in the reaction. The experiments were performed with individual enantiomers of the chiral base and subsequently with its racemic mixture. The reaction was carried out in 25ml round-bottom flasks using 2-propanol as solvent over 100 mg Zr-beta-B catalyst at 82 °C under stirring at 450 rpm using StarFish™ apparatus. The reaction mixture consisted of 83 mmol of 2-propanol, 1.4 mmol of mesitylene (as internal standard), 2.6 mmol of 3-methylcyclohexanone (as prochiral ketone) and 0.26 mmol of the chiral base. The reaction procedure for the base-free reaction was the same as for the MPV reduction of citronellal. The catalyst with solvent was first heated to 82 °C in the flask. The base was then added, and after 20 minutes, the mixture of substrate and mesitylene was introduced to the flask to initiate the reaction. Samples were collected at defined time intervals: 0, 1, 2, 4, and 24 hours. Each sample was centrifuged, and the separated liquid phase was analysed by GC Agilent 8890 equipped with FID and with HP Chiral 20B column (30m x 0.25mm x 0.25 µm). The column operated using a temperature program starting at 110 °C for 2 minutes, followed by a ramp of 10 °C/min to 150 °C, which was held for 8 minutes.

Table 3: Summary of reaction mixture compositions for each experiment

	catalyst [mg]	2-propanol [mmol]	mesitylene [mmol]	citronellal [mmol]	base
Study with pyridine-derived bases	20	78.5	1.3	2.2	1 eq. base: heteroatom in used catalyst
Kinetic study	40[a]/200[b]	157	2.6	4.4	0.44 mmol
Study with prochiral bases	100	83	1.4	2.6	0.26 mmol

[a] *Catalyst amount in base-free reaction in kinetic study*
[b] *Catalyst amount in reactions with added bases in kinetic study*

4.4.6 GC Calibration and data evaluation

For the GC calibration of the citronellal reaction, a mixture of 2-propanol (solvent), citronellal (aldehyde), and citronellol (corresponding alcohol and product of MPV reduction) was used, along with isopulegol, as the reaction of citronellal with 2-propanol proceeds through other 2 pathways over Lewis acid zeolites. These include en-al cyclization

(forming isopulegol) and acetalization (forming citronellal diisopropylacetal). The response coefficients (*K*) for citronellol and isopulegol were determined as the ratio of the slopes of the individual product and substrate calibration curves, as described in my bachelor thesis[3]. For citronellal diisopropylacetal, the coefficient was estimated based on its molar mass and its chemical composition. The calibration curve for 3-methylcyclohexanone reaction was prepared according to the same procedure as for citronellal, also described in my bachelor thesis[3]. An overview of the response coefficients used for all analysed compounds is listed in Table 4.

Table 4: Table of response coefficients

	Response coefficient
citronellal/citronellol	0.978
citronellal/isopulegol	0.963
citronellal/citronellal diisopropylacetal	0.625
3-methylcyclohexanone/3-methylcyclohexanol	0.943

The measured data were evaluated in terms of conversion (*X*) and yield (*Y*) using an internal standard and response corrected peak areas according to equations 2 and 3. In these equations, A_0 represents the initial peak area of the substrate (aldehyde or ketone), while A_i corresponds to the substrate peak area at a specific time of the reaction. Similarly, $A_{\mathrm{Std,0}}$ denotes the initial peak area of the internal standard, and $A_{\mathrm{Std,i}}$ represents the internal standard peak area at given time. *K* denotes the specific response coefficient for each product calculated in calibration. Selectivity was calculated as the ratio of yield to conversion (eq. 4). Rate of conversion is defined according to equation 5 and is comparable only between experiments with the same amount of the catalyst.

$$X = \frac{\frac{A_0}{A_{Std,0}} - \frac{A_i}{A_{Std,i}}}{\frac{A_0}{A_{Std,0}}} \tag{2}$$

$$Y = \frac{\frac{A_i}{A_{Std,i}}}{\frac{A_0}{A_{Std,0}}} \cdot K \tag{3}$$

$$S = \frac{Y}{X} \tag{4}$$

$$\text{rate of conversion} = \frac{\mathrm{d}X}{\mathrm{d}t} \tag{5}$$

4.4.7 Evaluation of activation energy and kinetic analysis of individual reaction pathway

The data obtained from catalytic experiments were measured on GC and further processed by calculating the absolute concentration of the individual substrates and products at a given time. Firstly, the amount of substrate added to the reaction was calculated from the known density and its volume, which was then converted into moles using the molar mass of the compound. The absolute concentration (in $\mathrm{mol} \cdot \mathrm{l}^{-1}$) was obtained by dividing the number of moles by total reaction volume (in litres). Since GC data are measured at time zero and at subsequent time points, the ratio of the GC area at each time to the initial GC area was calculated. This ratio was then multiplied by the initial concentration to estimate the concentration at each time. In this way, the concentration over time was known and used for further calculations.

The integral method was used to estimate the apparent reaction order for each reaction pathway by comparing experimentally measured concentration over time with theoretically derived integrated rate equations for different reaction orders (e.g., zero, first, or second order). The reaction order was identified based on which plot showed a linear dependence.

Data for kinetic study were collected across a temperature of 40-80 °C at regular intervals over a 6-hour period, yielding comprehensive concentration on time database for all key reaction products. The experimental data were fitted with the kinetic model using the Easy Regression Analysis (ERA) program 3.0[73], a specialised kinetic modelling software developed for evaluation of kinetic data from heterogeneous catalysis experiments. The program enables precise optimization of rate constants (model parameters) and their confidence limits through nonlinear regression analysis.

The apparent activation energy (E_A) for each reaction pathway was determined using the Arrhenius plot. Specifically, an Arrhenius plot was constructed by plotting the natural logarithm of the corresponding rate constants ($\ln(k)$) against the reciprocal of the absolute temperature ($1/T$). The activation energy was then evaluated from the slope of the linear fit using the Arrhenius equation:

$$k = A \cdot e^{-E_A/RT} \qquad (6)$$

, where k represents the rate constant, A is the preexponential factor, R is the universal gas constant ($8.314\ \mathrm{J} \cdot \mathrm{mol}^{-1} \cdot \mathrm{K}^{-1}$) and T denotes the absolute temperature in Kelvin.

5 Results

5.1 Characterization of prepared zeolites

The primary objective of the characterization is to confirm that the synthesised zeolite samples are phase-pure and exhibit the desired physico-chemical properties. This includes verifying the successful incorporation of heteroatoms (in our case, Sn or Zr) into the zeolite framework.

The Zr-beta-A, Zr-beta-B, Zr-beta-C, and Sn-beta were prepared by seed-assisted hydrothermal synthesis, and their crystal structures were confirmed by PXRD analysis. The measured diffraction patterns were compared to the theoretical pattern of beta zeolite, referencing data from the IZA database[17], which consist of an intergrowth of polymorphs beta A and B in 50:50 ratio. The X-ray diffractograms of the prepared and calcined Zr-beta samples (Figure 4) and Sn-beta (Figure 5) showed patterns (meaning presence and position of the peaks) that closely matched those of the reference beta, confirming that the desired structure was successfully obtained in all four synthesised samples. However, the peak at 17° 2θ in Zr-beta-B is unexplained, though we have ruled out ZrO_2, dense SiO_2 phases (quartz) and other zeolites.

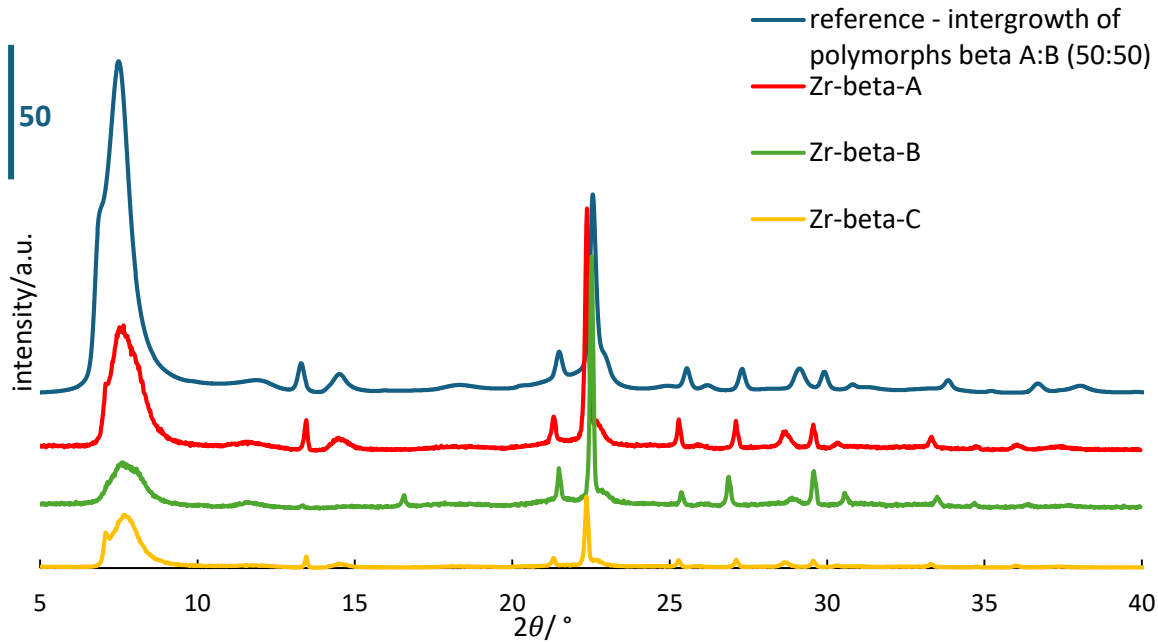

Figure 4: XRD patterns of calcined Zr-beta zeolites. Reference XRD pattern of intergrowth polymorphs beta A and B were calculated and taken from IZA database.[17]

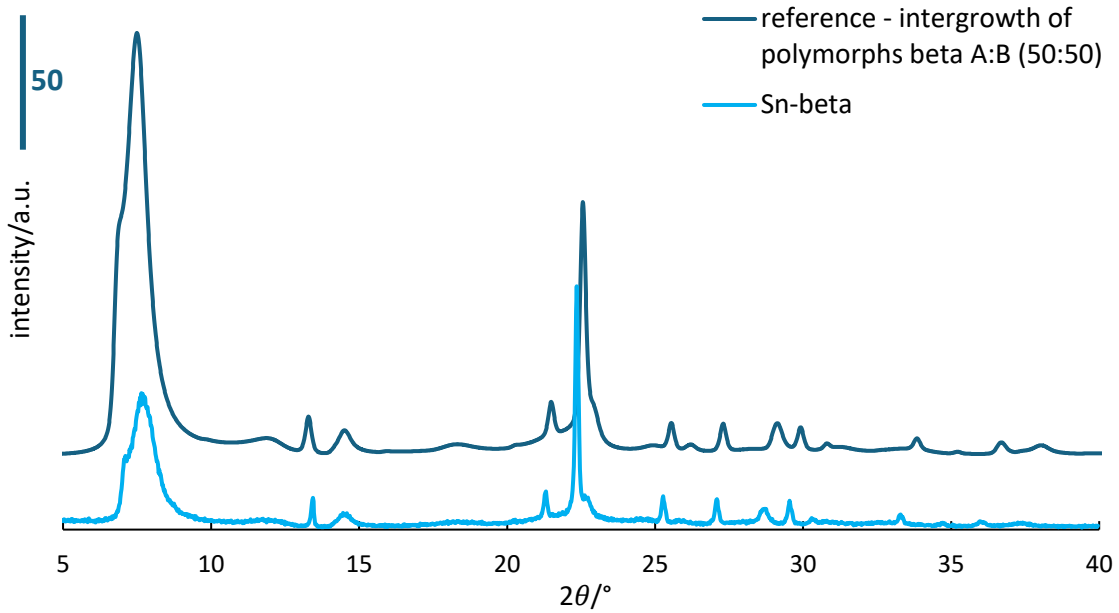

Figure 5: XRD pattern of synthesised Sn-beta zeolite after calcination with reference pattern from IZA database.[17]

Nitrogen sorption measurements were performed to investigate the textural properties of synthesised materials (values in Table 5). The highest BET surface area was observed for Zr-beta-A (631 $m^2 \cdot g^{-1}$) followed by the other 3 materials with relatively same values (579 $m^2 \cdot g^{-1}$ Zr-beta-B, 574 $m^2 \cdot g^{-1}$ Sn-beta, and 517 $m^2 \cdot g^{-1}$ for Zr-beta-C). The highest external surface area was observed for Zr-beta-B (106 $m^2 \cdot g^{-1}$). The values of total pore volume ranged from 0.25 to 0.28 $cm^3 \cdot g^{-1}$, while micropore volumes varied between 0.19 and 0.22 $cm^3 \cdot g^{-1}$ across the prepared materials. These measured values are consistent with those reported in the literature.[64] The Si/*M* ratios obtained from ICP-MS analysis were compared with the theoretical values based on synthesis gel composition. While Zr-beta-B showed agreement in the values (53 measured vs. 54 theoretical), indicating efficient Zr incorporation into the zeolite framework, Zr-beta-A (179 vs. 217) and Zr-beta-C (280 vs. 206) showed deviations in opposite directions. Zr-beta-A has a lower Si/Zr ratio than expected, suggesting more Zr was incorporated than anticipated, while Zr-beta-C exhibits a higher ratio, pointing to less efficient incorporation. For Sn-beta, the measured Si/Sn ratio (139) was slightly lower than the theoretical value (167), suggesting good incorporation of Sn species. Overall, these results confirm the presence of heteroatoms in the final material. However, their incorporation into the zeolite framework must be verified by spectroscopic methods.

Table 5: Measured and calculated textural properties of the used catalysts

		BET $[\mathbf{m^2 \cdot g^{-1}}]$	$\boldsymbol{S_{ext}}$ $[\mathbf{m^2 \cdot g^{-1}}]$	$\boldsymbol{V_{tot}}$ $[\mathbf{cm^3 \cdot g^{-1}}]$	$\boldsymbol{V_{micro}}$ $[\mathbf{cm^3 \cdot g^{-1}}]$	***Si/M***
Zr-beta	Zr-beta-A	631	74	0.26	0.21	179
	Zr-beta-B	579	106	0.28	0.22	53
	Zr-beta-C	517	63	0.25	0.20	280
Sn-beta	Sn-beta	574	79	0.28	0.19	139

UV-Vis spectroscopy was used to confirm the incorporation of metal species into the zeolite framework and to detect the possible presence of extra-framework (oxidic) species such as SnO_2. Framework tin atom in a tetrahedral coordination exhibits absorption band at 220 nm, while SnO_2 has a characteristic band at 260-280 nm.[63] In the UV-Vis spectra of Sn-beta (Figure 6), the presence of tetrahedrally coordinated Sn is evident from a band at 220 nm, confirming the Sn incorporation into the framework. Additionally, a less intense band around 260 nm suggests also the presence of extra-framework Sn oxide species. In contrast, the interpretation of the UV-Vis spectra of the Zr-beta catalysts was complicated by observed luminescence, which is inconsistent with the literature.[19] As an example, the FTIR spectrum of Zr-beta-A shown in Figure 7 (left) exhibits reflectance values exceeding 100% in the region of lower wavelengths, which is physically invalid and indicates spectral distortion. Furthermore, the baseline upward shift observed in the spectra (Figure 7, right) supports the presence of luminescence contamination, making the spectra uninterpretable in terms of zirconium coordination. Consequently, additional characterization techniques are required to verify the presence and nature of acidic sites. To address this, FTIR adsorption experiments with acetone and acetonitrile probe molecules were conducted (see below).

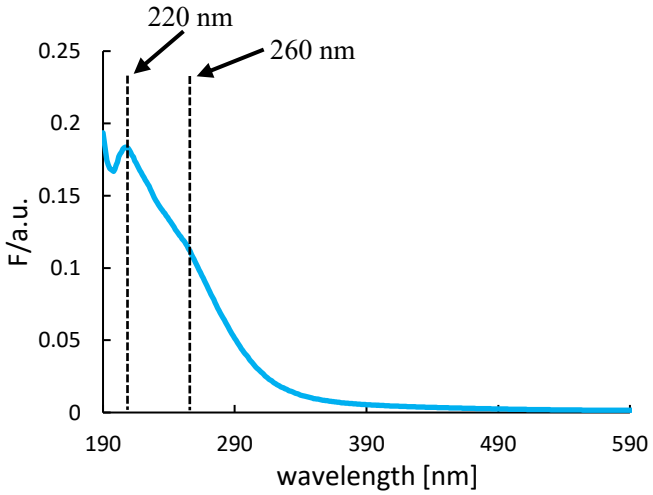

Figure 6: UV-Vis spectra of Sn-beta

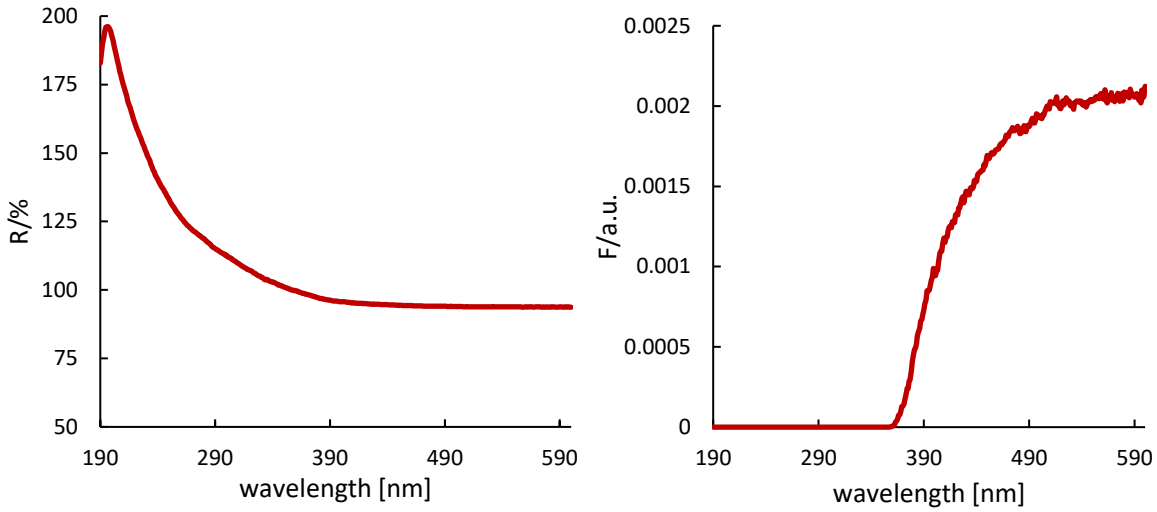

Figure 7: UV-Vis spectra of Zr-beta-A

FTIR spectroscopy of adsorbed acetone was performed to probe the nature and strength of Lewis acid sites in Zr-beta zeolites, with a particular focus on distinguish between "open" and "closed" sites. The FTIR spectra (Figure 8) after acetone adsorption and excess acetone desorption revealed ν(C=O) bands in the range of 1712-1690 cm^{-1}, indicating coordination of acetone to Lewis acid sites of the zeolites. Based on the theoretical background summarized in chapter 2.3.6 Quantification of acid sites in zeolites, a visible band at 1698 cm^{-1}, which evolves first, was assigned for all three catalysts to acetone interacting with stronger, "open" Lewis sites. In contrast, a broader and less intense band at 1709 cm^{-1}, was attributed to weaker, "closed" sites.[36] Observation of these Lewis sites also confirms the Zr incorporation.

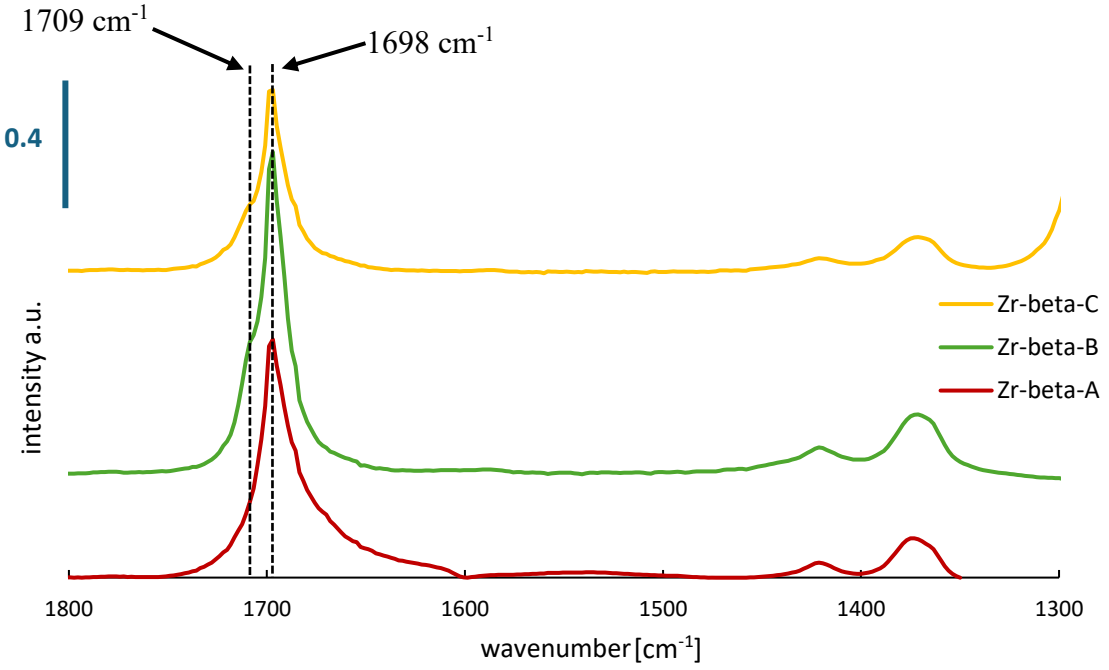

Figure 8: FTIR spectra of Zr-beta zeolites interacting with acetone

SEM was used to visualise the morphology of the prepared zeolites. In the case of Zr-beta-A (Figure 9), the SEM images show relatively uniform crystals resembling truncated octahedra, with the smallest ones measuring 300 nm, but mostly around 1 μm in size. The crystal surface displays a distinct stepped texture, suggesting the presence of terraces that may indicate the crystals are intergrowth of smaller subunits. The SEM images of Zr-beta-B (Figure 10) show aggregated crystals with sizes also around 1 μm, exhibiting rhombic shapes and fine structured surface features. SEM image of Zr-beta-C (Figure 11) shows uniform crystals (around 1 μm) with smooth facets, like for the Zr-beta-A. The analysis of Sn-beta (Figure 12) reveals well-defined, truncated octahedra shaped crystals with an average size of around 2 μm. Their surfaces are textured with terraces, and bright particles that are visible due to Z-contrast imaging. These bright spots are probably tin oxide particles, meaning that tin is not fully incorporated into the zeolite framework. This observation was further supported by the EDX map (Figure 13), which reveals distinct clusters of metallic tin corresponding to the locations of these bright spots. This confirms that the bright spots observed by backscattered electron detector are isolated SnO_2 particles on the surface of the zeolite. This finding is consistent with the UV-Vis spectrum, where a weak absorption band around 260 nm suggests the presence of extra-framework SnO_2 species. At the same time, a strong absorption band at 220 nm confirms that a significant amount of Sn is present in tetrahedral coordination within the zeolite framework. These results indicate that tin is present in both framework and extra framework forms. Notably, the absence of such bright particles in all Zr-beta samples suggests that zirconium is uniformly incorporated into the zeolite framework, with no presence of ZrO_2 particles. Both tin and zirconium belong to the 5th period of the periodic table, and thus they should exhibit similar Z-contrast.

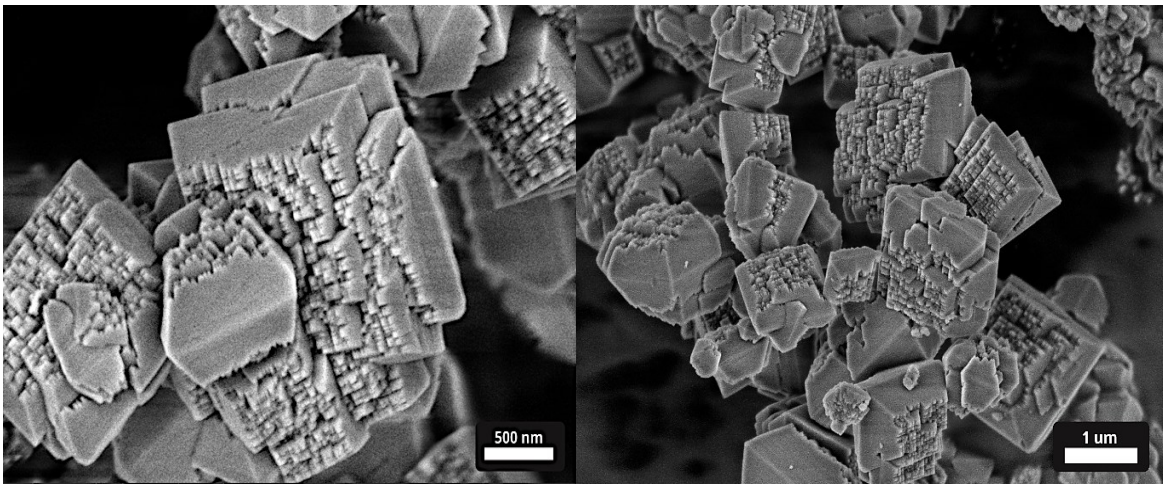

Figure 9: SEM image of Zr-beta-A

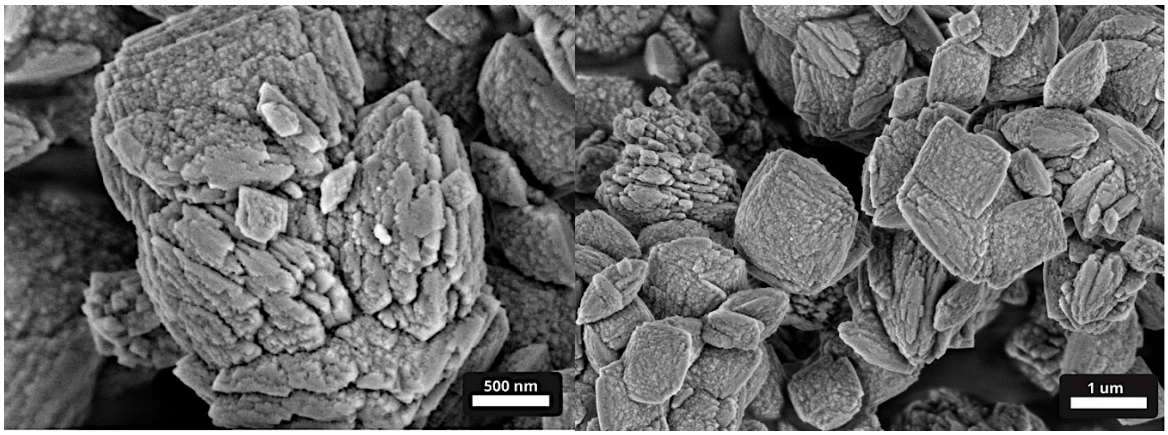

Figure 10: SEM image of Zr-beta-B

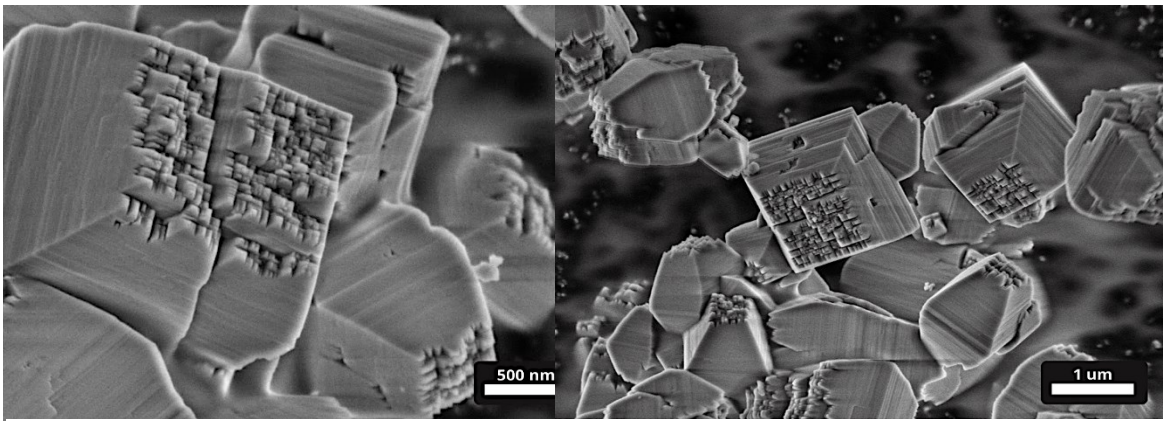

Figure 11: SEM image of Zr-beta-C

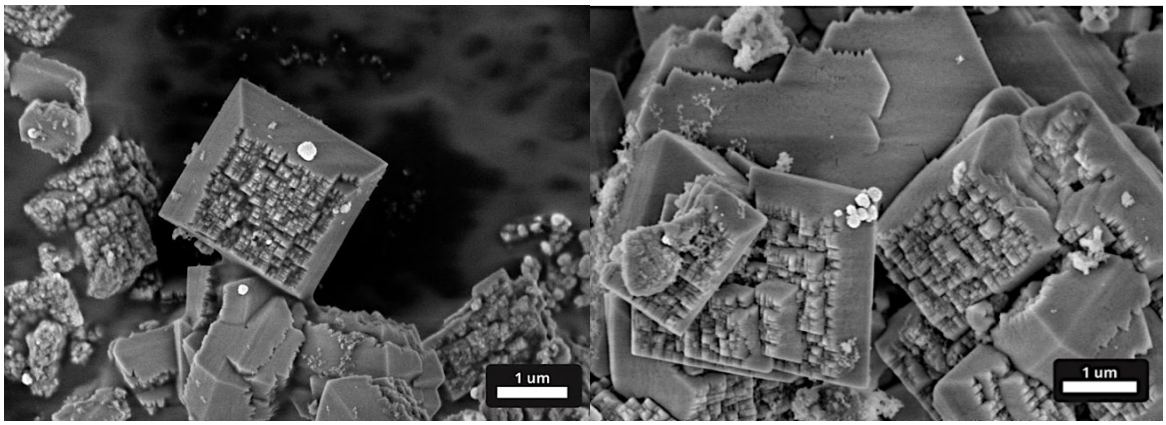

Figure 12: SEM image of Sn-beta

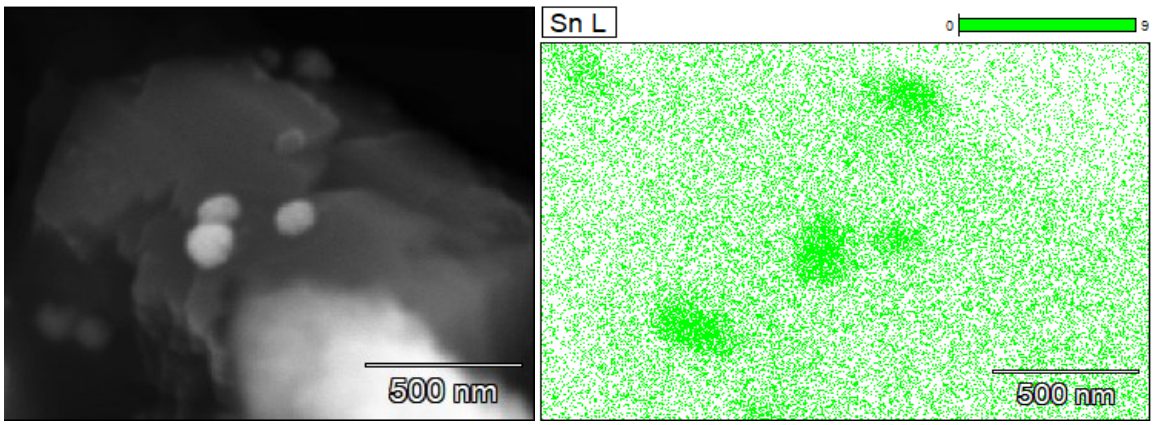

Figure 13: EDX map showing the spatial distribution of tin in Sn-beta

5.2 Catalytic experiments

5.2.1 Study of citronellal reaction with pyridine-derived bases

The reaction of citronellal with 2-propanol over Lewis acid zeolites is a complex process that can yield not only citronellol as the desired product but also side products formed through parallel reaction pathways (Figure 14). Namely, isopulegol is a product of intramolecular carbonyl-ene cyclization reaction, and citronellal diisopropylacetal is a product of the acetalization. Previous experiments have demonstrated that without the presence of a base, the dominant product is isopulegol in most cases (over both Zr-beta and Sn-beta). However, the addition of a base (for example pyridine) induces a selectivity shift towards citronellol, which becomes the main product of the reaction under these conditions.[3]

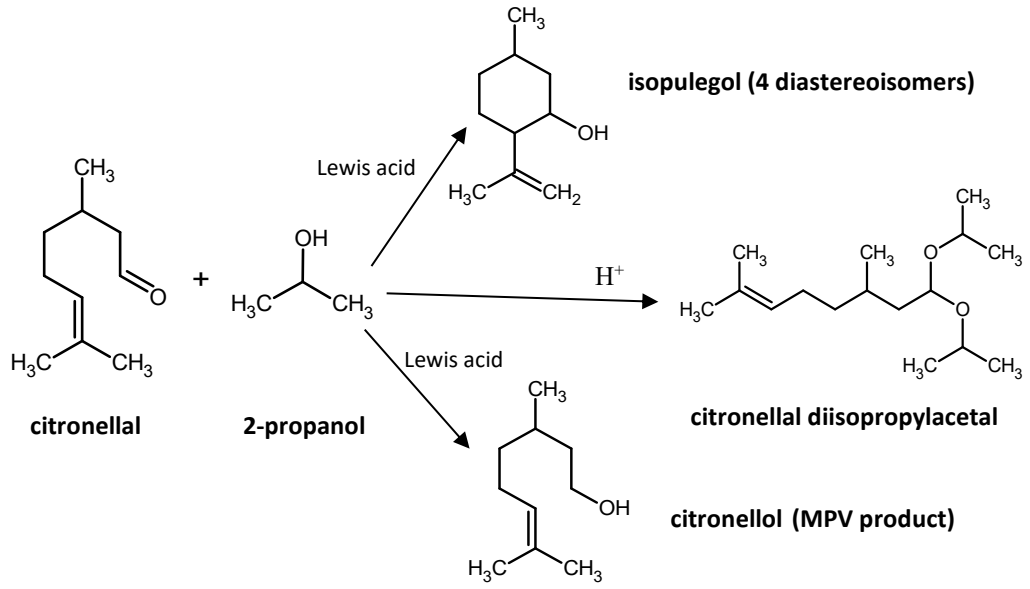

Figure 14: Reaction pathways of citronellal transformation in 2-propanol over Lewis acid zeolites

5.2.1.1 Standard base-free experiment of citronellal reaction with 2-propanol

Based on previous experiments from my bachelor thesis[3], it is already known that the citronellal reaction with 2-propanol, over Zr-beta catalyst, provides nearly complete conversion of citronellal after 6 hours of reaction in the absence of a base (at 70 °C using 20 mg catalyst and 2.2 mmol of citronellal and 78.5 mmol of 2-propanol). To confirm the reproducibility of the experiment, a series of three independent catalytic runs was conducted using 20 mg of the Zr-beta-B catalyst under identical reaction conditions. Figure 15 shows, all three experiments provided almost identical conversion curves, reaching 97% conversion after 6 hours. Also, the product distribution after 6 hours, shown in terms of selectivity in Figure 16, remained the same across all experiments. The selectivity was approximately 0.58 ±0.01 towards isopulegol, 0.34±0.01 for citronellol, and 0.07±0.01 for citronellal

diisopropylacetal. These findings confirmed that our catalytic experiment is reproducible. To ensure that the reaction does not proceed without the catalyst, a blank experiment was also carried out under the same conditions but in the absence of Zr-beta-B. As expected, no conversion of citronellal was observed after 6 hours, confirming that the reaction is catalytic and does not occur spontaneously under the given reaction conditions.

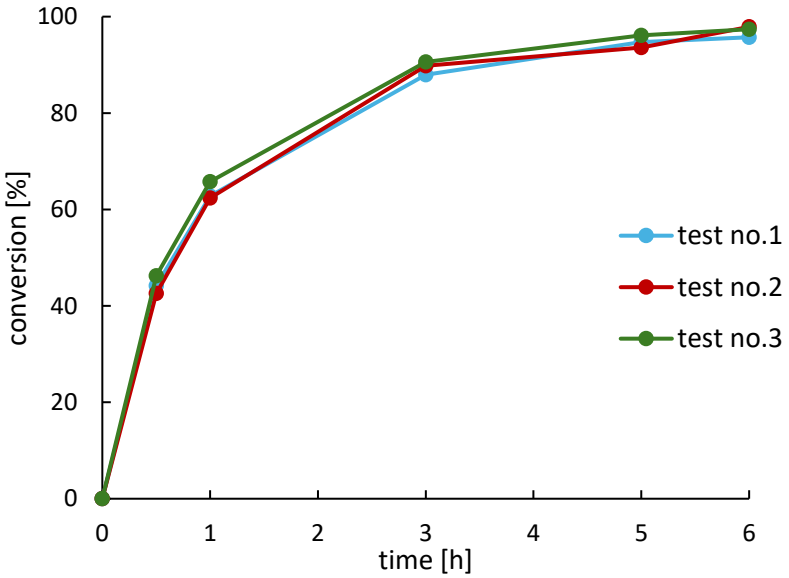

Figure 15: Conversion curves of the citronellal reaction with 2-propanol over 20 mg Zr-beta-B without base at 70 °C

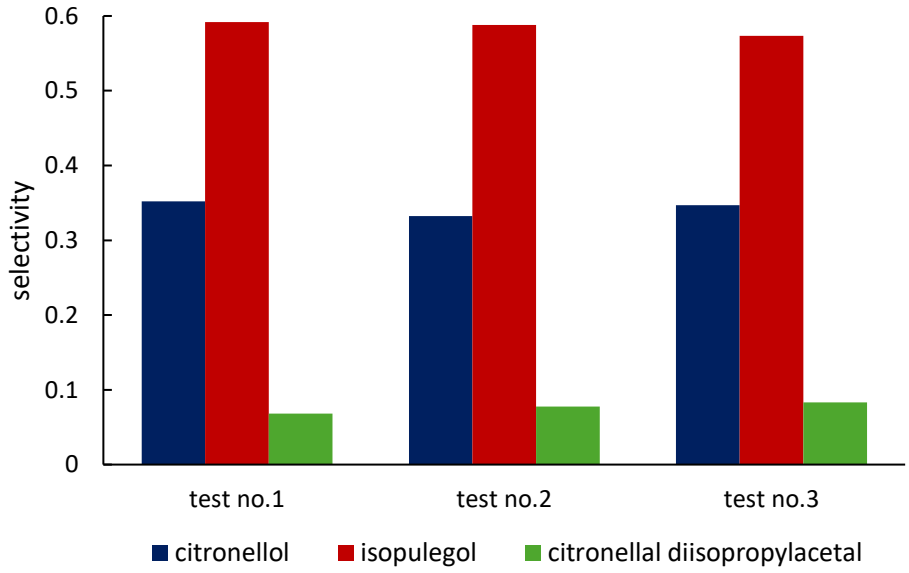

Figure 16: Comparison of the product distribution of base-free reaction after 6 hours over Zr-beta-B

5.2.1.2 The influence of pyridine-derived bases on citronellal reaction

In my bachelor thesis[3], it was shown that the introduction of an organic base to the reaction changes the reaction selectivity in favour of MPV reduction, and different bases provided this effect to varying extents. In those experiments, the base was added in a 1:10 molar ratio to citronellal and five bases were tested: hexamethylenetetramine, N,N-dimethylbenzylamine, 4-pyrrolidinopyridine, N-methylpiperidine, and pyridine. In the reaction with the first three bases, the selectivity was completely shifted toward citronellol, whereas in the presence of N-methylpiperidine and pyridine, a small amount of isopulegol was still observed. It was also concluded that the extent of this selectivity switch was independent of the base strength, and thus the driving parameters remained unclear.

Accordingly, in the present thesis, the reaction with pyridine-derived bases (pyridine and its derivate; 2,5-lutidine, 3,5-lutidine, 2,4,6-collidine and 2,6-ditert-butylpyridine (2,6-DTBP)) was systematically studied in this thesis to investigate how the steric hindrance of nitrogen atom in the base's structure and its overall size influence the course of the citronellal reaction over Zr-beta-B. The molecular size values used in this study, listed in Table 6, correspond to the smallest conformer of each molecule based on DFT modelling. According to reference[74], the values were obtained for pyridine (0.655 nm), 2,4,6-collidine (0.822 nm), and 2,6-DTBP (0.834 nm). However, no such calculated values were available for 2,5-lutidine and 3,5-lutidine. Therefore, their sizes were estimated based on structurally related aromatic compounds. The molecular size of 2,5-lutidine was approximated using *p*-xylene (0.671 nm), and 3,5-lutidine was approximated by *m*-xylene (0.735 nm) and 2,6-lutidine (0.738 nm).

The beta zeolite topology has channels with a diameter of around 0.67 nm[17,33], which corresponds to the size of small organic molecules such as pyridine (0.655 nm). This allows pyridine to freely diffuse into the pores and interact there with the internal Zr active sites. Similarly, 2,5-lutidine fits within the pore system, and its nitrogen remains sterically accessible for coordination. In the case of 3,5-lutidine, its estimated molecular diameter (~0.735 nm) slightly exceeds the size of the pores. However, due to the position of methyl groups in the meta positions, steric hindrance near the nitrogen atom is minimal. As a result, the molecule is still expected to access and interact with some internal acid sites. In contrast, 2,4,6-collidine and 2,6-DTBP are significantly bulkier, and their molecular diameter exceeds the pore size of the beta zeolite, which may limit its diffusion into the channels. While 2,4,6-collidine may still interact with the active centres on or near the external surface of the

catalyst due to its relatively accessible nitrogen atom, 2,6-DTBP is much more sterically hindered. Its large size (0.834 nm) and two bulky *tert*-butyl groups in the ortho positions limit nitrogen accessibility, making it sterically inaccessible for coordination, even on external Lewis acid sites.

Table 6: The molecular sizes of individual bases and their pKa values

	molecular size [nm]	**pK_a**
pyridine	0.655	5.14
2,5-lutidine	0.671	6.47
3,5-lutidine	0.735-0.738	6.15
2,4,6-collidine	0.822	7.48
2,6-DTBP	0.834	3.58

Figure 17 shows conversion curves over time for the MPV reduction of citronellal in the presence of the above bases, as well as in the absence of any base. The reaction without base achieved 97% conversion after 6 hours. In the presence of unsubstituted pyridine and 2,5-lutidine, the conversions were slightly lower but still reached over 80 % (specifically 83 %). This indicates that these smaller bases can diffuse to the pores with only minimal steric hindrance as predicted. To confirm that pyridine does not allow an alternative organocatalysed reaction pathway, a blank experiment was performed with pyridine in the absence of Zr-beta-B, which resulted in no conversion and no product formation. In contrast, the catalysed reaction with bulkier 2,6-DTBP resulted in reduced conversion to 71 %. The reduced conversion in this case may stem from weak interaction with external surface silanols or active sites. Interestingly, the reaction with 3,5-lutidine gave only 60% conversion, although this molecule is not significantly hindered around the nitrogen atom. This indicates that its overall molecular diameter, which slightly exceeds the pore size of the beta zeolite, limits its ability to diffuse efficiently into the pore system. The lowest conversion, 48 % after 6 hours, was observed with 2,4,6-collidine, which has a large molecular size so limited diffusion likely prevents effective interaction with the internal active sites. Overall, the results suggest that molecular size is a key factor affecting conversion. The larger the base molecule the more its diffusion into the zeolite channels is restricted. An exception is 2,6-DTBP, where the nitrogen atom is so sterically shielded that it likely cannot interact with the active sites at all, even on the external surface.

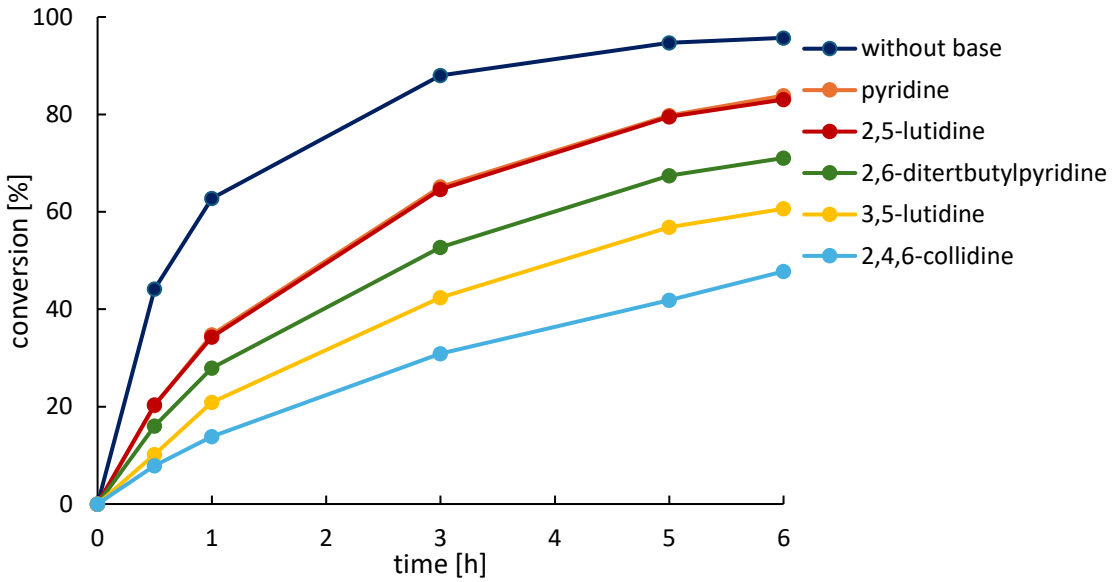

Figure 17: The conversion curves of base-free reaction and with addition of pyridine-derived bases over Zr-beta-B at 70 °C

The reaction progress may also be influenced by the pK_a values[75] (listed in Table 6) of the added bases. Pyridine has pK_a of 5.14 and gives high conversion. 2,5-lutidine (pK_a= 6.47) shows also high conversion (83 %), but 3,5-lutidine with relatively similar pK_a of 6.15 has lower conversion (60 %). 2,4,6-collidine has the highest pK_a of 7.48 and gives the lowest conversion among the substituted pyridines. On the other hand, 2,6-DTBP with the lowest pK_a (3.58) reached 71% conversion. These results show that there is no clear trend between pK_a and the rate of conversion.

The most important effect of the base is the selectivity switch favouring MPV reduction at the expense of carbonyl-ene cyclization. Accordingly, product yield (citronellol and isopulegol) was plotted against conversion (Figure 18). Notably, these selectivity curves clearly show that selectivity remains constant throughout the whole conversion range, which is evidenced by the linear trends observed in both graphs. This indicates citronellol and isopulegol are formed through parallel reaction pathways and the selectivity is independent of conversion. In addition to selectivity curves, the product distribution interpolated at 40% conversion in terms of selectivity was plotted in Figure 19, with detailed values provided in Table 7. For the base-free reaction over Zr-beta-B, isopulegol was the main product, and selectivity was 0.60 for isopulegol, 0.34 for citronellol, and 0.06 for citronellal diisopropylacetal. Conversely, the addition of the pyridine, 2,5-lutidine, 3,5-lutidine, and even 2,4,6-collidine caused the shift in selectivity toward citronellol. The only exception is 2,6-DTBP, which does not affect selectivity in comparison with the base-free reaction. This

shows that the coordination of the base to the Zr Lewis acid sites of the zeolite is essential for the selectivity switch. In the case of 2,6-DTBP, the bulky *tert*-butyl groups sterically hinder the nitrogen atom, preventing interaction with the active sites. Reactions with smaller bases such as pyridine and 2,5-lutidine exhibit similar selectivity, resulting in 0.70 for citronellol. However, 3,5-lutidine shows decrease in selectivity to 0.60. This suggests that even substituents located further from the nitrogen atom can affect the reaction. Overall, the reaction is mainly influenced by two factors. One is the ability of the base to coordinate with the Lewis acid site, which depends on its accessibility. The other is the ability of the base to diffuse into the microporous structure of the zeolite.

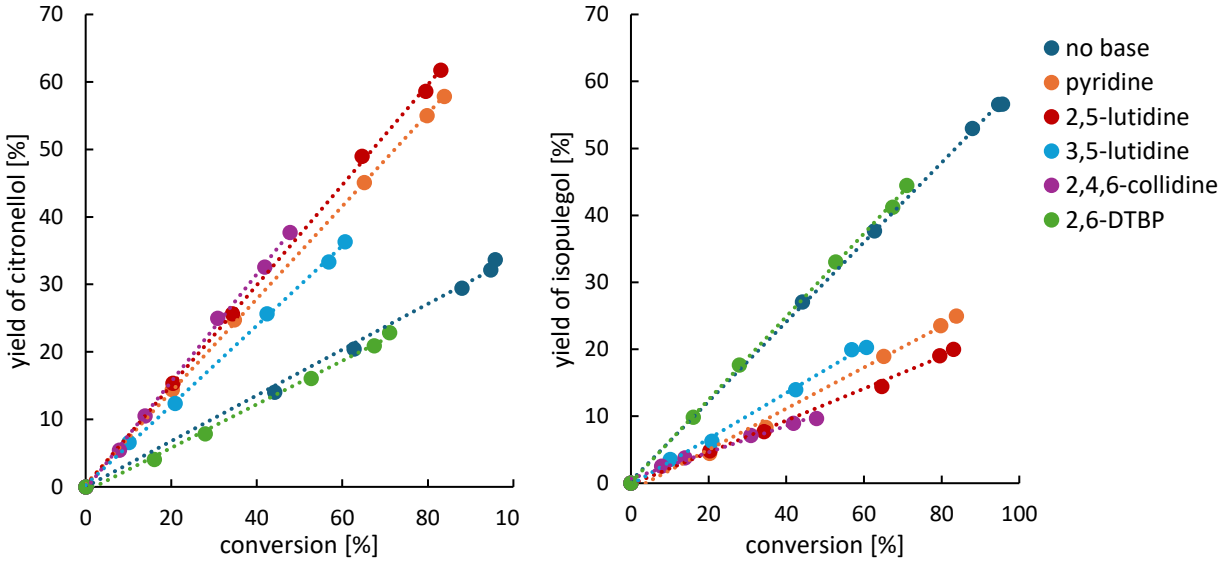

Figure 18: Dependence of yields (left citronellol, right isopulegol) on conversion for reaction with and without substituted pyridines at 70 °C over Zr-beta-B

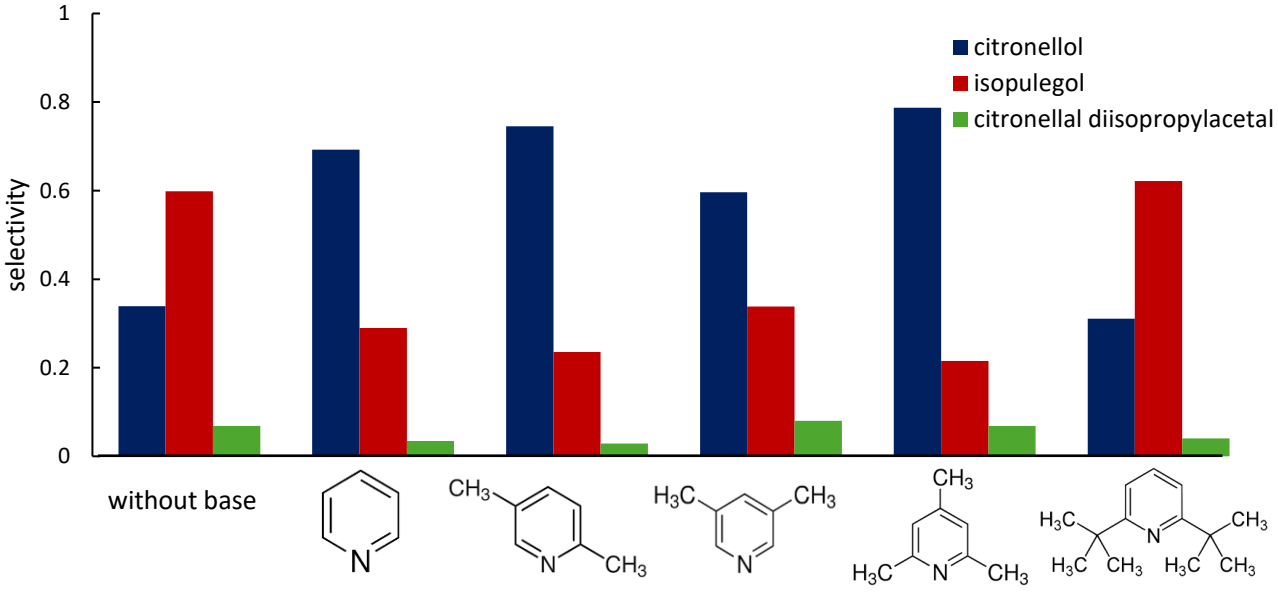

Figure 19: Distribution of products at 40% conversion for reactions without and with substituted pyridines over Zr-beta-B at 70 °C

Table 7: Summary of conversion and selectivity values of the base-free reaction and with the addition of pyridine-derived bases over Zr-beta-B at 70°C. Selectivity values were obtained from the slopes of product-specific selectivity curves. As a result, their sum does not necessarily equal 100 %, which is within the experimental error

type of the experiment		conversion [%]	selectivity		
			citronellol	isopulegol	citronellal diisopropylacetal
reaction without base	test no.1	95.7	0.35	0.59	0.07
	test no.2	97.9	0.33	0.59	0.08
	test no.3	97.4	0.35	0.57	0.08
reaction with base	pyridine	83.9	0.69	0.30	0.03
	2,5-lutidine	83.0	0.74	0.24	0.03
	3,5-lutidine	60.6	0.60	0.33	0.08
	2,4,6-collidine	47.8	0.79	0.18	0.07
	2,6-DTBP	72.0	0.32	0.62	0.04

Turnover frequencies (TOF) calculated for individual product formation could further distinguish the effects of base structure on the catalytic activity. Table 8 summarizes the TOF values for MPV reduction of citronellal in the presence of various bases. In the absence of any base, the TOF values are 1.6 s^{-1} for citronellal consumption, 0.55 s^{-1} for citronellol formation, and 0.96 s^{-1} for formation of isopulegol. The most evident trend is an increase in TOF for citronellol formation upon the addition of small bases (pyridine and 2,5-lutidine), thus easily diffusing in the micropores and possess sterically accessible nitrogen atoms available for coordination to the active sites. In the case of pyridine, the TOF increases to 0.72 s^{-1} and to 0.76 s^{-1} for 2,5-lutidine, indicating that these bases enhance selectivity of MPV reduction favouring citronellol. In contrast, the use of bulkier bases, especially 2,6-DTBP, leads to lower TOF values for citronellol formation, with the lowest value observed (0.20 s^{-1}). This reflects that their growing size and steric hindrance limit access to internal active sites and diffusion. Nevertheless, an increase in citronellol formation may still occur, but it is less apparent due to the significantly reduced overall reaction rate. In parallel, TOF values for isopulegol formation decrease for all tested bases, confirming that base addition consistently suppresses the competing carbonyl-ene cyclization, except for 2,6-DTBP, which does not significantly alter the product distribution.

Table 8: TOFs of citronellal MPV reduction with pyridine-derived bases over Zr-beta-B

		TOF [s^{-1}]		
		citronellal	**citronellol**	**isopulegol**
reaction without base		1.6	0.55	0.96
reaction with base	pyridine	0.86	0.72	0.21
	2,5-lutidine	0.85	0.76	0.19
	3,5-lutidine	0.52	0.28	0.16
	2,4,6-collidine	0.34	0.27	0.094
	2,6-DTBP	0.69	0.20	0.44

A comparison of the yield curves (Figure 20) for reactions with and without pyridine further shows that the addition of the base accelerates the formation of citronellol, indicating that the base influences the intrinsic reaction mechanism. These findings rule out the possibility of selective site poisoning mechanism, in which the base would be expected to block specific active sites and reduce the overall reaction rate. These results suggest that pyridine does not deactivate the active sites but rather modifies them, enabling faster formation of the MPV product.

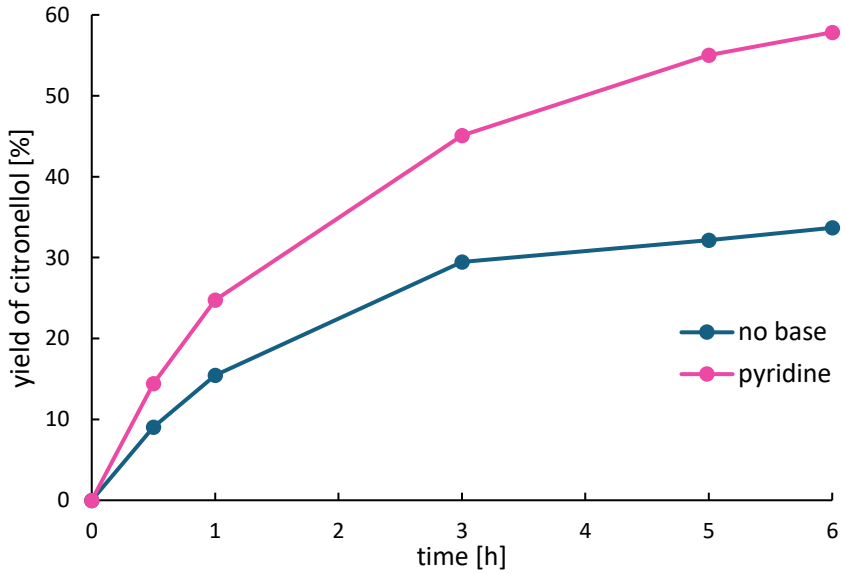

Figure 20: Citronellol yield curves without base and with pyridine over Zr-beta-B at 70 °C

5.2.2 Characterization of Lewis acid sites in Zr-beta-A by FTIR spectroscopy using acetone and pyridine as probe molecule

In order to prove the site modification mechanism, we ttamted to prove carbonyl compounds can be adsorbed on Zr sites even after saturation with the base. To simulate conditions relevant to our reaction system, a comparative FTIR experiment was designed. In

the first step, acetone was adsorbed on activated Zr-beta-A, and the corresponding FTIR spectrum was recorded. In the second step, pyridine was introduced to the reactivated catalyst before acetone, allowing the catalyst to reach pyridine adsorption equilibrium, after which acetone (its carbonyl group acting as a model for citronellal in our reaction system) was introduced.

The first subtracted FTIR spectrum (Figure 21) shows the vibrational features of acetone on activated Zr-beta-A. A strong band appears in the carbonyl stretching region (1690-1720 cm^{-1}), indicating the interaction of acetone with Lewis acid sites. Specifically, three distinct peaks are observed in 1720, 1709, and 1698 cm^{-1}. The band at 1720 cm^{-1} corresponds to physisorbed acetone molecules, while the band at 1709 cm^{-1} indicates coordination to "closed" Lewis acid sites[71]. In contrast, the band at 1698 cm^{-1} was attributed to acetone adsorbed to stronger, "open" Lewis acid sites[70]. Additionally, the band at 1743 cm^{-1} corresponds to acetone in the gas phase[76].

The second FTIR spectrum (Figure 22) shows the adsorption of pyridine on the reactivated Zr-beta-A zeolite. A sharp and intense band at 1608 cm^{-1} is observed, assigned to the pyridine coordinated to Lewis acid sites. Two additional bands appear at 1490 and 1448 cm^{-1}. The 1490 cm^{-1} band is associated to pyridine interacting with both Brønsted and Lewis acid sites, while the 1448 cm^{-1} band is linked to δ(CH) deformation of coordinated pyridine, providing further evidence of their presence. Importantly, the spectrum lacks a band near 1545 cm^{-1}, which would indicate protonated pyridine (PyH^+) at Brønsted acid sites[77]. This absence, i.a., confirms the purely Lewis acidic nature of the Zr-beta-A sample.

The third FTIR spectrum (Figure 23) represents a sample of Zr-beta-A that was first pre-treated with pyridine before acetone was introduced. The same characteristic bands (1720, 1709, and 1698 cm^{-1}) for acetone adsorption are observed as in the first spectrum, confirming that acetone still interacts with Lewis acid sites. However, the reduced intensity of the bands compared to the untreated sample suggest that some of the sites have been partially blocked by the prior pyridine adsorption. Overall, the presence of these bands shows that acetone can still coordinate to Lewis acid sites, even in the presence of a base like pyridine.

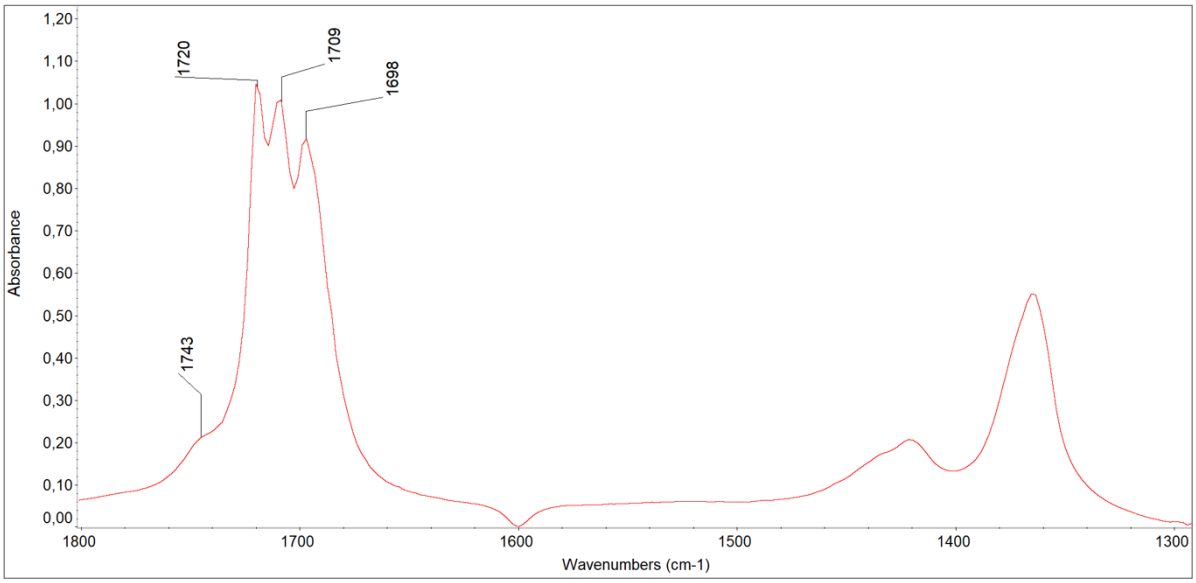

Figure 21: FTIR substracted spectrum of acetone adsorbed on Zr-beta-A

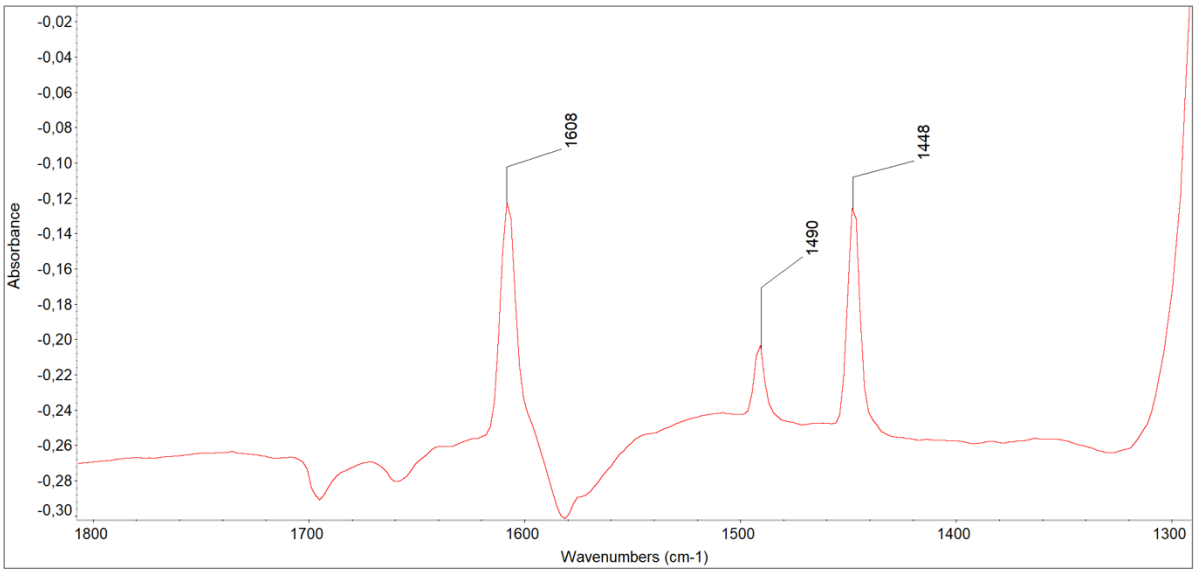

Figure 22: FTIR substracted spectrum of Zr-beta-A after pyridine adsorption

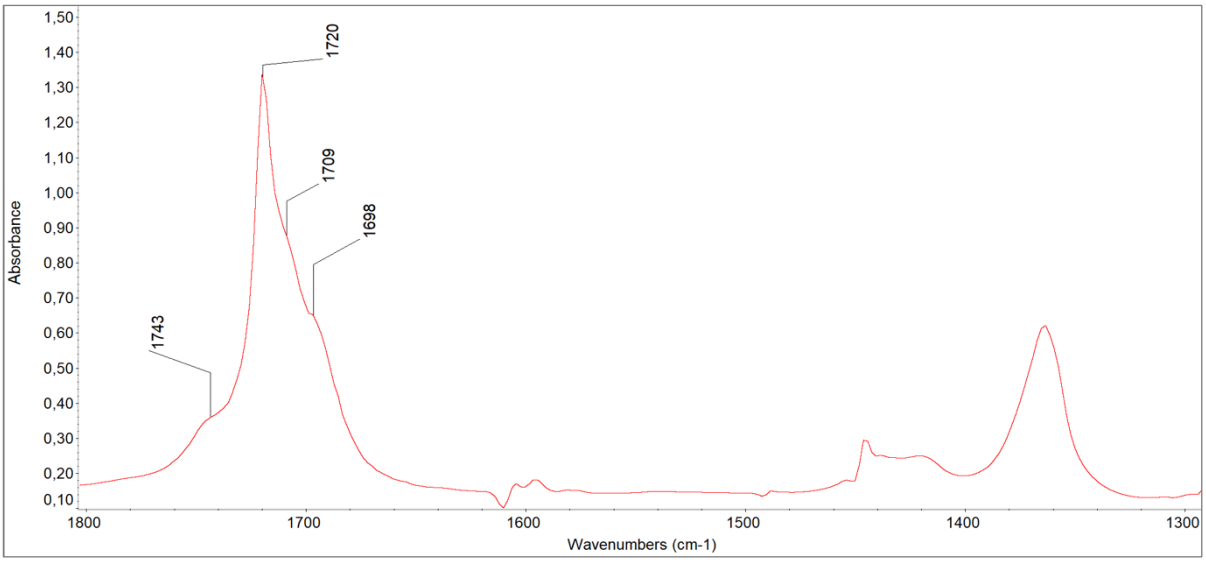

Figure 23: FTIR substracted spectrum of acetone adsorbed on Zr-beta-A after pyridine pre-adsorption

5.2.3 Kinetic study

The above observations with substituted pyridines suggested the base likely modifies the Zr active sites and thus changes the intrinsic reaction mechanism. A change in reaction mechanism should manifest itself in changing (apparent) activation energy. Therefore, a kinetic study was conducted to determine the apparent activation energies of individual reaction pathways to gain a deeper understanding of the reaction mechanism and to understand how different bases (pyridine and N-methylpiperidine) at different temperatures affect the reaction rate and selectivity of the reaction over Zr-beta-A and Sn-beta. The choice of bases followed findings from my bachelor's thesis.[3] Pyridine was chosen as a "standard" nitrogen-containing base, i.e., widely used in IR spectroscopy due to its characteristic absorption bands. In contrast, N-methylpiperidine was selected as a small aliphatic base, which provided an outstanding selectivity toward citronellol in our system.

Firstly, to confirm that the reaction is not limited by external diffusion (not limited by mass transfer of reactants to the catalyst particles), the reaction with citronellal over Zr-beta-C was tested at three different stirring speeds: 100, 450 and 600 rpm. If mass transfer was a significant factor, increasing the stirring speed would lead to noticeably higher reaction rates. However, Figure 24 and Figure 25 showed that both the conversions and distribution of the products remained nearly identical across all stirring speeds, with differences of only about 3 %. These small variations are within the expected experimental range and are consistent with the reproducibility demonstrated earlier. Given this, it can be concluded that the reaction is not limited by external diffusion.

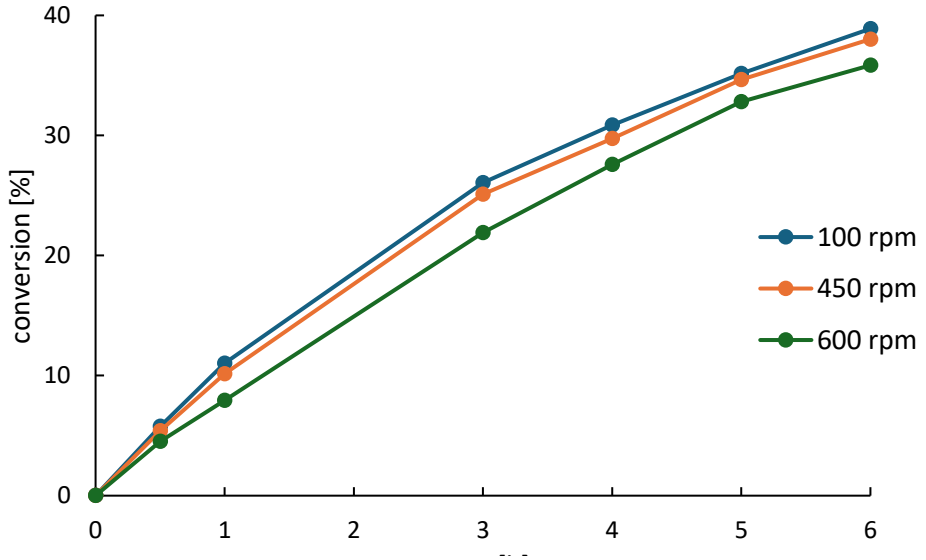

Figure 24: Conversion curves of the citronellal base-free reaction at different rpm over Zr-beta-C at 70 °C

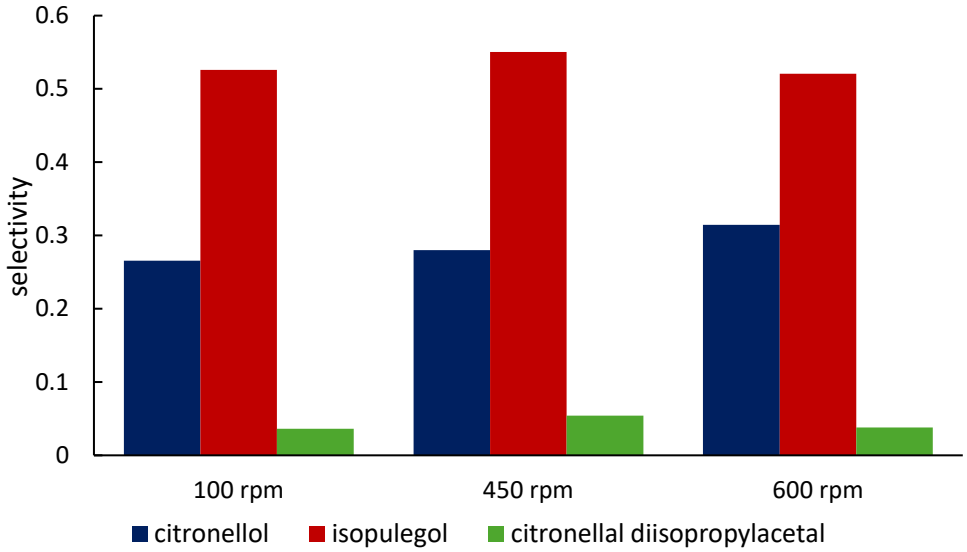

Figure 25: Distribution of the products at 35% conversion of the citronellal reaction at different rpm over Zr-beta-C at 70 °C

To determine the reaction order, the integral method was applied by fitting the experimentally measured concentration over time to theoretically integrated rate equations corresponding to orders of 0, 0.5, 1, 1.5, and 2. This analysis was conducted for all three systems. As an example, Figure 26 shows the fitted plots for the base-free reaction and Figure 27 with pyridine at 70 °C. In both cases, the best linear correlation was observed for the second-order model ($R^2 = 0.9919$ in the reaction without base, $R^2 = 0.9761$ for presence of the pyridine), indicating that the rate of formation follows second-order kinetics with respect to citronellal.

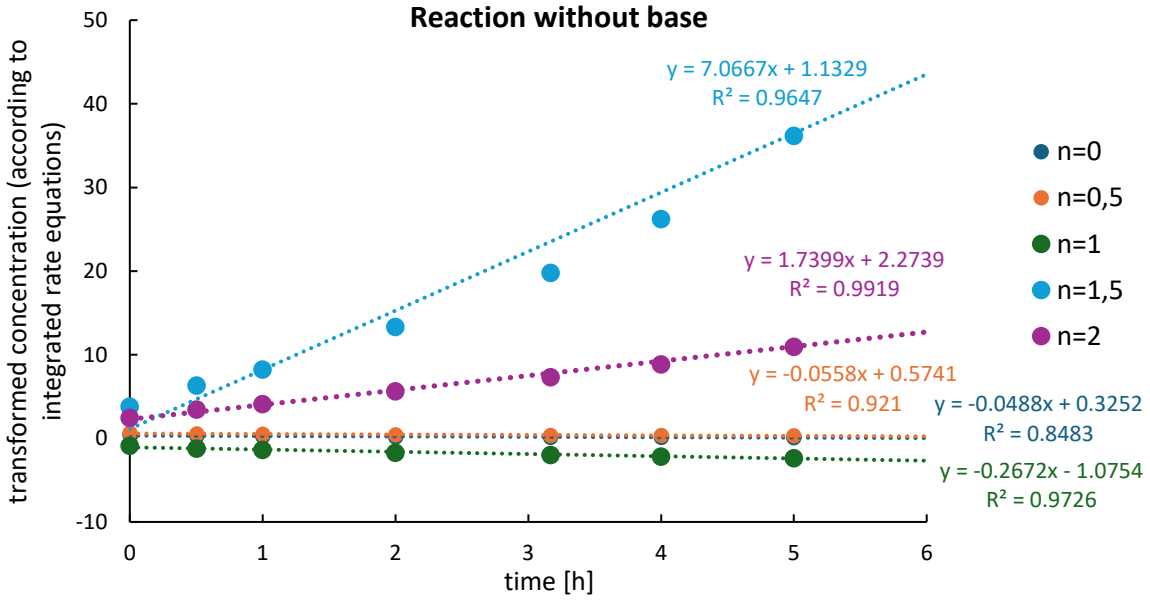

Figure 26: Example of determination of reaction order by integral method for base-free reaction over Zr-beta-A at 70 °C

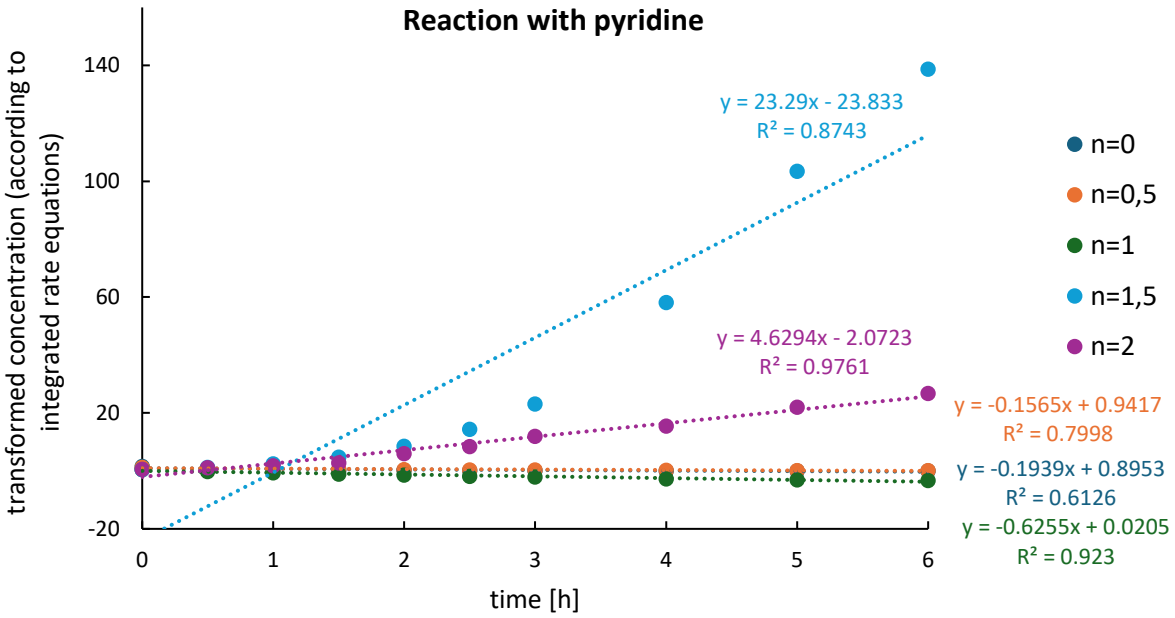

Figure 27: Example of determination of reaction order by integral method for reaction with pyridine over Zr-beta-A at 70 °C

To determine the apparent activation energies, we need to choose a kinetic model for each reaction pathway, meaning the formation of citronellol and isopulegol. The formation for citronellal diisopropylacetal was neglected in this activation energy calculation because its yield in most of the reactions with bases was below 5 %. For the MPV reduction over Lewis acid zeolites, there exists already a kinetic model developed by Y. Romanov et. al.[78], for cyclohexanone substrate, which is described by the following rate equation:

$$\frac{r}{[L]} = \frac{K_{\text{ads}} k_{\text{app}} a_{\text{C}}}{a_{\text{P}} + K_{\text{ads}} a_{\text{C}}} \qquad (7)$$

Here, K_{ads} represents the equilibrium constant for the adsorption of the carbonyl substrate (in our case citronellal), k_{app} is the apparent rate constant, a_i are the activities of 2-propanol (a_{P}) and substrate (a_{C}) in solution, and $[L]$ is the concentration of active sites in the catalyst. The activities of each species are calculated using the following equation:

$$a_i = \gamma_i \left(\frac{c_i}{c_0}\right) \qquad (8)$$

where c_i is the concentration of molecules i in solution, c_0 is the standard state concentration equal to the concentration of the pure component, and γ_i is the activity coefficient of species i in solution, which accounts for non-ideal behaviour in solution. Since all our experiments were conducted on the same catalyst, the activity coefficient in the activity term was neglected due to the assumption of ideal behaviour, and only the relative concentrations were used. The final form of the rate expression used initially in our analysis is therefore:

$$\frac{r_{\text{citronellol}}}{[L]} = \frac{K_1 \cdot k_2 \cdot c_{\text{citronellal}}}{13.08 + K_1 \cdot c_{\text{citronellal}}} \qquad (9)$$

where 13.08 is the concentration of 2-propanol in the reaction mixture in $\mathrm{mol} \cdot \mathrm{l}^{-1}$, which is the same in all reactions. Since Roman-Leshkov's et. al.[78] model is designated for the MPV reduction pathway, it was not suitable for describing isopulegol formation. As this reaction proceeds by a different mechanism and occurs on different active sites, a pseudo-second-order kinetic model was used instead, based on the results of the reaction order estimation by the integral method.

$$\frac{r_{\mathrm{isopulegol}}}{[L]} = k_3 \cdot (c_{\mathrm{citronellal}})^2 \qquad (10)$$

After optimizing the rate constants using the ERA program, it was found that the original three-parameter model produced unreliable values (Table 9) for the MPV reduction rate constant k_2 (unlimited confidence interval), as shown in Figure 28 where the fitted data deviate from the experimental points. Various attempts were made to improve the fit by fixing one of the parameters and freeing others, but these approaches were also unsuccessful. As a result, the model was simplified to a two-parameter model (eq. 11 for citronellol formation and eq. 10 for isopulegol formation), which assumes that only the adsorption of 2-propanol (and not the aldehyde) is in equilibrium, which ultimately proved to be a reasonable assumption. This simplified model was then used for the analysis of the apparent activation energy. See sample fits in Figure 31.

$$\frac{r_{\mathrm{citronellol}}}{[L]} = \frac{k_1 \cdot c_{\mathrm{citronellal}}}{13.08 + k_1 \cdot c_{\mathrm{citronellal}}} \qquad (11)$$

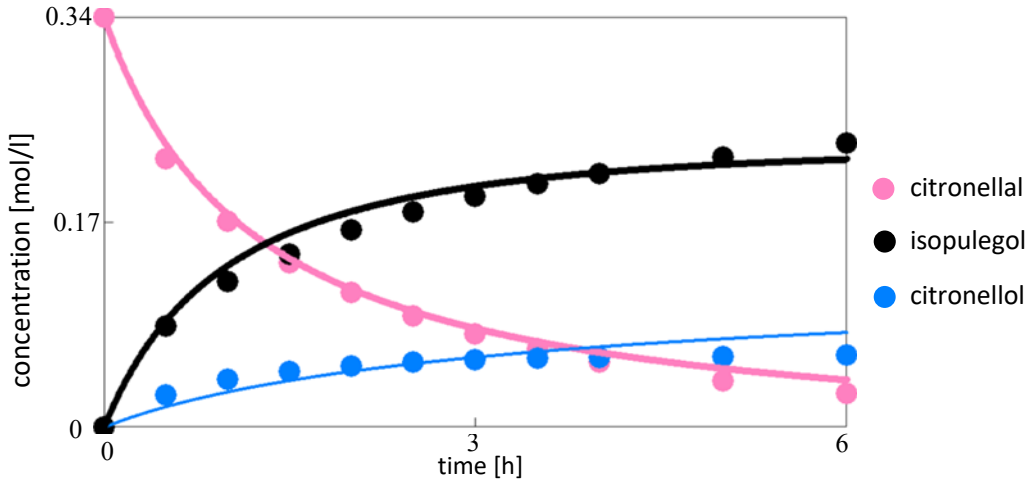

Figure 28: Fit of experimental data for the citronellal MPV reduction with pyridine at 60 °C over Zr-beta-A. The concentration profiles are shown with the lines represent the fitted curves obtained using the kinetic models described by eqs. 9 and 10.

Table 9: Calculated rate constants k_1, k_2, and k_3 (labelled as 1, 2, and 3) from the fit along with their confidence intervals defined by the lower and upper F-limits (low F-limit and high F-limit)

	value	low F-limit	high F-limit
1	0.00082	0.0000	31.6122
2	1928.04	0.06900	14978640397
3	1.48868	1.39246	1.58919

5.2.3.1 Kinetic study over Zr-beta-A

The kinetic study of MPV reduction of citronellal over Zr-beta-A was conducted at five temperatures (40, 50, 60, 70, and 80 °C) in the absence and presence of two bases (pyridine and N-methylpiperidine). The corresponding conversion curves are plotted in Figure 29. It is important to note that the base-free reaction was performed using only 40 mg of catalyst, as the use of 200 mg led to a fast conversion, reaching 100 % after 1 hour, where no meaningful kinetic trends could be observed. As expected, an increase in temperature led to a higher conversion rate in all cases. The reaction with pyridine reached full conversion within 6 hours at 70 and 80 °C. In contrast, the presence of N-methylpiperidine significantly slowed down the reaction. Even at 80 °C, the conversion reached only 52 % after 6 hours.

Subsequent data analysis involved plotting the product distribution interpolated at 20% conversion. Figure 30 (graphs A-C) showed that selectivity remained constant across different temperatures for all reactions. It is further evident that in the absence of a base, isopulegol was the main product, with a selectivity of 0.70 ± 0.05 across the entire temperature range. However, the addition of bases influenced the reaction mechanism, altering the selectivity in favour of citronellol, which became the main product in both base-modified systems, with selectivities of 0.95 ± 0.03 for N-methylpiperidine and 0.90 ± 0.03 for reaction with pyridine. In reactions with these bases, the selectivity of isopulegol did not exceed 0.10, and citronellal diisopropylacetal was not detected at all. Further, citronellol yield, the main and desired product, was plotted (Figure 30, graphs D-F) against overall citronellal conversion to construct selectivity curves.

Table 10 presents TOF values for the reaction of citronellal over Zr-beta-A, comparing 3 different reaction systems: without any base, with N-methylpiperidine, and with pyridine, across temperatures from 40 to 80 °C. A clear trend is observed, where the addition of bases significantly influences both the product distribution and overall reaction rates. Notably, the presence of pyridine leads to the acceleration of citronellol formation as observed before over the Zr-beta-B. For example, at 40 °C, the reaction in the presence of pyridine has a TOF of 0.40 s^{-1} for citronellol formation, compared to only 0.14 s^{-1} in the base-free system. The TOF values for citronellol formation remain consistently higher than those for the formation of isopulegol across the entire temperature range and the addition of both bases, indicating a shift in selectivity toward citronellol upon base addition. Overall,

both bases promote the formation of citronellol. These findings suggest that the presence and specific nature of the base play a key role in modifying the reaction mechanism.

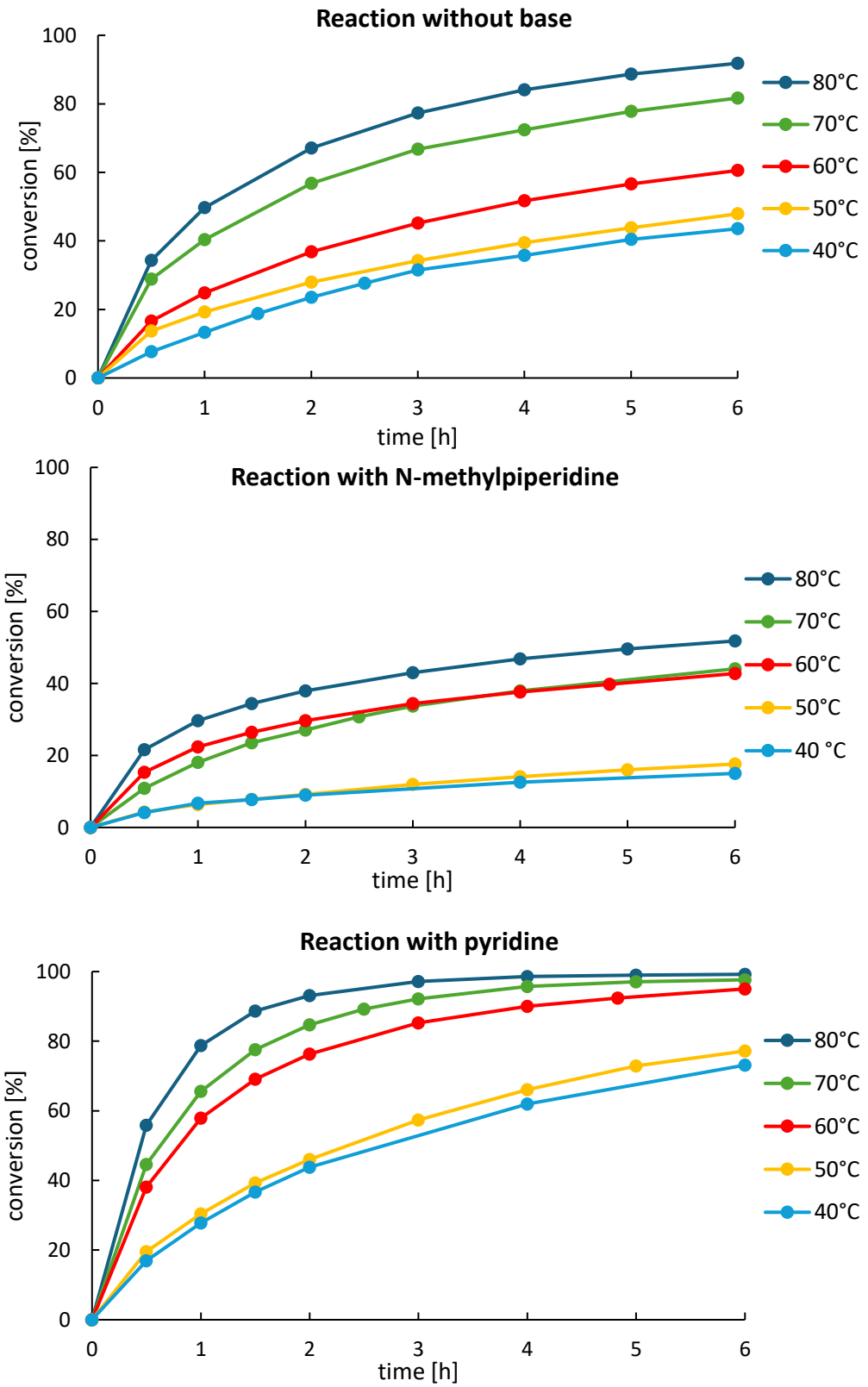

Figure 29: Conversion curves of the citronellal reaction without base over 40 mg Zr-beta-A, with N-methylpiperidine and pyridine over 200 mg of the catalyst at different temperatures (base / citronellal is 1:10)

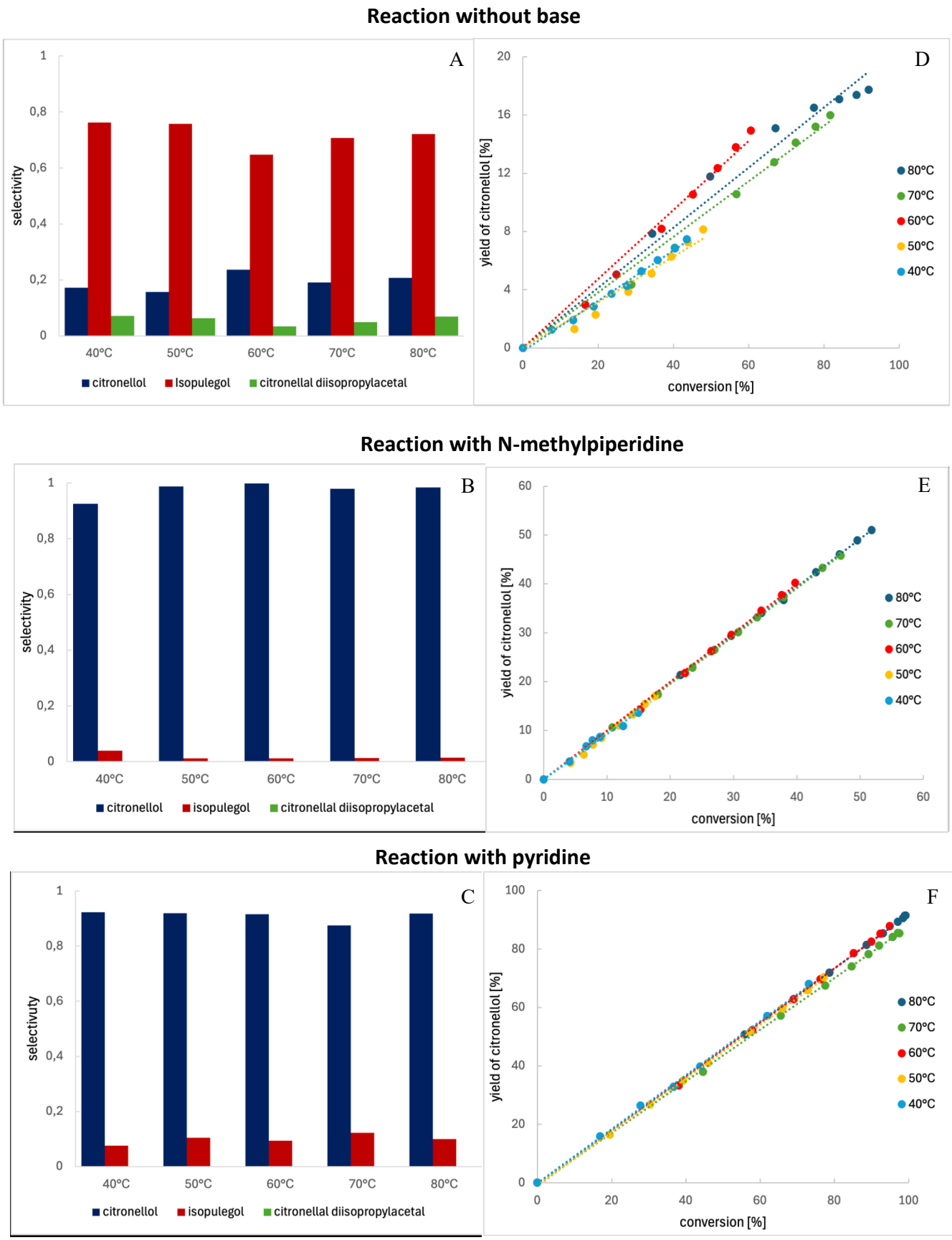

Figure 30: Distribution of the products at 20% conversion (graphs A-C) and citronellol selectivity curves over conversion (graphs D-F) for base-free reaction and with bases (N-methylpiperidine, pyridine) over Zr-beta-A at different temperatures

Table 10: TOF values for citronellal reaction over Zr-beta-A without base, with pyridine and N-methylpiperidine at different temperatures

		TOF values [s^{-1}]		
		citronellal	**citronellol**	**isopulegol**
Zr-beta-A without base	40 °C	1.0	0.14	0.71
	50 °C	1.5	0.15	1.2
	60 °C	1.9	0.17	1.3
	70 °C	3.1	0.52	2.2
	80 °C	3.8	0.89	2.6
Zr-beta-A with N-methylpiperidine	40 °C	$9.7 \cdot 10^{-2}$	$7.7 \cdot 10^{-2}$	$1.1 \cdot 10^{-2}$
	50 °C	0.10	$7.7 \cdot 10^{-2}$	$1.1 \cdot 10^{-2}$
	60 °C	0.28	0.26	$1.3 \cdot 10^{-2}$
	70 °C	0.34	0.33	$1.4 \cdot 10^{-2}$
	80 °C	0.45	0.45	$1.5 \cdot 10^{-2}$
Zr-beta-A with pyridine	40 °C	0.42	0.40	$3.6 \cdot 10^{-2}$
	50 °C	0.46	0.41	$5.5 \cdot 10^{-2}$
	60 °C	0.88	0.79	$8.3 \cdot 10^{-2}$
	70 °C	0.99	0.87	0.12
	80 °C	1.2	1.1	0.12

The experimental data obtained from the catalytic reactions were processed using the ERA software, where the rate constants were estimated by fitting the measured concentration profiles to the proposed kinetic models. The kinetic rate constants were determined using the rate equations for citronellol (eq. 11) and isopulegol (eq. 10) and are summarized in Table 11. The table also contains the corresponding confidence intervals, defined by the lower (low F-limit) and upper (high F-limit) bounds, which reflect the statistical reliability of the fitted values. As an illustration, Figure 31 shows the experimental data fitted using a two-parameter kinetic model for base-free reaction, as well as for reactions conducted in the presence of bases at 60 °C.

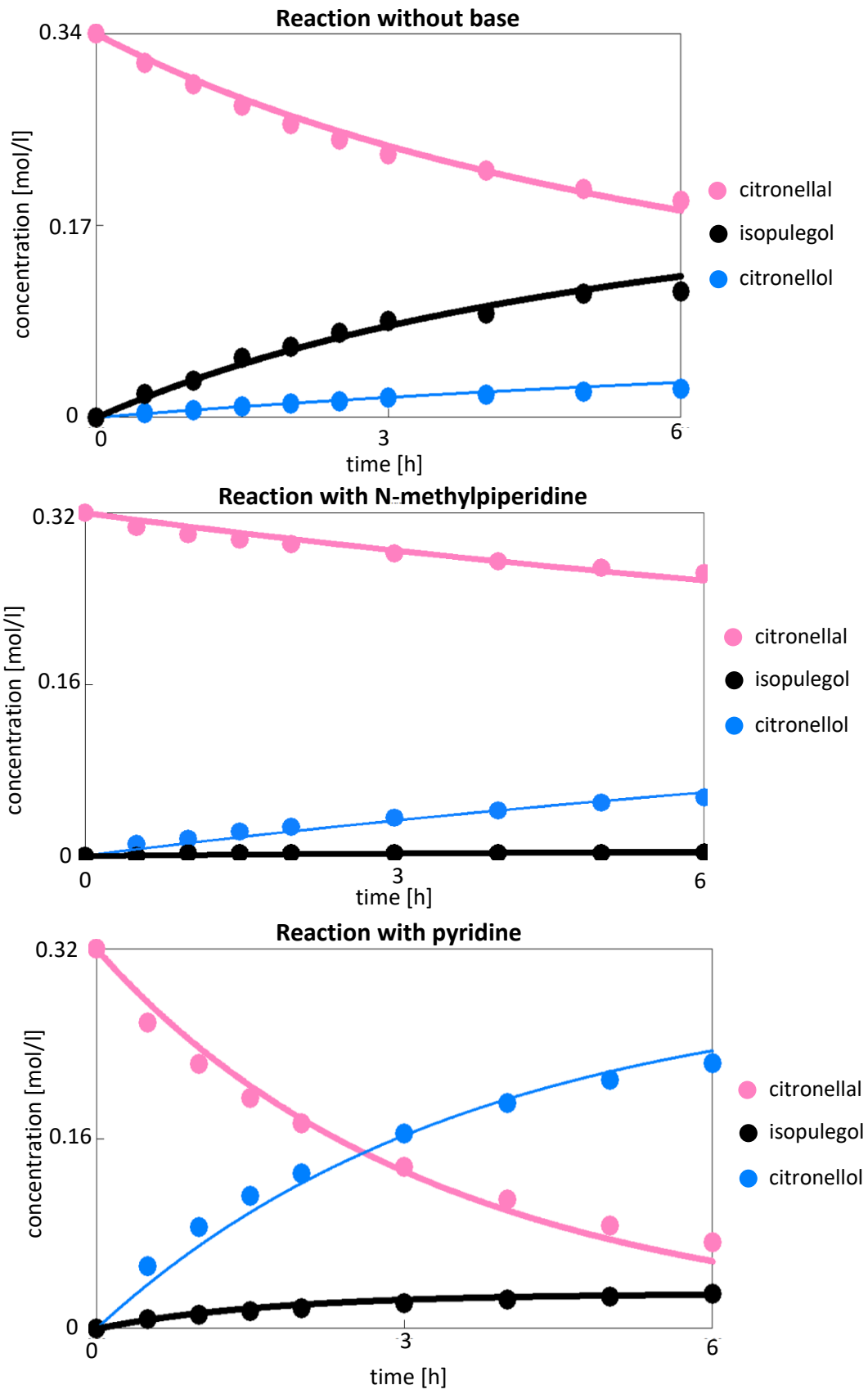

Figure 31: Concentration of reaction components dependance on time for citronellal reduction at 60 °C over Zr-beta-A

Table 11: Calculated rate constants, low and high F-limits for kinetic study over Zr-beta-A

			rate constant	low F-limit	high F-limit
Zr-beta-A without base	40 °C	citronellol	0.875	0.815	1.13
		isopulegol	2.40	2.33	2.47
	50 °C	citronellol	1.54	1.04	2.03
		isopulegol	3.17	3.02	3.33
	60 °C	citronellol	3.26	2.86	3.75
		isopulegol	3.71	3.56	3.85
	70 °C	citronellol	5.35	4.62	6.20
		isopulegol	5.35	5.15	5.60
	80 °C	citronellol	8.05	7.60	9.00
		isopulegol	7.45	7.15	7.70
Zr-beta-A with N-methylpiperidine	40 °C	citronellol	0.318	0.304	0.346
		isopulegol	0.089	0.000	0.127
	50 °C	citronellol	0.346	0.341	0.358
		isopulegol	0.100	0.000	0.165
	60 °C	citronellol	0.693	0.684	0.716
		isopulegol	0.139	0.000	0.251
	70 °C	citronellol	0.734	0.693	0.776
		isopulegol	0.144	0.000	0.206
	80 °C	citronellol	0.889	0.827	0.956
		isopulegol	0.198	-0.221	0.332
Zr-beta-A with pyridine	40 °C	citronellol	3.50	3.24	3.76
		isopulegol	0.330	0.233	0.408
	50 °C	citronellol	5.56	5.55	5.83
		isopulegol	0.412	0.353	0.466
	60 °C	citronellol	9.51	8.58	10.4
		isopulegol	0.641	0.544	0.733
	70 °C	citronellol	13.7	12.4	14.7
		isopulegol	0.891	0.825	0.956
	80 °C	citronellol	24.7	23.8	27.3
		isopulegol	0.959	0.896	1.02

Subsequently, Arrhenius plots (Figure 32) were constructed by plotting $\ln(k_i)$ against $1/T$, where k_i denotes the rate constant derived from the kinetic model for the formation of either citronellol or isopulegol. The apparent activation energies for the formation of both products were determined from the slopes of the corresponding linear fits. All the calculated values are in Table 12.

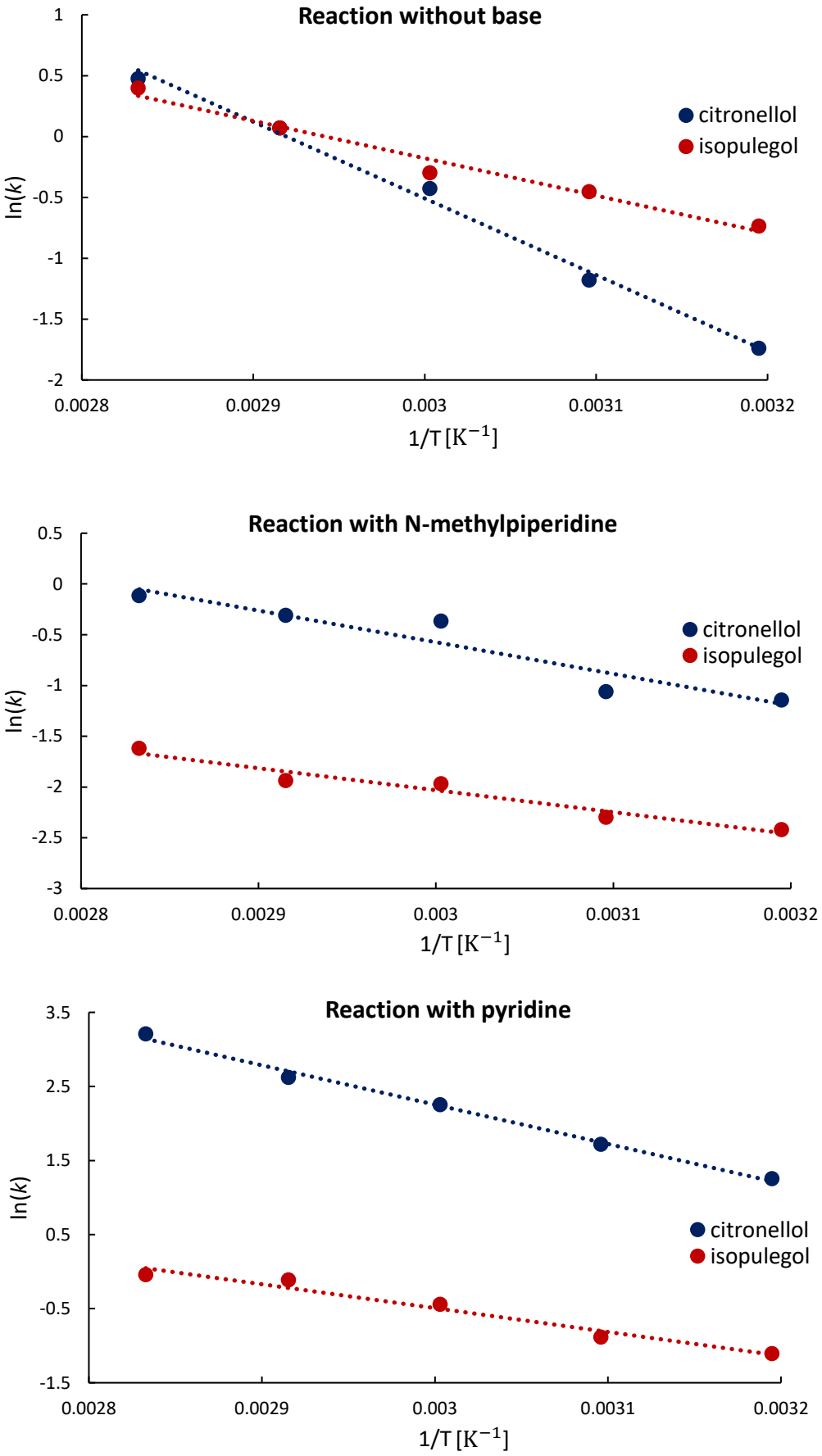

Figure 32: Arrhenius plots for base-free reaction and with addition of bases over Zr-beta-A

Table 12: Comparison of calculated apparent activation energies for citronellal reaction over Zr-beta-A

	apparent activation energy [kJ · mol^{-1}]	
	citronellol	**isopulegol**
no base	52	26
with N-methylpiperidine	26	18
with pyridine	44	27

In summary, the apparent activation energies for the formation of both products were estimated under base-free and base-modified conditions to assess the influence of organic bases on the reaction pathway. As expected, if the reaction mechanism changes upon the addition of a base, a corresponding shift in apparent activation energy should be observed. The calculated values show that in the presence of N-methylpiperidine, both activation energies fall below 30 kJ · mol^{-1} (26 kJ · mol^{-1} for citronellol formation and 18 kJ · mol^{-1} for isopulegol formation), which suggests that the system operates under (internal) diffusion-controlled conditions. In contrast, the addition of pyridine affects the mechanism of formation of citronellol, where the activation energy decreases from 52 to 44 kJ · mol^{-1}, while the activation energy for isopulegol formation remains nearly unchanged (also falls in the diffusion-controlled regime). These findings support the hypothesis that different bases change the intrinsic reaction mechanism of the MPV reduction by modifying the active sites. At the same time, isopulegol formation may also be suppressed by slowing down its diffusion out of the active sites or steric hindering of its formation in the confined space of the micropores.

5.2.3.2 Kinetic study over Sn-beta

For the kinetic study conducted using Sn-beta as the catalyst, four reaction temperatures were selected: 50, 60, 70 and 80 °C. The conversion curves (Figure 33) revealed that the addition of bases has a significant effect on the overall reaction rate. Specifically, the presence of pyridine decreased the reaction rate. In contrast, the addition of N-methylpiperidine led to a much stronger decrease in reaction rate. At 80 °C, the conversion after 6 hours was only 9 %, indicating a strong inhibition effect.

For further analysis, isopulegol yield was plotted against citronellal conversion (Figure 34, graphs D-F) to complement the kinetic study. The dependence of isopulegol yield on conversion followed a similar trend to that observed in reactions catalysed by Zr-beta-A, confirming that reactions proceed via parallel pathways. Additionally, product distribution (Figure 34, graphs A-C) was constructed, showing that isopulegol was the dominant product in the base-free reaction, similar to the Zr-beta system. Upon addition of both bases, a selectivity switch was also observed with Sn-beta, although to a lesser extent. In the reaction with pyridine, the ratio of isopulegol to citronellol formation was approximately 50:50 %. In the reaction with N-

methylpiperidine, the selectivity shifted more clearly towards citronellol, reaching 0.80±0.03 across temperature range. Nevertheless, 0.16±0.03 of isopulegol was still formed, which is notably higher than in the reaction catalysed by Zr-beta-A, where isopulegol formation was almost completely suppressed under the same conditions.

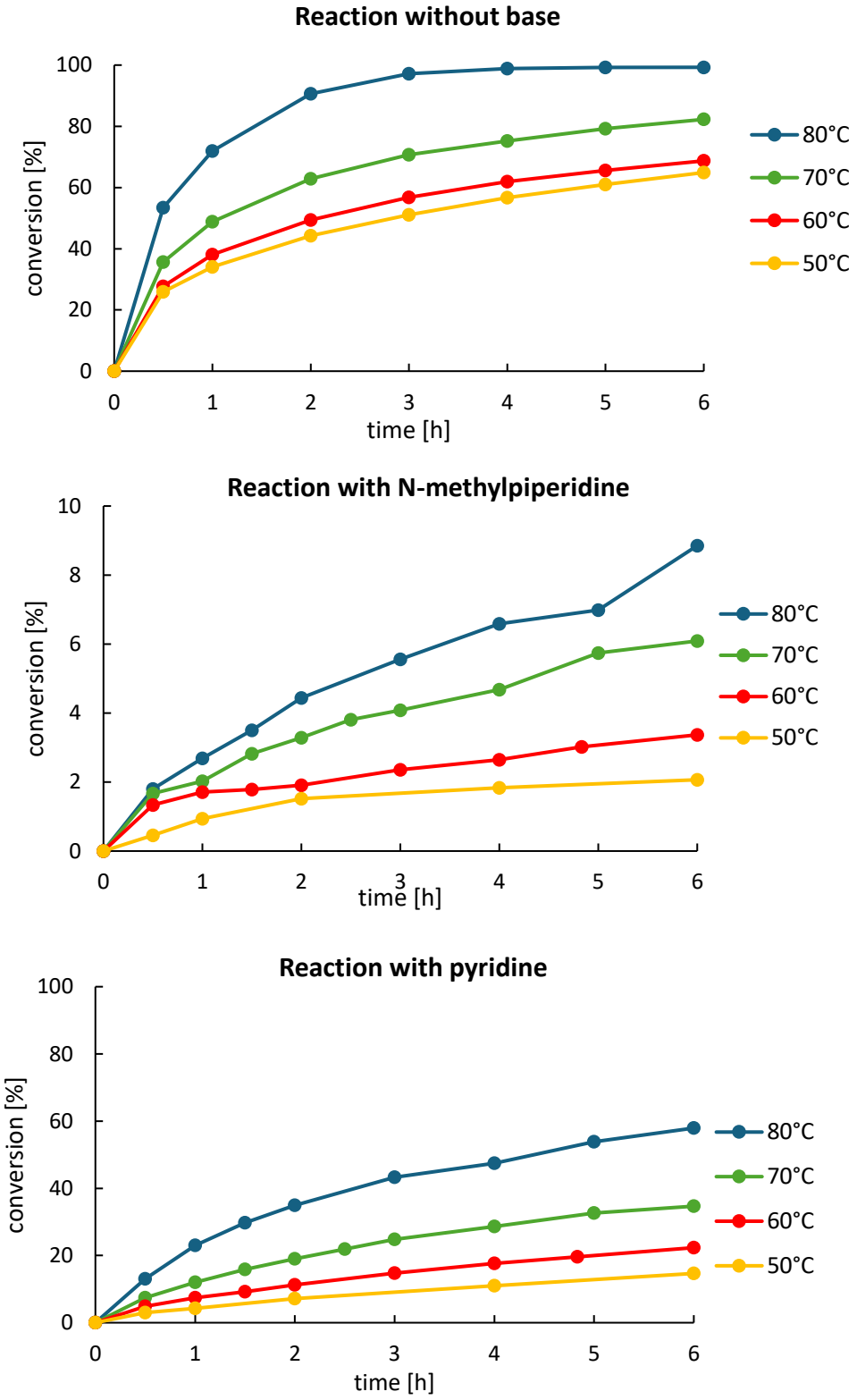

Figure 33: Conversion curves of the citronellal reaction without base over 40 mg Sn-beta, with N-methylpiperidine and pyridine over 200 mg catalyst at different temperatures (base/citronellal is 1:10)

Reaction without base

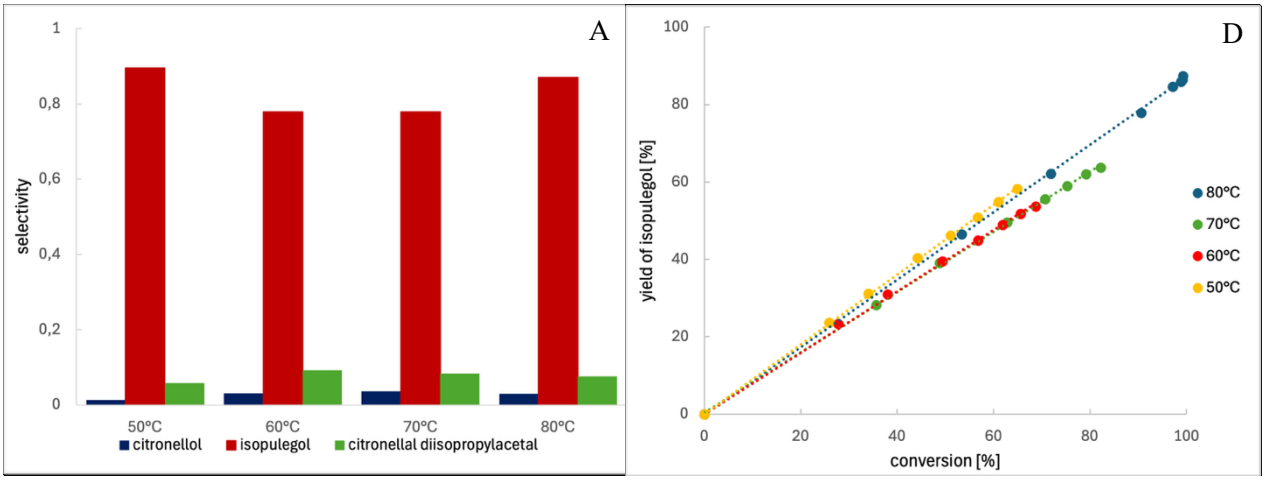

Reaction with N-methylpiperidine

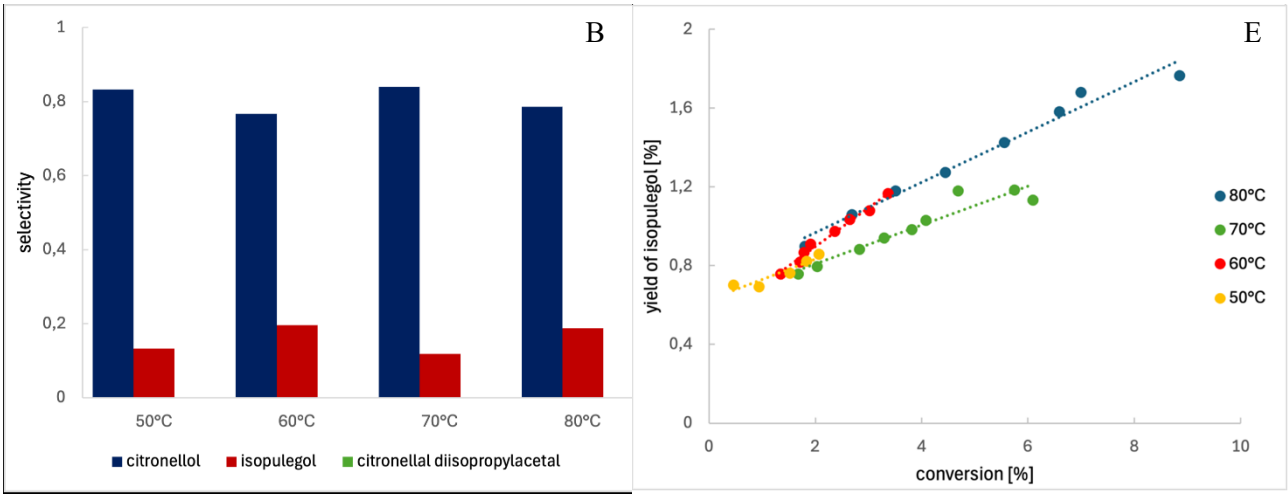

Reaction with pyridine

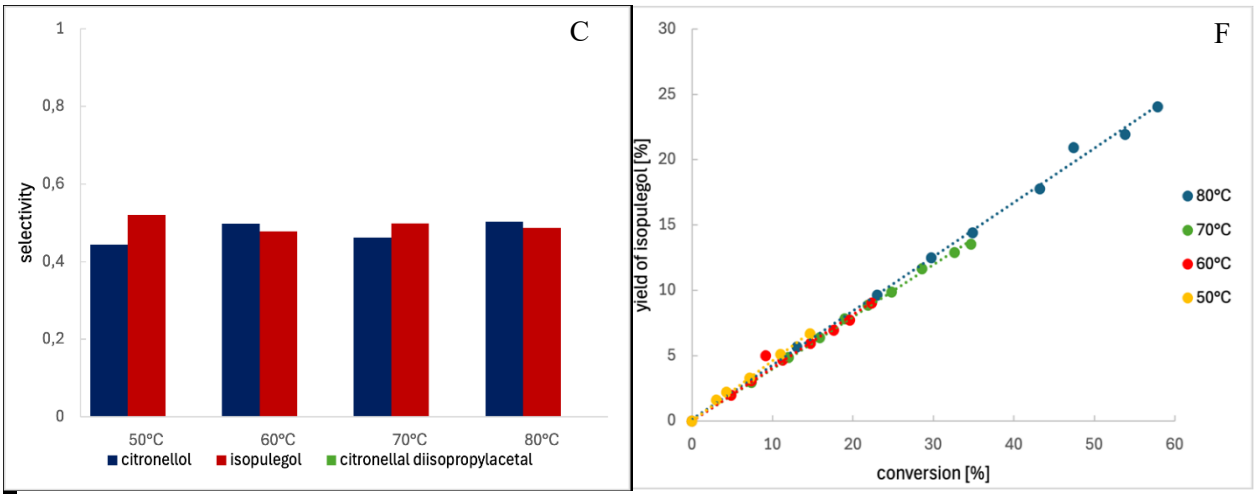

Figure 34: Distribution of the products at 20% conversion for base-free reaction and with pyridine, at 3% conversion for N-methylpiperidine (graphs A-C), isopulegol selectivity curves over conversion (graphs D-F) for base-free reaction and with bases over Sn-beta

The TOF values for the MPV reduction over Sn-beta, listed in Table 13, show an obvious general increase in activity with temperature in all systems. In the absence of the base, isopulegol formation dominates across the whole temperature range, indicating a strong preference for the cyclization pathway. This is in line with the fact that Sn Lewis acid sites are generally stronger than the Zr sites.[36] The addition of pyridine and N-methylpiperidine increases citronellol selectivity, but both bases lead to an overall decrease in TOF values compared to the base-free system, likely due to partial site blocking resulting from their strong binding of the base to the catalyst. Importantly, unlike in the Zr-beta system, no significant acceleration of citronellol formation is observed upon base addition, highlighting a different response of Sn-beta.

Table 13: TOF values of the citronellal reaction over Sn-beta without base, with pyridine and N-methylpiperidine at different temperatures

		TOF values [s^{-1}]		
		citronellal	**citronellol**	**isopulegol**
Sn-beta without base	50 °C	2.6	$1.0 \cdot 10^{-2}$	0.47
	60 °C	2.9	$8.1 \cdot 10^{-2}$	0.47
	70 °C	3.7	0.13	0.59
	80 °C	5.4	0.17	0.94
Sn-beta with N-methylpiperidine	50 °C	$2.8 \cdot 10^{-3}$	$1.2 \cdot 10^{-3}$	$1.2 \cdot 10^{-3}$
	60 °C	$1.0 \cdot 10^{-2}$	$4.7 \cdot 10^{-3}$	$4.5 \cdot 10^{-3}$
	70 °C	$1.2 \cdot 10^{-2}$	$5.9 \cdot 10^{-3}$	$4.5 \cdot 10^{-3}$
	80 °C	$1.6 \cdot 10^{-2}$	$1.2 \cdot 10^{-2}$	$6.3 \cdot 10^{-3}$
Sn-beta with pyridine	50 °C	$2.6 \cdot 10^{-2}$	$9.1 \cdot 10^{-3}$	$1.3 \cdot 10^{-2}$
	60 °C	$5.6 \cdot 10^{-2}$	$1.7 \cdot 10^{-2}$	$1.8 \cdot 10^{-2}$
	70 °C	$7.2 \cdot 10^{-2}$	$2.5 \cdot 10^{-2}$	$2.9 \cdot 10^{-2}$
	80 °C	1.4	$6.1 \cdot 10^{-2}$	$5.7 \cdot 10^{-2}$

Like in the case of Zr-beta-A, the experimental data from the Sn-beta catalysed reactions were processed using ERA software. Rate constants were determined by fitting the concentrations to the same kinetic model equations for citronellol and isopulegol formation. The results, including confidence intervals, are summarized in Table 14. Figure 35 illustrates the model fits for the base-free reaction and those with added bases at 60 °C.

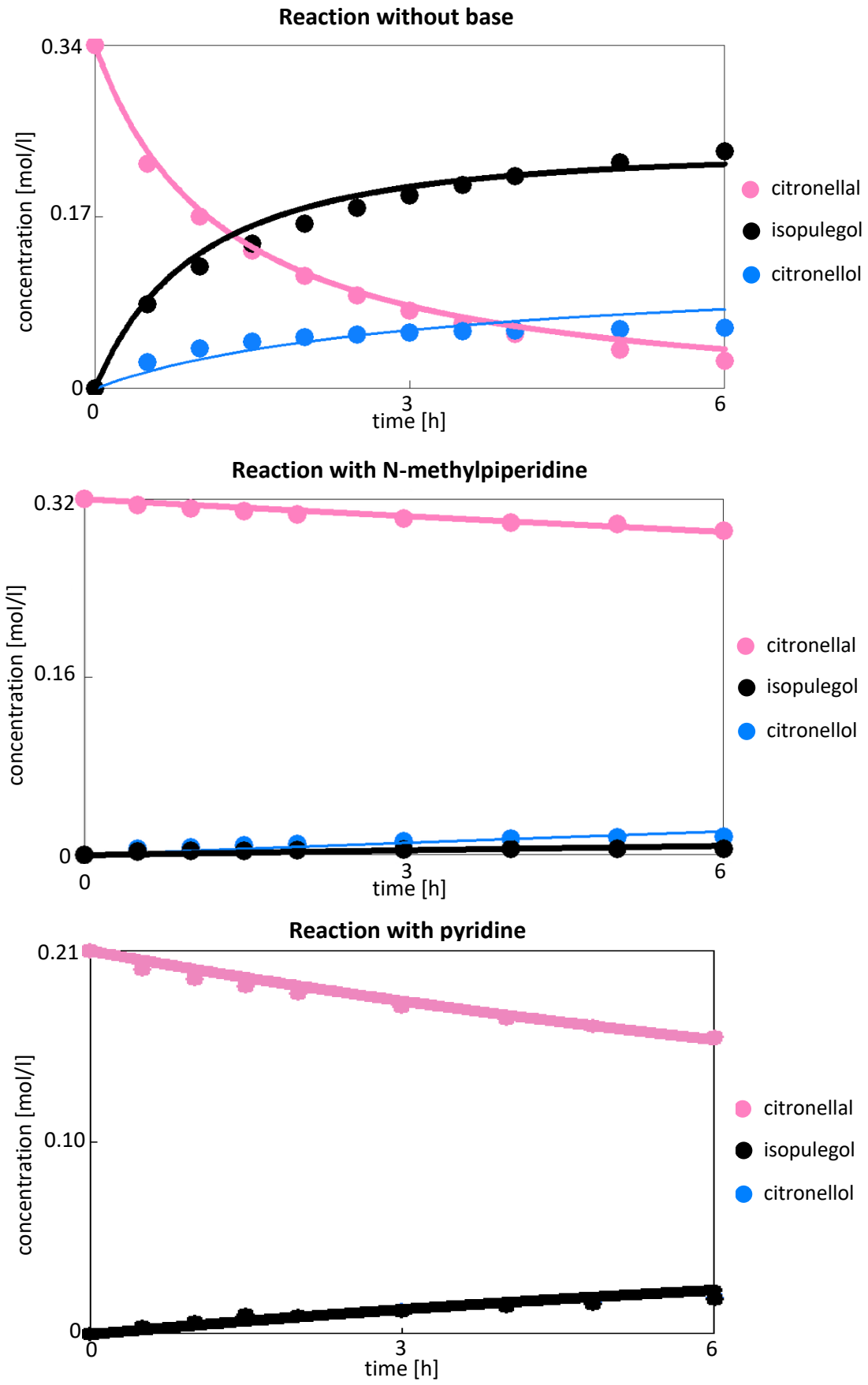

Figure 35: Concentration of reaction components denpendance on time for citronellal reduction at 60 °C over Sn-beta

Table 14: Calculated rate constants, low and high F-limits for kinetic study over Sn-beta

			rate constant	low F-limit	high F-limit
Sn-beta without base	50 °C	citronellol	0.645	0.00	1.62
		isopulegol	5.05	4.81	5.35
	60 °C	citronellol	1.66	0.437	2.92
		isopulegol	5.25	4.83	5.65
	70 °C	citronellol	2.62	1.31	4.27
		isopulegol	6.35	5.90	6.85
	80 °C	citronellol	3.60	1.76	5.65
		isopulegol	13.9	12.8	14.7
Sn-beta with N-methylpiperidine	50 °C	citronellol	$7.34 \cdot 10^{-2}$	$5.19 \cdot 10^{-2}$	$8.99 \cdot 10^{-2}$
		isopulegol	$8.25 \cdot 10^{-2}$	$6.41 \cdot 10^{-2}$	$9.75 \cdot 10^{-2}$
	60 °C	citronellol	0.114	0.101	0.125
		isopulegol	$9.01 \cdot 10^{-2}$	$7.39 \cdot 10^{-2}$	0.104
	70 °C	citronellol	0.144	0.128	0.159
		isopulegol	0.121	0.101	0.140
	80 °C	citronellol	0.192	0.187	0.204
		isopulegol	0.122	0.101	0.139
Sn-beta with pyridine	50 °C	citronellol	0.159	0.128	0.192
		isopulegol	0.222	0.203	0.242
	60 °C	citronellol	0.294	0.250	0.335
		isopulegol	0.283	-0.277	0.303
	70 °C	citronellol	0.447	0.400	0.556
		isopulegol	0.388	0.358	0.416
	80 °C	citronellol	1.08	0.944	1.22
		isopulegol	0.584	0.544	0.625

To determine the apparent activation energies for each reaction pathway over Sn-beta, Arrhenius plots (Figure 36) were constructed following the same procedure as for Zr-beta-A. The slopes of the resulting linear fits were used to calculate the activation energies, and the final values are summarized in Table 15.

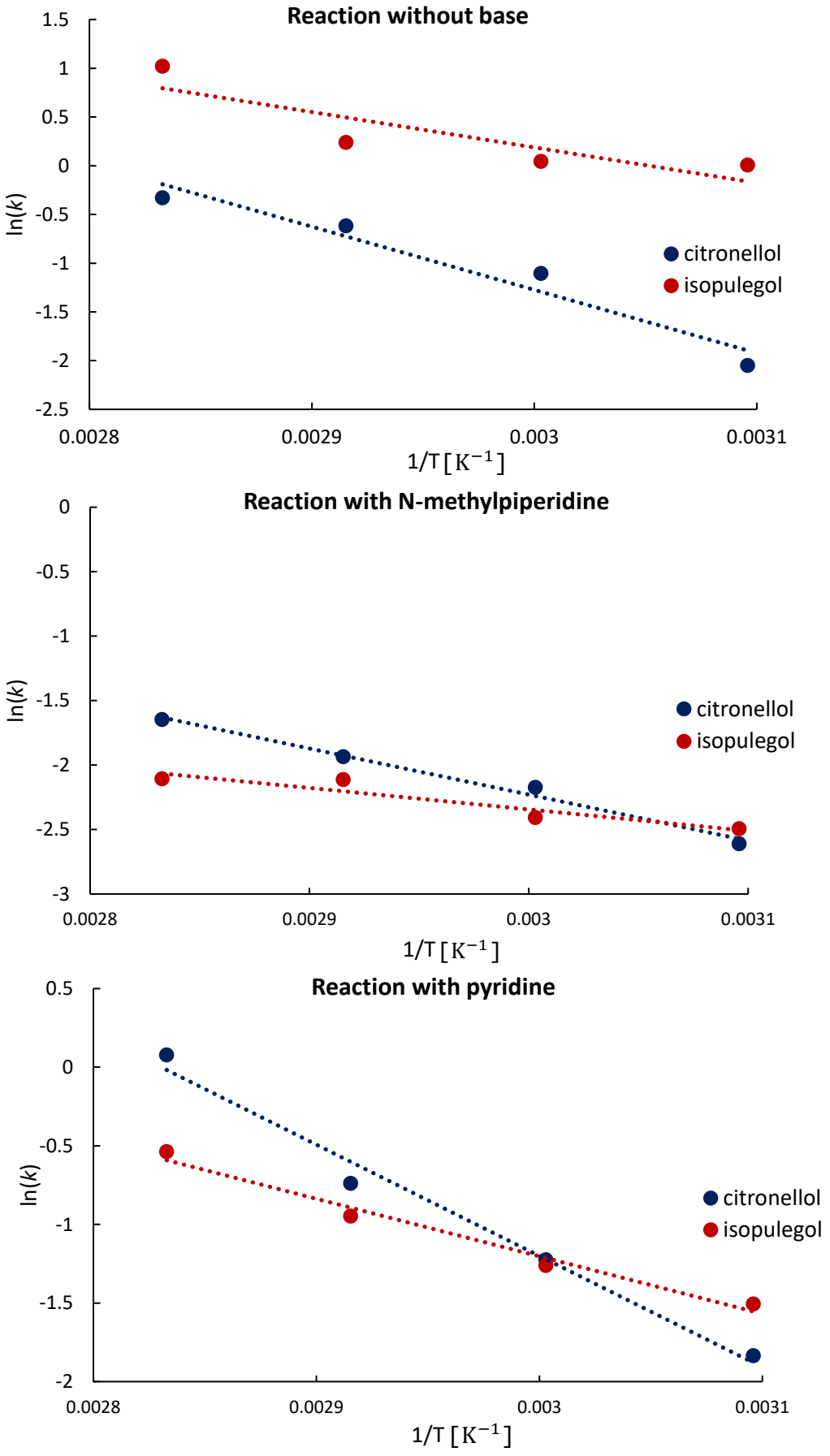

Figure 36: Arrhenius plots for base-free reaction and with adition of bases over Sn-beta

Table 15: Comparison of apparent activation energies for citronellal reaction over Sn-beta

	apparent activation energy [kJ · mol^{-1}]	
	citronellol	**isopulegol**
no base	54	30
with N-methylpiperidine	30	14
with pyridine	59	31

Similar to the reaction over Zr-beta-A, the activation energies for both citronellol and isopulegol formation over Sn-beta in the presence of N-methylpiperidine were below 30 kJ · mol^{-1}, indicating that the reaction is likely diffusion-controlled under these conditions. However, unlike the Zr system, the addition of pyridine did not lead to a decrease in activation energy for citronellol formation. Instead, it slightly increased to 59 kJ · mol^{-1}, while the value for isopulegol remained nearly unchanged compared to the base-free system. However, this small difference of 5 kJ · mol^{-1}falls within the estimated experimental uncertainty, especially considering the relatively broad confidence intervals and the lower quality of the Arrhenius plots obtained for the base-free reaction. Therefore, only qualitative conclusions can be drawn in this case. These observations suggest that the promoting effect of pyridine on citronellol formation observed with Zr-beta does not occur to the same extent with Sn-beta.

5.3 Influence of chiral base on the MPV reduction of prochiral ketones

In this part, an attempt was made to induce chiral selectivity in the MPV reduction of prochiral ketones, specifically with 3-methylcyclohexanone (scheme of the reaction in Figure 37), by using chiral amines ((R)-1-methyl-2-pyrrolidinemethanol or (S)-(-)-1-methyl-2-pyrrolidinemethanol) to modify the Zr active sites.

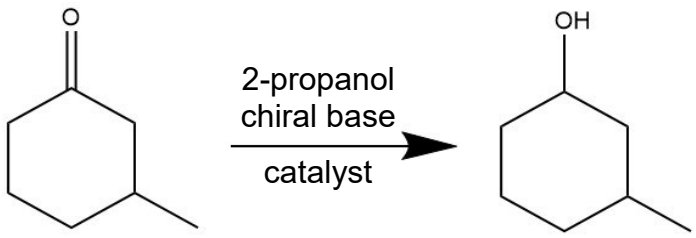

Figure 37: Scheme of the MPV reduction of 3-methylcyclohexanone with 2-propanol, chiral base (in reaction with the addition of base) over Zr-beta-B at 82 °C

The reactions were carried out without base, as well as with the addition of individual enantiomers and with a racemic mixture. From the conversion curves (Figure 38), it can be

seen that the base-free reaction proceeded significantly faster, reaching 100% conversion within 24 hours. In contrast, the reactions with bases showed much lower conversion rates, with 27% conversions after one day. Despite the significant influence of the bases on the reaction rate, analysis of the product distribution (Figure 39) revealed that the addition of chiral amines did not induce stereoselectivity. The analysis of the two product diastereoisomers of 3-methylcyclohexanol consistently showed a ratio of 3.87, corresponding to the ratio of selectivity of one enantiomer over the second, across all tested systems. Thus, we conclude that, stereoselectivity of the MPV reduction was not influenced by using the chiral amine in this case. Although chiral induction under these conditions was not successful, these results do not rule out the possibility of achieving stereoselective MPV reductions with the use of different reaction parameters.

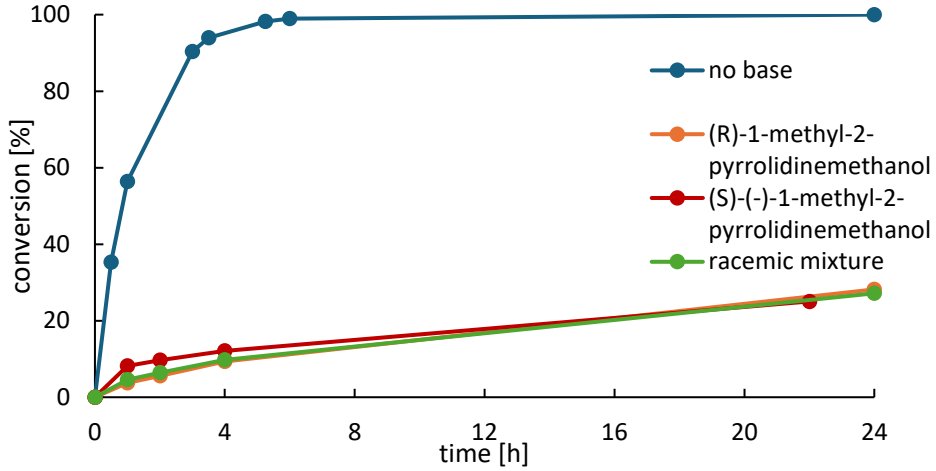

Figure 38: Conversion curves of the 3-methylcyclohexanone reaction without base and with the addition od chiral bases over Zr-beta-B

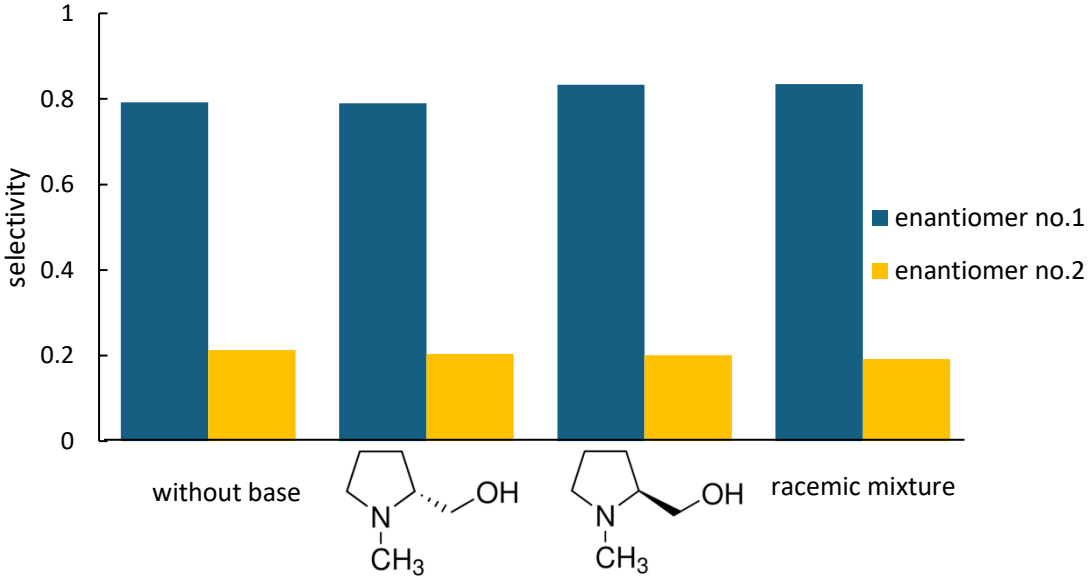

Figure 39: Distribution of the products in the 3-methylcyclohexanone reaction at 25% conversion over Zr-beta-B

6 Conclusions

This thesis explored the MPV reduction of citronellal using Zr Lewis acidic zeolites, with a focus on how nitrogen-containing organic bases influence the reaction kinetics in a system of competing reactions. Special attention was given to the contrasting behaviour of Zr-beta and Sn-beta catalysts and the mechanistic changes introduced by the addition of the bases.

The catalysts used in this study (Zr-beta-A, B, C and Sn-beta) were successfully synthesised. PXRD confirmed the formation of the desired zeolite structures with no evidence of unwanted crystalline phases. SEM imaging and UV-Vis spectroscopy revealed the presence of both framework and extra-framework (SnO_2) Sn species in the Sn-beta sample, whereas no such oxidic species were observed for the Zr-based materials. Due to sample luminescence, the UV-Vis spectra for Zr catalysts could not be reliably interpreted. However, SEM results supported their structural purity. FTIR spectroscopy using acetone as probe molecules confirmed that the materials possessed the Zr Lewis acid sites thus evidencing the Zr incorporation.

Initial experiments demonstrated reproducibility in the MPV reduction of citronellal over Zr-beta-B, with product distributions varying by no more than 1 % point across three independent runs. Subsequent studies focused on the effect of pyridine-derived bases on catalytic performance. It was confirmed that the presence of a base shifts the product selectivity in favour of citronellol formation. However, this effect strongly depends on the steric accessibility of the nitrogen atom and the overall molecular size of the base, which governs its ability to diffuse through the zeolite channels and coordinate with Lewis acid sites. Particularly, the nitrogen atom must be able to coordinate to the Lewis site.

Reactions with pyridine and 2,5-lutidine demonstrated that the base enhances citronellol formation by accelerating the MPV pathway. This ruled out a selective poisoning mechanism and instead suggested a form of modification or activation of the catalytic centres, possibly involving the formation of a zeolite–amine complex, which alters the reaction pathway in favour of the desired product.

To better understand the reaction mechanism, kinetic studies were performed over a temperature range of 40–80 °C for Zr-beta-A and 50–80 °C for Sn-beta. The reaction

proceeded via two parallel pathways: the MPV reduction to citronellol and the carbonyl-ene cyclization to isopulegol. A key parameter determined in this study was the apparent activation energy for each reaction pathway. Rate constants and activation energies were obtained by fitting experimental data using the ERA software. For both catalysts, reactions carried out in the presence of N-methylpiperidine showed apparent activation energies below 30 $\mathrm{kJ \cdot mol^{-1}}$, indicating a diffusion-controlled regime. Over Zr-beta-A, the addition of pyridine reduced the activation energy for citronellol formation from 52 to 44 $\mathrm{kJ \cdot mol^{-1}}$ while the value for isopulegol formation remained unchanged. In contrast, pyridine had a different effect over Sn-beta. It did not enhance citronellol formation and instead increased the activation energy from 54 $\mathrm{kJ \cdot mol^{-1}}$ (without base) to 59 $\mathrm{kJ \cdot mol^{-1}}$. However, this difference of 5 $\mathrm{kJ \cdot mol^{-1}}$ falls within the possible error range of the method.

An additional part of this study aimed to explore the possibility of inducing stereoselectivity in the MPV reduction of prochiral ketones by modifying Zr-beta-B with chiral amines. Although the introduction of (R)- and (S)-1-methyl-2-pyrrolidinemethanol significantly slowed down the reaction rate, no diastereoselectivity was observed. The ratio of the resulting 3-methylcyclohexanol diastereoisomers remained constant at 3.8 across all tested systems, regardless of whether a single enantiomer or racemic mixture was used.

In conclusion, this study clearly shows that both the type of metal in the zeolite framework and the structure of added organic bases play a key role in controlling the outcome of the MPV reduction of citronellal. Even slight differences in the structure or properties of the base can significantly influence product selectivity and reaction rates. Rather than simply suppressing side reactions, selected bases, especially pyridine, can actively promote the formation of the citronellol by modifying the active sites.

7 Reference

1. Chizallet, C., Bouchy, C., Larmier, K. & Pirngruber, G. Molecular Views on Mechanisms of Brønsted Acid-Catalyzed Reactions in Zeolites. *Chem Rev* **123**, 6107–6196 (2023).
2. Thomas, J. M. Uniform Heterogeneous Catalysts: The Role of Solid-State Chemistry in their Development and Design. *Angew Chem Int Ed* **27**, 1673–1691 (1988).
3. Veselá, K. Influence of bases on heterogeneous Lewis acid catalyzed hydrogen transfer reactions. (2023).
4. Fechete, I., Wang, Y. & Védrine, J. C. The past, present and future of heterogeneous catalysis. *Catal Today* **189**, 2–27 (2012).
5. Toulhoat, H. Heterogeneous Catalysis: Use of Density Functional Theory. *Encyclopedia of Materials: Science and Technology* 1–7 (2010).
6. Nakao, R. *et al.* Performance and characterization of BEA catalysts for catalytic cracking. *Appl Catal A Gen* **273**, 63–73 (2004).
7. Li, Y. & Yu, J. Emerging applications of zeolites in catalysis, separation and host–guest assembly. *Nat Rev Mater* **6**, 1156–1174 (2021).
8. Van Leeuwen, P. W. N. M. Homogeneous Catalysis Understanding the Art. in 6–7 (2004).
9. Robinson, P. K. Enzymes: principles and biotechnological applications. *Essays Biochem* **59**, 1 (2015).
10. Feliczak-Guzik, A. Hierarchical zeolites: Synthesis and catalytic properties. *Microporous and Mesoporous Materials* **259**, 33–45 (2018).
11. Pérez-Botella, E., Valencia, S. & Rey, F. Zeolites in Adsorption Processes: State of the Art and Future Prospects. *Chem Rev* **122**, 17647–17695 (2022).
12. Król, M. Natural vs. Synthetic Zeolites. *Crystals (Basel)* **10**, 622 (2020).
13. Corma, A. From microporous to mesoporous molecular sieve materials and their use in catalysis. *Chem Rev* **97**, 2373–2419 (1997).
14. Wang, S. & Peng, Y. Natural zeolites as effective adsorbents in water and wastewater treatment. *Chemical Engineering Journal* **156**, 11–24 (2010).
15. Zhang, H., Wang, B. & Yan, W. The structure-directing role of heterologous seeds in the synthesis of zeolite. *Green Energy & Environment* 1–3 (2023).

16. Ackley, M. W., Rege, S. U. & Himanshu, S. Application of natural zeolites in the purification and separation of gases. *Microporous and Mesoporous Materials* 26–40 (2003).
17. Database of Zeolite Structures. https://www.iza-structure.org/databases/. [10.12.2024]
18. Čejka, J., Morris, R. E. & Nachtigall, P. Zeolites in Catalysis: Properties and Applications. *The Royal Society of Chemistry* 37–71 (2017).
19. Suib, S. L., Přech, J., Szaniawska, E. & Čejka, J. Recent Advances in Tetra- (Ti, Sn, Zr, Hf) and Pentavalent (Nb, V, Ta) Metal-Substituted Molecular Sieve Catalysis. *Chem Rev* **123**, 877–917 (2023).
20. Raman, G. Identifying extra-large pore structures in zeolites with a machine learning approach and its deployment into production. *Microporous and Mesoporous Materials* **348**, 1 (2023).
21. Smith, J. V. Topochemistry of Zeolites and Related Materials. 1. Topology and Geometry. *Chem. Rev* **88**, 149–182 (1988).
22. Veselý, O., Morris, R. E. & Čejka, J. Beyond traditional synthesis of zeolites: The impact of germanosilicate chemistry in the search for new materials. *Microporous and Mesoporous Materials* **358**, 1–5 (2023).
23. Paillaud, J.-L. & Patarin, J. Synthesis Commission of the International Zeolite Association. *Verified syntheses of zeolitic materials 3 ed.* 24–28 (2016).
24. Lang, Q., Lu, P., Yang, X. & Valtchev, V. Zeolites for the environment. *Green Carbon* **2**, 12–14 (2024).
25. Román-Leshkov, Y., Moliner, M., Labinger, J. A. & Davis, M. E. Mechanism of glucose isomerization using a solid Lewis acid catalyst in water. *Angew Chem Int Ed Engl* **49**, 8954–8957 (2010).
26. Corma, A., Nemeth, L. T., Renz, M. & Valencia, S. Sn-zeolite beta as a heterogeneous chemoselective catalyst for Baeyer-Villiger oxidations. *Nature* **412**, 423–425 (2001).
27. Přech, J. Catalytic performance of advanced titanosilicate selective oxidation catalysts – a review. *Catalysis Reviews* **60**, 71–131 (2018).
28. Corma, A. & Renz, M. A General Method for the Preparation of Ethers Using Water-Resistant Solid Lewis Acids. *Angewandte Chemie International Edition* **46**, 298–300 (2007).
29. Bellussi, G., Millini, R., Pollesel, P. & Perego, C. Zeolite science and technology at Eni. *New Journal of Chemistry* **40**, 4061–4077 (2016).

30. Camblor, M. A., Corma, A. & Valencia, S. Spontaneous nucleation and growth of pure silica zeolite-β free of connectivity defects. *Chemical Communications* 2365–2366 (1996).
31. Dapsens, P. Y. ;, Mondelli, C. ;, Pérez-Ramírez, J., Dapsens, P. Y. & Mondelli, C. Design of Lewis-acid centres in zeolitic matrices for the conversion of renewables. *Chem Soc Rev* **44**, 7025–7043 (2015).
32. Beta: DO Family. https://europe.iza-structure.org/IZA-SC/DO_structures/DO_family.php?ID=1. [25.2.2025]
33. Newsam, J. M., Treacy, M. M. J., Koetsier, W. T. & De Gruyter, C. B. Structural characterization of zeolite beta. *Proc R Soc Lond A Math Phys Sci* **420**, 375–405 (1988).
34. Higgins, J. B. *et al.* The framework topology of zeolite beta. *Zeolites* **8**, 446–452 (1988).
35. Boronat, M., Concepción, P., Corma, A., Renz, M. & Valencia, S. Determination of the catalytically active oxidation Lewis acid sites in Sn-beta zeolites, and their optimisation by the combination of theoretical and experimental studies. *J Catal* **234**, 111–118 (2005).
36. Přech Jan *et al.* unpublished results. Preprint at (2023).
37. Bates, J. S., Bukowski, B. C., Harris, J. W., Greeley, J. & Gounder, R. Distinct Catalytic Reactivity of Sn Substituted in Framework Locations and at Defect Grain Boundaries in Sn-Zeolites. *ACS Catal* **9**, 6146–6168 (2019).
38. Bermejo-Deval, R., Orazov, M., Gounder, R., Hwang, S. J. & Davis, M. E. Active sites in Sn-beta for glucose isomerization to fructose and epimerization to mannose. *ACS Catal* **4**, 2288–2297 (2014).
39. Boronat, M. & Corma, A. What Is Measured When Measuring Acidity in Zeolites with Probe Molecules? *ACS Catal* **9**, 1539–1548 (2019).
40. Bordiga, S., Lamberti, C., Bonino, F., Travert, A. & Thibault-Starzyk, F. Probing zeolites by vibrational spectroscopies. *Chem Soc Rev* **44**, 7262–7341 (2015).
41. Sushkevich, V. L., Vimont, A., Travert, A. & Ivanova, I. I. Spectroscopic Evidence for Open and Closed Lewis Acid Sites in ZrBEA Zeolites. *Journal of Physical Chemistry C* **119**, 17633–17639 (2015).
42. McMurry, J. *Organická Chemie*. 47-50 (2023).
43. Shamzhy, M. *et al.* Quantification of Lewis acid sites in 3D and 2D TS-1 zeolites: FTIR spectroscopic study. *Catal Today* **345**, 80–87 (2020).

44. Gil, B. Acidity of zeolites, In: J.Čejka, J.Peréz-Pariente, W.J. Roth (Eds.), Zeolites: From Model Materials to Industrial Cataylsts Transworld Research Network. in *Zeolites* 173–207 (2008).
45. Van Der Waal, J. C., Creyghton, E. J., Kunkeler, P. J., Tan, K. & Van Bekkum, H. Beta-type zeolites as selective and regenerable catalysts in the Meerwein-Ponndorf-Verley reduction of carbonyl compounds. *Top Catal* **4**, 261–268 (1997).
46. Choudhary, V. R. Titration of active acid sites on zeolites by selective poisoning of stronger acid sites. *Zeolites* **7**, 272–276 (1987).
47. Miñambres, J. F. & Čejka, J. Meerwein-Ponndorf-Verley reduction in current heterogeneous catalysis research: a review. *Catal Rev Sci Eng* (2023).
48. Meerwein, H. & Schmidt, R. Ein neues Verfahren zur Reduktion von Aldehyden und Ketonen. *Justus Liebigs Ann Chem* **444**, 221–238 (1925).
49. Ponndorf, W. Der reversible Austausch der Oxydationsstufen zwischen Aldehyden oder Ketonen einerseits und primären oder sekundären Alkoholen anderseits. *Angewandte Chemie* **39**, 138–143 (1926).
50. Chuah, G. K., Jaenicke, S., Zhu, Y. Z. & Liu, S. H. Meerwein-Ponndorf-Verley Reduction over Heterogeneous Catalysts. *Curr Org Chem* **10**, 1639–1654 (2006).
51. Luo, H. Y., Consoli, D. F., Gunther, W. R. & Román-Leshkov, Y. Investigation of the reaction kinetics of isolated Lewis acid sites in Beta zeolites for the Meerwein–Ponndorf–Verley reduction of methyl levulinate to γ-valerolactone. *J Catal* **320**, 198–207 (2014).
52. Creyghton, E. J., Huskens, J., Van Der Waal, J. C. & Van Bekkum, H. Meerwein-Ponndorf-Verley and Oppenauer reactions catalysed by heterogeneous catalysts. *Stud Surf Sci Catal* **108**, 531–537 (1997).
53. Connolly, J. R. Introduction to X-ray Powder Diffraction. *EPS400-002* 1–9 (2005).
54. X-ray Powder Diffraction (XRD). https://serc.carleton.edu/research_education/geochemsheets/techniques/XRD.html. [3.1.2025]
55. Suslick, K. S. & Neimark, A. V. HANDBOOK OF HETEROGENEOUS CATALYSIS: Characterisation of Solid Catalysts. 721–1258 (2008).
56. Čejka, J., Morris, R. E. & Serrano, D. P. Catalysis on Zeolites – Catalysis Science & Technology. *Catal Sci Technol* **6**, 2465–2466 (2016).

57. Malyshev, M. E., Paukshtis, E. A., Malysheva, L. V., Toktarev, A. V. & Vostrikova, L. A. N2 and CO as probe molecules for determining the properties of acid sites on the surface of zeolites. *Kinetics and Catalysis* **46**, 100–106 (2005).
58. Sing, K. S. W. *et al.* Reporting Physisorption Data for Gas/Solid Systems with Special Reference to the Determination of Surface Area and Porosity. *Pure and Applied Chemistry* **57**, 603–619 (1985).
59. Naderi, M. Surface Area: Brunauer–Emmett–Teller (BET). *Progress in Filtration and Separation* 585–608 (2015).
60. Galarneau, A., Villemot, F., Rodriguez, J., Fajula, F. & Coasne, B. Validity of the t-plot method to assess microporosity in hierarchical micro/mesoporous materials. *Langmuir* **30**, 13266–13274 (2014).
61. Chauhan, R., Kumar, R., Kumar, V., Sharma, K. & Sharma, V. On the discrimination of soil samples by derivative diffuse reflectance UV–vis-NIR spectroscopy and chemometric methods. *Forensic Sci Int* **319**, 1–3 (2021).
62. What is UV-Visible/UV-Vis Spectroscopy? Principles Overview | Agilent. https://www.agilent.com/en/support/molecular-spectroscopy/uv-vis-uv-vis-nir-spectroscopy/uv-vis-spectroscopy-spectrophotometer-basics. [3.1.2025]
63. Wang, X. *et al.* Characterization and catalytic properties of tin-containing mesoporous silicas prepared by different methods. *J Mol Catal A Chem* **238**, 185–191 (2005).
64. Wang, J., Okumura, K., Jaenicke, S. & Chuah, G. K. Post-synthesized zirconium-containing Beta zeolite in Meerwein–Ponndorf–Verley reduction: Pros and cons. *Appl Catal A Gen* **493**, 112–120 (2015).
65. What is ICP-MS? Principles & Technique | Agilent. https://www.agilent.com/en/product/atomic-spectroscopy/inductively-coupled-plasma-mass-spectrometry-icp-ms/what-is-icp-ms-icp-ms-faqs. [4.1.2025]
66. Koga, D., Kusumi, S., Shibata, M. & Watanabe, T. Applications of Scanning Electron Microscopy Using Secondary and Backscattered Electron Signals in Neural Structure. *Front Neuroanat* **15**, (2021).
67. Cazaux, J. From the physics of secondary electron emission to image contrasts in scanning electron microscopy. *J Electron Microsc (Tokyo)* **61**, 261–284 (2012).
68. Harris, J. W. *et al.* Titration and quantification of open and closed Lewis acid sites in Sn-Beta zeolites that catalyze glucose isomerization. *J Catal* **335**, 141–154 (2016).

69. Dereka, B., Lewis, N. H. C., Keim, J. H., Snyder, S. A. & Tokmakoff, A. Characterization of Acetonitrile Isotopologues as Vibrational Probes of Electrolytes. *Journal of Physical Chemistry B* **126**, 278–291 (2022).
70. Crocellà, V., Cerrato, G. & Morterra, C. On the adsorption/reaction of acetone on pure and sulfate-modified zirconias. *Phys Chem Chem Phys* **15**, 13461 (2013).
71. Kubelková, L., Čejka, J. & Nováková, J. Surface reactivity of ZSM-5 zeolites in interaction with ketones at ambient temperature (a FT-i.r. study). *Zeolites* **11**, 48–53 (1991).
72. Lang, S., Benz, M., Obenaus, U., Himmelmann, R. & Hunger, M. Novel Approach for the Characterization of Lewis Acidic Solid Catalysts by Solid-State NMR Spectroscopy. *ChemCatChem* **8**, 2031–2036 (2016).
73. ERA. http://old.vscht.cz/kot/era/kontakt.html. [20.11.2025]
74. Gugeler, K., Kästner, J. & Dyballa, M. Computational Approach for Determining Molecular Diameters and Access to Pores. *ACS Catal* 4798–4816 (2025).
75. Williams, R. pka Data https://organicchemistrydata.org/hansreich/resources/pka/pka_data/pka-compilation-williams.pdf. [12.4.2025]
76. Shimanouchi & Takehiko. Tables of molecular vibrational frequencies, consolidated volume i. 160 (1972).
77. Vimont, A., Thibault-Starzyk, F. & Daturi, M. Analysing and understanding the active site by IR spectroscopy. *Chem Soc Rev* **39**, 4928–4950 (2010).
78. Johnson, B. A., Di Iorio, J. R. & Román-Leshkov, Y. Identification and quantification of distinct active sites in Hf-Beta zeolites for transfer hydrogenation catalysis. *J Catal* **404**, 607–619 (2021).